

77 GHz waveguide antenna and transition for FMCW MIMO on-chip radar for autonomous driving applications

Rocío Gabriela Molina Moreno

Supervisors:

dr. Rabia Zainab Syeda

Prof.dr.ir. Martijn C. van Beurden

ir. Anton J. M. de Graauw

*A thesis submitted in fulfillment of the requirements
for the degree of Professional Doctorate in Engineering
in the*

**ELECTROMAGNETICS GROUP
DEPARTMENT OF ELECTRICAL ENGINEERING**

TEMPORARILY CONFIDENTIAL (1 June 2023)

PDEng-thesis number: 2022/034

Eindhoven, June 17th, 2022

Thesis Evaluation Committee:

Prof.dr. M.C. (Martijn) van Beurden (TU/e supervisor)
dr. R. (Rabia) Zainab Syeda (TU/e supervisor)
ir. A.J.M (Anton) de Graauw (NXP supervisor)
dr. V. (Vojkan) Vidojkovic (TU/e first independent member)
dr. B.P. (Bastiaan) de Hon (TU/e second independent member)
dr. A.J. (Aart-Jan) Hoeven (TU/e Project Based Management coach)
Prof.dr. A.B. (Bart) Smolders (TU/e chairman)

NXP Evaluation Committee:

dr. G. (Giorgio) Carluccio (NXP additional member)
dr. W.H. (Waqas) Syed (NXP additional member)

The design described in this thesis has been carried out in accordance with the TU/e Code of Scientific Conduct.

This work has been sponsored by Eindhoven Engine, Smart Mobility ENGINE EM 2018-102, project number 10027824.



This work has been facilitated by a significant financial and intellectual contribution from NXP.



Abstract

The goal of this Professional Doctorate in Engineering project is to develop a waveguide transition and an antenna array for a Frequency Modulated Continuous Wave Multiple Input Multiple Output radar transceiver. The effort is one step towards imaging radars for self-driving cars. The solution proposed must be cheap and compact, but at the same time it must achieve low losses and high isolation between antennas, especially transmitter antennas with respect to receiver antennas. The starting point for the design is an NXP Integrated Circuit radar transceiver with three transmitters and four receivers. The solution includes a launcher in package as a high-performance, low-cost transition from the integrated circuit to the waveguides that are mounted on top of the launcher. As a termination of the waveguides, an array of antennas completes the design.

First, we investigated the motivation for developing self-driving vehicles, then, a review of the existing commercial solutions of imaging radars and high performance radar transceivers was conducted. After this, the problem definition was detailed, based on the requirements of the current market of self-driving cars. With this in mind, the design, manufacture, and measurements of the launcher in package and the design of an antenna array were conducted.

As a consequence of new design rules, re-optimizations of a previously designed launcher in package were conducted. Also, a version of the launcher for higher frequencies based on the same technology was proposed. The simulation results for reflection and transmission performance of the launcher and a waveguide fan-out device are presented. The launcher and a waveguide fan-out device are fabricated and the results show that the choice of connection between the launcher and a metal surface is of high relevance for the final performance of the launcher.

The antenna array consists of seven slotted-waveguide antennas, where the slots are placed on the narrow wall of each waveguide. This solution has a longitudinal polarization and is a type of antenna that is less studied than the transversely polarized case in automotive applications. After careful design, the antenna array is shown to achieve the performance required for a module for blind-spot detection with a narrow frequency bandwidth in terms of impedance matching. Finally, the system can be integrated from the integrated circuit to the antenna array. Also, the results exhibit low losses and the device is sufficiently cheap to be mass produced.

Contents

Contents	iii
List of Figures	v
List of Tables	vii
1 Introduction	1
1.1 The promise of autonomous driving	1
1.2 Motivation	1
1.2.1 History of radars	3
1.2.2 Types of radars	3
1.3 State of the art of commercial automotive MIMO radars	8
1.3.1 Transceiver suppliers (77 GHz band)	8
1.3.2 Imaging radar solutions	9
1.4 Problem definition	10
1.4.1 Overview of the solution	11
1.5 Organization of the report	11
2 Requirements and constraints	12
2.1 Car radar requirements	12
2.2 Project general requirements	12
2.3 Proposed general solution	13
2.4 Detailed requirements of the solution: radar transceiver, launcher and antenna array	14
2.4.1 Barracuda and Dolphin chip	14
2.4.2 Launcher in package	14
2.4.3 Antenna array	15
2.5 Planning	16
3 Launcher in package	18
3.1 Launcher principle of operation	18
3.2 Launcher design specification goals	18
3.3 Launcher and waveguide fan-out design	19
3.4 Launcher and waveguide fan-out fabrication	23
3.4.1 Launcher	23
3.4.2 Waveguide fan-out	23
3.5 Measurements of launcher and waveguide fan-out	24

3.5.1	Measurement strategy	25
3.5.2	Measurement results	25
3.5.3	Analysis of results	26
3.6	Conclusions	31
4	Slotted-waveguide antenna array	32
4.1	Antenna specification goals and constraints	32
4.2	Slotted-waveguide antenna theoretical model	33
4.2.1	Longitudinally polarized slotted-waveguide antenna analytical model based on literature	34
4.3	Longitudinally polarized slotted-waveguide antenna array design	36
4.3.1	Feeding strategy	36
4.3.2	Travelling wave vs standing wave	38
4.3.3	Single-slot design	38
4.3.4	Slot-array design	38
4.3.5	Second alternative for a slot design	42
4.3.6	Impedance-matching structure	43
4.3.7	Beamforming network and integration of the design	45
4.4	Slotted-waveguide antenna fabrication	48
4.5	Slotted-waveguide antenna characterization	48
4.6	Comparison of longitudinally and transversely polarized slotted-waveguide an- tenna	48
4.7	Conclusions	49
5	Conclusions and future work	50
5.1	Conclusions	50
5.2	Future work	51
	Bibliography	53
	Appendix	58
A	State of the art of commercial automotive MIMO radars	59
A.1	Transceiver suppliers (77 GHz band)	59
A.2	Imaging radar solutions	61
B	Additional measurement results launcher in package	64
C	Additional simulation results slotted-waveguide antenna	70
C.1	Side feed design	71
C.2	Loaded waveguide	75
C.3	Central feed design	75
C.4	Model with added metal plane	78

List of Figures

1.1	Car multi-sensor scheme.	2
1.2	Radar principle of operation.	4
1.3	Overview of the proposed radar solution	11
2.1	Demonstrator functional blocks.	14
2.2	NXP TEF810X transceiver functional blocks.	15
2.3	Tx and Rx positions of the radar module.	16
3.1	Conceptual scheme of dielectric and metal layers for laminate manufacturing technology designs.	19
3.2	Back-to-back model of the 77 GHz launcher with conductive interface.	21
3.3	Final model of the launcher and waveguide to be manufactured and tested.	21
3.4	Waveguide fan-out performance.	22
3.5	Simulated performance of the 77 GHz launcher.	22
3.6	Simulated performance of the 100 GHz launcher.	23
3.7	Final model of the launcher in package.	24
3.8	Final model of the waveguide fan-out.	24
3.9	Measurement connections to characterize launcher s-parameters.	26
3.10	Waveguide fan-out performance.	27
3.11	Dielectric layer launcher performance.	29
3.12	Conductive layer launcher performance.	30
4.1	Rectangular waveguide mode TE ₁₀ with slots.	33
4.2	Longitudinally polarized slotted-waveguide design parameters.	34
4.3	Equivalent circuit for a slot array.	36
4.4	Design flow of a slotted-waveguide antenna.	37
4.5	Scheme of a longitudinally polarized slotted-waveguide antenna feed from the side and from the middle.	37
4.6	T feed wave propagation.	39
4.7	Middle feed model. 3D Ludwig 3 copolar and cross-polar component for 76.5 GHz.	40
4.8	Middle feed model. Ludwig 3 copolar and cross-polar component for 76.5 GHz.	40
4.9	Middle feed 15° model simulation results.	41
4.10	Middle feed model. Ludwig 3 copolar and cross-polar component for 76.5 GHz, second iteration.	42
4.11	Middle feed 30° model simulation results.	43
4.12	Input impedance of the shorted center-feed slotted-waveguide antenna.	44

4.13	Impedance-matching network formed by capacitive or inductive irises.	44
4.14	Middle feed 30° model, with matching structure, simulation results.	45
4.15	90° H bend reflection and transmission coefficient.	46
4.16	Beamforming network for a seven-channel slotted-waveguide antenna array. .	47
4.17	Seven-channel antenna array.	47
4.18	Single-channel antenna model to be fabricated.	48
B.1	Different launcher samples.	64
B.2	Launcher assembly in waveguide fan-out.	65
B.3	Isolation between lateral channels.	65
B.4	Isolation between diagonal channels.	66
B.5	Simulation for different material interfaces.	66
B.6	Testing set-up for pressure measurements.	67
B.7	Summary of conducted measurements.	68
B.8	Summary results of different samples.	69
C.1	Normalized conductance with respect to angle.	70
C.2	Normalized conductance with respect to width.	71
C.3	Side feed model. Ludwig 3 copolar and cross-polar component for 76.5 GHz. .	72
C.4	Side feed model. Ludwig 3 copolar (longitudinal) for different frequencies. . .	73
C.5	Side feed model. Ludwig 3 cross-polar (transverse) for different frequencies. .	74
C.6	Reflection coefficient in a loaded middle-fed slotted waveguide antenna. . . .	75
C.7	Middle feed model. Ludwig 3 copolar (longitudinal) for various frequencies. .	76
C.8	Middle feed model. Ludwig 3 cross-polar (transverse) for various frequencies. .	77
C.9	Middle feed 30° model, with matching structure and metal plane, simulation results.	78

List of Tables

1.1	Comparison of the different levels of self-driving cars.	6
1.2	Comparison of the capabilities of a camera, radar, lidar and ultrasonic sensor for autonomous cars.	7
1.3	Comparison of transceiver suppliers.	9
1.4	Comparison of imaging radar solutions.	10
2.1	Launcher in package target performance parameters.	15
2.2	Slotted waveguide antenna array target performance parameters.	16
3.1	Design inputs used for the design of the launcher: layers thicknesses and electrical properties.	20
3.2	Design rules used for the design of the launcher: minimum spacing and dimensions.	20
3.3	Launcher performance summary.	27
3.4	Properties of interfaces materials.	28

Acronyms

- ACC** Adaptive Cruise Control. 1, 8, 59
- ADAS** Advanced Driver Assistant System. 1, 8, 59
- ADC** Analog to Digital Converter. 14, 59–61
- AEB** Autonomous Emergency Braking. 1, 8, 59
- BGA** Ball Grid Array. 60, 61
- BSD** Blind Spot Detection. 1, 8, 15, 32, 38, 43, 49, 50, 59, 71
- CA** Front/Rear/Lateral Collision Avoidance. 1
- CST** CST Microwave Studio. 38, 39
- CTA** Cross Traffic Alert. 1, 8, 59
- CW** Continuous Wave. 4
- DOA** Direction of Arrival. 4
- EM** Electromagnetics. 25
- EPC** Equipment and Prototype Center. 23, 48
- FMCW** Frequency Modulated Continuous Wave. 3, 4, 8, 9, 13, 14, 59–62
- FOV** Field Of View. 9, 10, 13, 61–63
- IC** Integrated Circuit. 8, 11, 13–16, 18–20, 25, 50, 51, 61
- LCA** Lane Change Assistant. 1
- lidar** Light Detection And Ranging. 2, 3, 7, 8, 10, 60
- LiP** Launcher in Package. 15–17, 50, 51
- LNA** Low Noise Amplifier. 8, 61
- MIMO** Multiple Input Multiple Output. 5, 8–10, 13, 50, 51, 59–62

MTI Moving Target Indication. 4

NCAP New Car Assessment Programme. 2, 8, 59

PA Parking Assist. 1

PCB Printed Circuit Board. 13, 14, 18, 19, 50

PDEng Professional Doctorate in Engineering. 14, 18, 19, 32

PLL Phase Locked Loop. 14, 60, 61

PTH Plated Through Holes. 19

radar Radio Detection And Ranging. 1–5, 7–15, 18, 20, 43, 50–52, 59–62

RF Radio Frequency. 3, 4, 38

RFCMOS Radio Frequency Complementary Metal Oxide Semiconductor. 14

ROD Rear Occupant Detection. 1

Rx Receive. 9, 13, 15, 16, 20, 32, 45–48, 50, 59–62

SLL Side-Lobe Level. 13, 36, 39–43, 45, 48, 51, 71, 78

TI Texas Instruments. 8, 9, 60, 61

TRL Thru-Reflect-Line. 25

TU/e Eindhoven University of Technology. 1, 16, 23, 25, 48

Tx Transmit. 9, 13, 15, 16, 20, 32, 45–48, 50, 59–62

UMS United Monolithic Semiconductors. 8, 61

VCO Voltage Controlled Oscillator. 14

VNA Vector Network Analyzer. 17, 20, 23–26, 48

Chapter 1

Introduction

1.1 The promise of autonomous driving

Autonomous driving is currently one of the hot topics in technology development. The idea of fully autonomous or self-driving cars operating in a smart mobility network is something that many companies and developers aim for [1]. In a world with fully automated vehicles, there would be fewer accidents, less pollution, less congestion [2], and for users, it might imply more productivity and comfort, because car-users could decide to perform a parallel task while commuting instead of driving. Also, a smart network including autonomous cars would allow a more efficient route decision. At the same time, it will allow safe transportation for people who can not drive, e.g. due to a disability, being under aged or elderly, or after consumption of alcohol.

Nevertheless, there are still many open questions regarding the legislation, and the required technology is not yet mature enough to allow a fully automated vehicle network. There are many legal and moral scenarios that have not been defined and regulated and there is no consensus on what to tell the car to do in a specific situation [3]. Regarding technology: the reliability of the sensors, the interference between Radio Detection And Ranging (radar) and communication signals, the algorithms for decision-making, proper security standards to guarantee that the system will not be hacked, data management, and the cost of the devices are some of the topics that still need to be improved.

This work aims to address improvements for the technology side, specifically the hardware perspective. The goal of this project is to develop a radar integrated solution that is reliable, has low interference and is cheap, as an intermediate step towards an imaging radar, capable of 3D mapping of the surrounding of a car. This project is a collaboration between Eindhoven University of Technology (TU/e) and NXP.

1.2 Motivation

The idea of fully automated cars has been growing since 1990 [4]. Currently, several car companies have included the possibility of partially automated functionalities such as Adaptive Cruise Control (ACC), Lane Change Assistant (LCA), Cross Traffic Alert (CTA), Front/Rear/Lateral Collision Avoidance (CA), Blind Spot Detection (BSD), Parking Assist (PA), Autonomous Emergency Braking (AEB), Rear Occupant Detection (ROD), traffic sign recognition, pedestrian detection either as a Advanced Driver Assistant System (ADAS), or

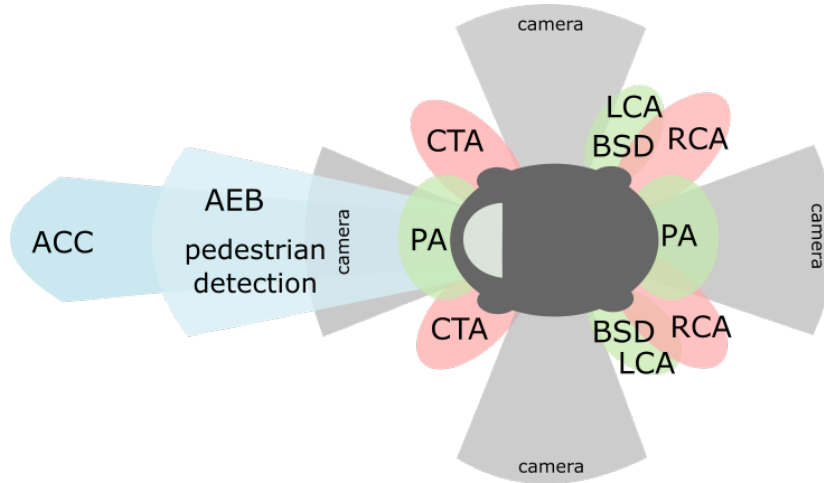


Figure 1.1: Car multi-sensor scheme: Video cameras are placed surrounding the car and different radars in short, medium and long range are used for different purposes.

to comply with regulations indicated by the New Car Assessment Programme (NCAP) [5], see Figure 1.1. Also, there have been self-driving vehicle demonstrators e.g. by Waymo (formerly Google) [6], Tesla [7], Nuro [8] and Uber [9]. Nevertheless, no vehicle with level-5 automation has been approved for the market yet. Level-5 automation stands for a vehicle that can perform all driving tasks under all conditions, without human intervention or attention required as summarized in Table 1.1 [10].

An automated vehicle without driver will need to be able to see, think, and act by itself, which requires reliable sensors, smart algorithms and fast and robust actuators. The design of such a system is challenging because the car must be able to constantly sense its environment, which is constantly changing. At the same time, it must be able to perform fast real-time decision making, by taking into account several factors such as changing weather and light conditions, fast-moving targets, stationary targets, both large and small and with different textures and colors. Most importantly, the consequences of an error can range from serious damage to private or public property to loss of lives. For that reason, the reliability of sensors and algorithms is of great importance.

A reliable multi-sensor network is therefore needed to collect as much information as possible, so that the decision-making algorithm can be properly fed. There are various types of sensors such as video cameras, Light Detection And Ranging (lidar), radar and ultrasonic sensors. In Table 1.2, a comparison of the sensors used to capture the environment is presented. Video cameras are necessary to detect color and texture and are thus required for identifying traffic signs, but they also provide images with more detail. Radar, lidar, and ultrasonic sensors are used to accurately measure the distance and the relative speed between objects. A low-cost radar is an attractive solution because they are light and weather independent and they can achieve better range and angular resolution than ultrasonic sensors. Historically, radars have been the preferred choice for measuring range outdoor. Nevertheless, one drawback, especially when compared to lidar, is that the angular resolution of a radar is not as good, which is a consequence of the wavelength at which they operate.

1.2.1 History of radars

The first radar experiments were conducted by the end of the 19th century, shortly after Heinrich Hertz detected radio waves for the first time. It was in April 1904 that Christian Hülsmeyer got a patent application for a device capable of detecting ships to avoid collisions, in spite of foggy conditions. He named his invention the Telemobiloskop [12]. It consisted of a spark-gap transmitter with dipole antennas and a parabolic antenna as a receiver system that was able to estimate the distance of the target in addition to detecting it under no-visibility conditions.

Between 1934-1939, several nations independently developed systems that, by using short pulses of radio waves, could identify the range and angular position of target aircraft and ships. In 1939, the United States Signal Corps used the name *radar* to refer to the system they worked on for the Navy [12].

The use of radar was expanded to military purposes during World War II (1939 - 1945) to identify enemies in the air, on the ground, and at sea. Since then, radars have evolved and have been used for several purposes. Nowadays, more than 80 years later, radars are used in civil applications for aircraft and ships, to avoid collisions, check on weather conditions, and to help in landing or approaching a harbor. For these purposes, radar systems need high transmit power to search for distant targets, so the radar systems are massive and expensive. By the end of the 20th century, low-power and relatively low-cost solutions in high frequency ranges have been developed for cars in driving assistance systems mentioned before.

Previously, the commercial frequency band used for car radar sensors was 21 - 26 GHz, known as the 24 GHz band, and currently it is 76 - 81 GHz, known as the 77 GHz band. The higher operating frequencies allow for better range and velocity resolution and accuracy and also allow for a more compact design of the antennas. Depending on the frequency range, 76-77 GHz or 77-81 GHz, radar sensors can be used for long range (10 - 250 m) or short (0.15 - 30 m) and medium (1 - 100 m) range applications respectively [13, 14]. Efforts are being made to push frequency range even further, to 140 GHz [15, 16]. This new frequency range will make feasible a better performance in terms of range and velocity resolution and also, the compact design will permit a larger array of antennas resulting in greater angular resolution.

1.2.2 Types of radars

A radar's principle of operation consists of transmitting a waveform that bounces back after hitting a target, so that a receiving system can detect the reflected signal. The frequency range for radar has historically been between radio-waves and microwaves (2 MHz - 100 GHz) while lidar operates in the infrared and visible range. Radars have been used to observe what the eye can not see: through fog, rain and snow, without ambient light and through non-metallic materials. Also, one can derive the range, velocity and angular position of the target by using radars [17].

Figure 1.2 shows an example of the Frequency Modulated Continuous Wave (FMCW) radar principle of operation. There is a control and digital signal processing unit that sends and receives digital signals. The frequency modulator or any Radio Frequency (RF) generator creates the analog signal to be transmitted by the antenna. The radio frequency signal reaches the target and then travels back, where the receiver antenna detects it. The received signal is mixed with the reference signal and is amplified and filtered and finally digitized.

The range of the target is determined by taking half of the time the signal takes to

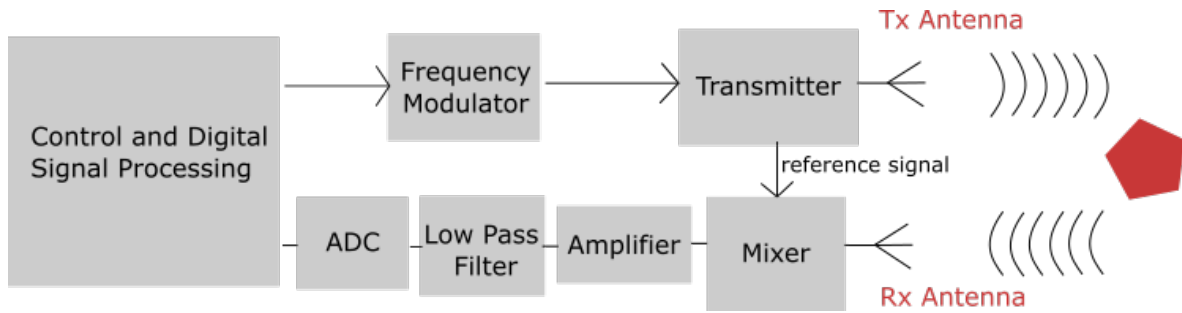


Figure 1.2: Frequency modulated radar principle of operation.

reach the receiver, times the speed of the RF signal. The relative velocity is derived by measuring a shift in the frequency of the reflected wave, which is due to the Doppler effect, and the angular position is determined by identifying the direction of arrival of the reflected wave [17]. For the latter purpose, an array of antennas can be used together with a signal processing algorithm, called a Direction of Arrival (DOA) algorithm. A matrix of data with the time and frequency shift for each receiving antenna contains all relevant information to characterize the 3D position and velocity of a target.

FMCW radars compared to other options

FMCW radars are one type among several types of radars: Continuous Wave (CW), pulse Doppler, Moving Target Indication (MTI), tracking radar, etc [17]. Below, the various types of radar and their corresponding principles are briefly discussed.

Unmodulated CW radars: the transmitter generates a continuous and unmodulated signal at a fixed frequency, usually a sinusoidal wave. In order to measure the range of the target, a time-mark must be applied to the signal. Unmodulated CW radars are used to measure the speed of the target. Some examples are: police speed monitoring, vertical-take-off rate of climb of planes controlling, docking speed of ships monitoring.

FMCW radars: the transmitter generates a frequency-modulated continuous signal. It has a larger bandwidth than the CW radar, which allows to measure range by using a timing mark. This type of radar is convenient for accurate measurement of both the range and relative speed of the target.

Pulse-Doppler radars: the transmitter generates a pulse for a certain amount of time. It is used to measure the relative velocity and range of the target. As it requires high pulse repetition rates, the speed is measured with great accuracy but it can have range ambiguities.

MTI radars: similar to Pulse-Doppler radars, the transmitter generates a pulse for a certain amount of time. It is used to measure the relative velocity and range of the target. In this case, the pulse repetition rate is low, allowing high accuracy for the measurement of the range but not for the speed of the target.

Tracking radars: their purpose is to identify a target and follow it. Various types of architectures can be used, provided that the post-processing of the data allows reliable angle tracking. Tracking radars measure range, angular position, and Doppler frequency shift to predict and follow the trajectory of a target.

From all of the above, FMCW radars are good candidates for the automotive industry as they can accurately and continuously measure range and velocity of the target.

Monostatic, bistatic and multistatic radars

Based on the architecture of the radar, it can be classified as a monostatic, bistatic, or multi-static radar. In a monostatic radar, both the transmitter and the receiver are placed at the same position. Bistatic radars, have the transmitter and receiver separated at a considerable distance, comparable to the distance of the target. Finally, multistatic radars have multiple transmitter and/or multiple receivers at different positions. Better detection capabilities, increased resolution and robustness due to redundancy are some of the advantages of this kind of radar, with the drawback that more data-processing resources are consumed [18].

Phased Array and MIMO Radars

Phased Array and Multiple Input Multiple Output (MIMO) radars are multi-static radar systems with multiple antennas and the main difference between them is that phased array radars transmit coherent signals, i.e. scaled and delayed version of a reference signal, in order to steer the beam into a desired direction. Angular resolution is related to the aperture size of the antenna array, implying a large number of antennas, which makes phased arrays expensive when high resolution is needed.

On the other hand, the antennas of MIMO radars transmit orthogonal waveforms. Each receiver then detects the signals from each transmitter after reflection from a target. This property allows them to have virtual array capabilities: the virtual array aperture is equal to the convolution of both transmit and receive apertures. For this reason, the same angular resolution can be achieved by using fewer physical antennas as compared to phased array radars [19, 20, 21]. MIMO is then better for estimation of multiple-target parameters as they could be more compact, cheaper and more versatile than a phased array.

Table 1.1: Comparison of the different levels of self-driving cars.

Property	Level 0	Level 1	Level 2	Level 3	Level 4	Level 5
Automation	Driver only *****	Assisted driving *****	Partial automation ***	Cond. automation **	High automation *	Full automation
Driver function		conditional feet off	conditional hands off	conditional eyes off	conditional mind off	full mind off
Control	human	human	human	system	system	system

Table 1.2: Comparison of the capabilities of a camera, radar, lidar and ultrasonic sensor for autonomous cars. [11]

Property	Camera	Radar	Lidar	Ultrasonic
Texture interpretation	Yes	No	No	No
Ambient light independent	No	Yes	Yes	Yes
All weather operation	No	Yes	No	Yes
Operating range	mid-far	near-far	mid-far	near
Velocity measurement	No	Yes	Yes	Yes
Angular resolution	high	medium	high	low
Cost	cheap	cheap	expensive	cheap

1.3 State of the art of commercial automotive MIMO radars

As mentioned before, the automotive industry has included radars to implement ADAS and NCAP functionalities. Companies like Bosch (Germany), Continental (Germany), Autoliv (Sweden), Hella (Germany), Denso (Japan), Delphi (UK) and Valeo (France), in partnership with semiconductor suppliers, have developed radar modules for car manufacturers. A review of the automotive vendors of these commercial solutions is given below and the characteristics of the systems are presented, with a focus on FMCW MIMO radars in the 77 GHz band. Some additional details can be found in Appendix A.1 and A.2.

1.3.1 Transceiver suppliers (77 GHz band)

There are several companies that supply semiconductor transceiver solutions. The focus of this review is on companies dedicated to the automotive industry and, in particular, on the 77 GHz car radar frequency band. A summary of the main characteristics is presented in Table 1.3 and a brief overview of the suppliers is presented below.

NXP

NXP is a Dutch-American semiconductor manufacturer. Until 2006 it was the Philips sub-division of semiconductors. In 2015, NXP acquired Freescale Semiconductors. Currently it has full solutions aimed for ACC, CTA, parking assist, AEB and BSD, including S32R26 and S32R27 microcontrollers for High-Performance radar and TEF810X Fully-Integrated 77 GHz radar Transceiver [22].

Infineon

Infineon is a German semiconductor manufacturer. Until 1999, it was a division of Siemens. In April 2020, Cypress, another semiconductor company, was acquired by Infineon [23]. Two versions of 77 GHz transceivers are under development.

Texas Instruments

Texas Instruments (TI) is an American technology company focused on semiconductors. It was founded in 1930 [24]. Currently, they have three sensors available for the 77 GHz band with (MIMO) imaging radar capabilities: AWR1642/AWR1843/AWR2243. They also provide cameras, lidar, ultrasound and sensor fusion solutions [25].

STMicroelectronics

STMicroelectronics is a French-Italian electronics and semiconductor company headquartered in Geneva, Switzerland. It was born as the fusion of SGS Microelettronica and Thomson Semiconducteurs. They have one 77 GHz STRADA770M transceiver [26].

UMS

United Monolithic Semiconductors (UMS) is a French-German company focused on RF and millimeter-wave Integrated Circuit (IC)s. They are in operation since 1996. Currently, they provide multipliers, mixers and Low Noise Amplifier (LNA)s in the range 76-77 GHz [27].

Table 1.3: Comparison of transceiver suppliers with focus on the 77 GHz frequency band. Frequency of operation, type of radar and number of Transmit (Tx) and Receive (Rx) channels are compared.

Supplier	Name	Type	Channels
NXP	TEF810X	FMCW MIMO	3Tx 4Rx
Infineon	RXS816xPL	FMCW	3Tx 4Rx
Infineon	RXS815PLA	FMCW	2Tx 4Rx
TI	AWR1642	FMCW MIMO	2Tx 4Rx
TI	AWR1843/2243	FMCW MIMO	3Tx 4Rx
STMicroelectronics	STRADA770M	FMCW MIMO	3Tx 4Rx

From all of the above, NXP, TI and STMicroelectronics have transceivers with MIMO capabilities, allowing multiple-chip connection in MIMO mode, making them feasible for imaging systems with virtual-array capabilities. NXP and TI also have application boards with wide azimuth Field Of View (FOV) and 1D scanning capability.

1.3.2 Imaging radar solutions

In the past years, a few companies have also developed full imaging radar solutions, either using proprietary transceivers or acquiring them from semiconductor suppliers. An analysis of the products that are available in the market is conducted here in order to identify potential competitors. A summary of the main characteristics is presented in Table 1.4.

Arbe Robotics

The company Arbe Robotics was founded in 2015 in Israel. Phoenix is their chipset solution with imaging capabilities [28].

Cognitive Pilot

Cognitive Pilot is a Russian company specialized in software for transport, agriculture and artificial intelligence and hardware for autonomous vehicles. Cognitive Imaging radar is their automotive radar solution [29].

Vayyar

Vayyar is an Israeli company and since 2011 they are dedicated to design low-cost imaging solutions. For the automotive industry they have one solution aimed for inside and outside the car [30].

Smartmicro

Smartmicro is a German company founded in 1997, as a spin-off from the Technical University of Braunschweig. They focus on radar design solutions for traffic, automotive, and airborne uses [31]. CATegory8 is their concept for an imaging radar solution.

Table 1.4: Comparison of imaging radar solutions for automotive purposes. Frequency of operation, number of channels, field of view, angular resolution, range limits, range resolution, speed limits and speed resolution are compared.

Supplier / device	Frequency	n° Channels	FOV / angular res.	Range / range res.	Speed / speed res.
Arbe Robotics Phoenix	unknown	24Tx 12Rx	100° Az 30° El 1° Az 2° El	300 m 7.5-60 cm	unknown 0.1 m/s
Cognitive Pilot	76 - 81 GHz	unknown	90° Az 15° El unknown	280 m 10 cm	unknown 0.03 m/s
Vayyar IMAGEVK-74	62 - 69 GHz	20Tx 20Rx	Wide 6.7°	unknown 2.14 cm	unknown unknown
Smartmicro UMRR-96 Type 153	77 - 81 GHz	unknown	130° Az 15° El 1° Az 2° El	0.15-120 m 1%	-400 - 140 km/h 0.15 m/s
Smartmicro UMRR-11 Type 132	76 - 77 GHz	unknown	100° Az 15° El 0.5° Az 0.5° El	0.5 - 175 m 1%	-400 - 200 km/h 0.1 m/s
InnoSent ISYS-5220	unknown	unknown	unknown unknown	90-350 m unknown	unknown unknown

InnoSenT

InnoSenT is a German-based company dedicated to radar technology for the automotive and other industries. It was founded in 1999 in Geldersheim [32]. They have several 3D MIMO radar solutions in the 24 GHz band.

1.4 Problem definition

The autonomous-vehicle industry has grown rapidly in the past few years. Nevertheless, commercially available vehicles that have successfully passed the safety requirements for even Level-4 automation are not yet in existence [4]. For autonomous vehicles to achieve level-5 independence, meaning being fully autonomous, some improvements need to be made. Regarding technological aspects, solutions need to be cheaper, exhibit less interference, be more reliable, specifically with respect to the proper identification of targets without false responses. The technology must guarantee the safety of the passengers and the surroundings.

Lidars are good for obtaining a 3D map of the surrounding, but they are expensive and can not operate in bad weather conditions. 2D radars do not accurately determine the height of objects, allowing possible false identifications or missing a target. 3D imaging radars can be a good alternative to lidars as long as they can achieve high angular resolution to facilitate a truthful classification of targets. That way, they can provide a 3D mapping of the surroundings, including the information of relative movement of possible targets, irrespective of weather and illumination conditions. Also, given the current technology improvements, this solution can be obtained at lower costs and reduced size.

Nevertheless, to move to imaging radars, an array of antennas with 3D capabilities is needed. The use of several antennas means that the module will use more power, will be

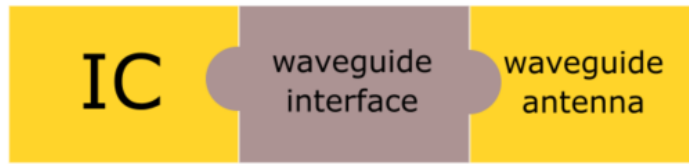


Figure 1.3: Overview of the proposed radar solution. It consists of a waveguide-like transition to connect the IC to a waveguide antenna array.

more sensitive to interference and the cost and size of the module will increase. In that sense, imaging radars will only be a feasible and attractive solution if they can be built such that they exhibit lower losses and better isolation than the current radar state of the art. Additionally, the price and volume of the radar module cannot be much higher as the current solutions.

1.4.1 Overview of the solution

The proposed solution to overcome the problem of losses and interference in between channels is to use a waveguide transition from IC to antenna and to use waveguide-like antennas instead of printed antennas.

1.5 Organization of the report

In Chapter 2 the requirements and constraints for the proposed solution are listed and explained and Chapter 3 presents the design and characterization of a transition from IC to waveguide. Chapter 4 discusses the antenna design to be mounted on top of the device. Finally, Chapter 5 contains conclusions and a discussion on future work.

Chapter 2

Requirements and constraints

2.1 Car radar requirements

Car radars need to provide a reliable picture of the environment of the car and at the same time be a profitable and commercial product. In terms of the quality of the provided information of the surrounding, a lot falls on the recognition software, but it is of great importance how much the radar can provide to it. A high angular and range resolution will allow a better instantaneous idea of the surrounding, an accurate speed measurement will allow a better prediction of future situations and a wide field of view will reduce the amount of units needed to map the 360° around the car, thus reducing costs and needed power to feed the system. However, there has to be redundancy in the sensors in case one of the modules shows a failure.

Radars are in principle a reliable solution in the sense that they can operate in most environmental situations, they do not rely on ambient light as normal cameras do, and they can still work under foggy or rainy weather conditions. Nevertheless, a radar module has to be designed in such a way to be waterproof, resistant to high speeds, shaking, and to extreme changes in temperature, to guarantee proper operation in all the particular conditions in which a car operates.

A marketable radar must ultimately be compact, to be able to locate it around the car, not disturbing other functionalities and the visual design. Additionally, it has to be competitively priced as compared with other solutions or providers.

2.2 Project general requirements

From all the car radar requirements, only a few will be considered for this project. A large focus will be on achieving a high angular and range resolution in a wide field of view. In other terms, the focus will be on improving the quality of the instant image of the surrounding. Secondly, the focus will be on providing a compact and affordable solution.

Angular resolution is a measure of how close two targets can be, in angular terms, to identify them as independent sources. The angular resolution is a function of the antenna beamwidth. When the angular resolution is small, it is approximately directly proportional to the wavelength of the signal and inversely proportional to the aperture of the sensor. In a radar module this can be achieved with higher operating frequencies as compared to the previous car radar band in 24 GHz and an array of compact antennas to increase the aperture without adding extra bulk.

Range resolution, similarly as the angular resolution, is a measure of how small the range difference between two targets can be to differentiate them as independent targets. The major factor for range resolution is the width of the transmitted radar pulse. In modulated signals, the width of the pulse is inversely proportional to the bandwidth. In the particular case of an FMCW radar module, the larger the frequency bandwidth, the higher the range resolution.

The aim is then to use a high-frequency radar module including a compact array of antennas with a large frequency bandwidth. When having an array of antennas, it is important to keep in consideration the isolation between them, to effectively differentiate targets by minimizing interference between channels. For the same purpose, to ensure a high angular resolution, the lateral or secondary beams of the antenna have to be of low power. Also, to obtain an efficient solution and to minimize the costs of operation, each of the components of the radar module has to add minimum losses, which guarantees that main part of the power is radiated, in Tx mode, or received, in Rx mode.

2.3 Proposed general solution

The proposed solution, following the general requirements previously listed, will consist in developing an integrated radar solution based on an FMCW MIMO NXP radar transceiver, as a step towards 3D imaging for future level-5 autonomous driving. A functional block diagram is shown in Figure 2.1 to facilitate understanding: the transceiver chip is located at the base of the model. On top of this IC, a launcher device is mounted to couple the power from the IC to the waveguide at the top. Finally, an array of waveguide-like antennas complete the design.

Commercially available NXP car radar transceivers cover the frequency range from 76-81 GHz, being attractive for the high frequency of operation and relatively large frequency bandwidth. The array of antennas was selected to be waveguide-like because they can, in principle, provide higher isolation between the different channels and have less losses as compared to printed antennas. The drawback is that they can be more bulky and more expensive to fabricate. The selected waveguide-like antenna has to be as compact as possible, cover the desired frequency range, have a small beamwidth and a low Side-Lobe Level (SLL). Under the same principle, a waveguide-like transition from IC to antenna was selected because of the lower losses when compared to standard Printed Circuit Board (PCB) transitions. PCB solutions are cheap and relatively easy to fabricate. The waveguide-like transition has to be designed by keeping compactness and low cost in consideration.

The general requirements of the radar module and each functional component are a trade-off in between the targeted performance, compactness and cost. The general requirements of the module are listed below:

- To cover the entire automotive frequency band: 76-81 GHz.
- To integrate an NXP IC transceiver and a waveguide-like launcher with an adequate array of waveguide-like antennas.
- To achieve a wide FOV: 100° in azimuth, 15° in elevation.
- To achieve high angular resolution: 2° by using virtual-array capabilities of MIMO.
- To cover a range between 50 cm and 250 m.

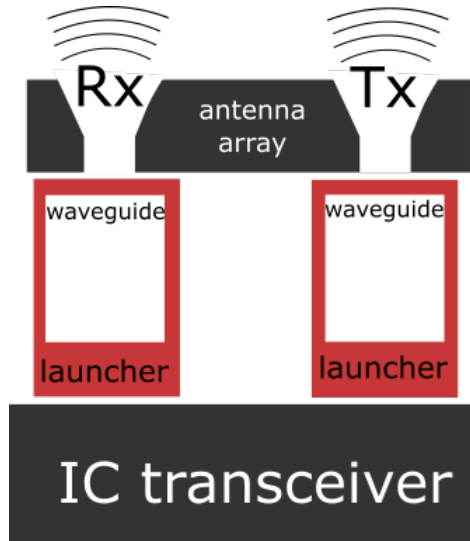


Figure 2.1: Demonstrator functional blocks.

- To achieve high isolation between channels: -30 dB.
- To achieve low transmission losses (compared to classical PCB methods).
- To have a cheap and compact demonstrator of the concept.

2.4 Detailed requirements of the solution: radar transceiver, launcher and antenna array

More in detail, the proposed solution will consist of a Barracuda IC, with an integrated launcher in package and, vertically connected on top of it, an array of seven waveguides terminated in antennas. This proposal aims to comply with all the requirements previously listed.

2.4.1 Barracuda and Dolphin chip

The NXP Barracuda radar transceiver is the starting point for this design. It is an updated version of the Dolphin chip [33], which is currently commercially available. Barracuda has all the properties of Dolphin plus enhanced cascaded connection capabilities. The NXP IC TEF810X, commonly known as the *Dolphin* chip, is a Radio Frequency Complementary Metal Oxide Semiconductor (RFCMOS) FMCW automotive radar transceiver with 3 transmitter and 4 receiver channels. It covers the range 76 – 81 GHz, allowing short, medium and long-range applications. It is a fully integrated solution including chirp generator, Analog to Digital Converter (ADC), Voltage Controlled Oscillator (VCO), Phase Locked Loop (PLL), phase control, and cascade connection for multiple chips, as illustrated in Figure 2.2 [33].

2.4.2 Launcher in package

The concept and an initial design of a launcher in package was developed under the Professional Doctorate in Engineering (PDEng) project of Valeria Tapia [34]. Due to an update

TEF810X BLOCK DIAGRAM

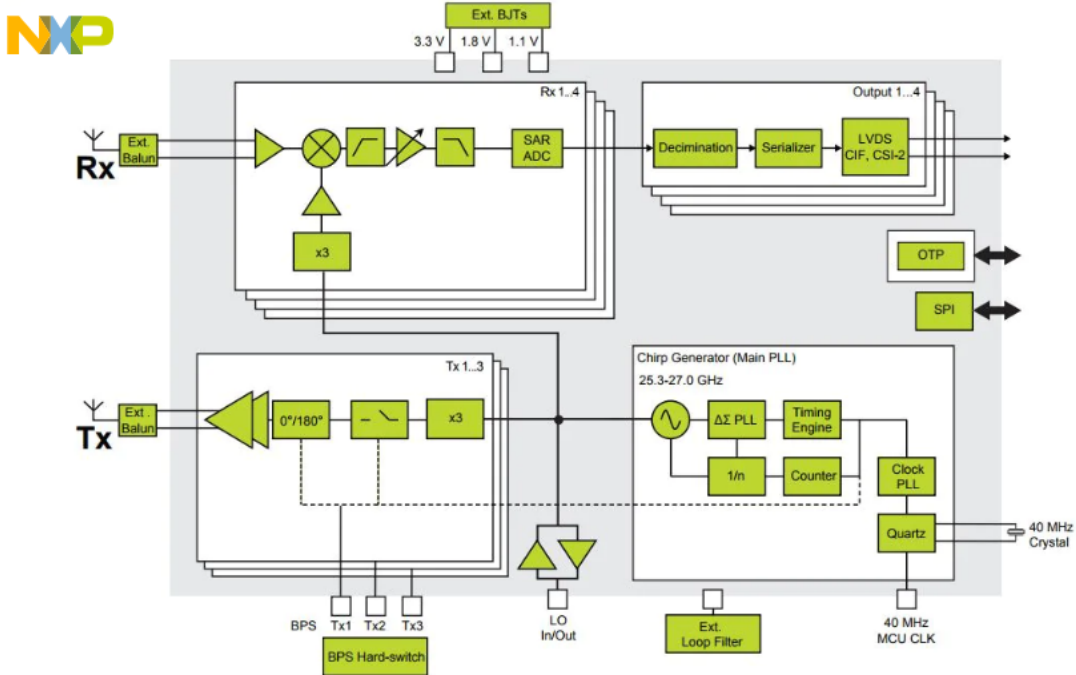


Figure 2.2: NXP TEF810X transceiver functional blocks [33].

Table 2.1: Launcher in package target performance parameters.

Parameter	Target
Frequency range	76-81 GHz
Reflection coefficient	< -15 dB
Transmission coefficient	> -2 dB
Isolation level	< -30 dB

of the design rules of the package, the design of the launcher had to be updated as well. The Launcher in Package (LiP) consists of a stack of dielectric and metal layers that create a transition from the pads of the IC to a waveguide cavity. The choice of dielectric material and some of the minimal dimensions and spacing between traces are fixed. Because it is sensitive information, the specific design rules will not be shared, but they were a strong requirement for the design of the LiP. As this part of the project was taken over from a previous design, many design choices were already made. Nevertheless, a list of performance goals is listed in Table 2.1.

2.4.3 Antenna array

It was decided to opt for a BSD radar module as a use case. The radar module for BSD consists of a single chip with three Tx and four Rx channels, located in positions defined by the NXP software team, based on their recognition software. The positions of the Tx and Rx channels are illustrated in Figure 2.3. Also, the recognition software requires a specific

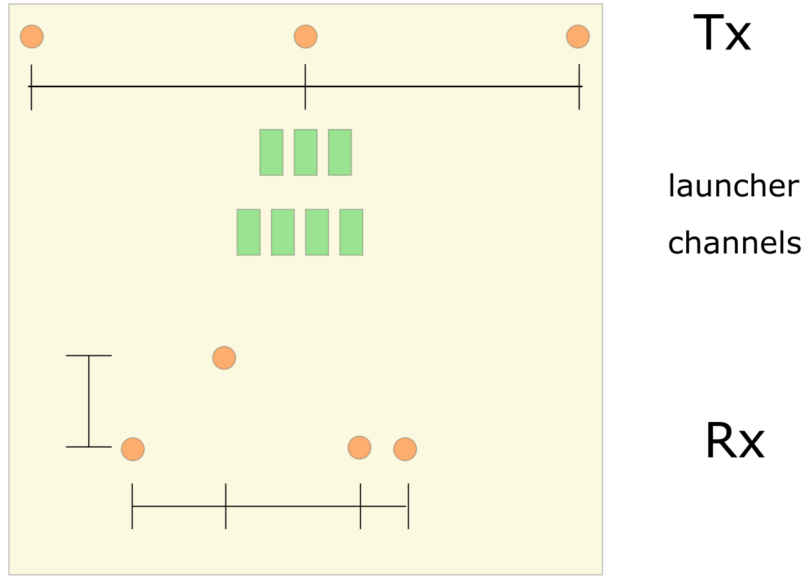


Figure 2.3: Tx and Rx phase center positions of the radar module have been determined by NXP software team. $\lambda = 3.9$ mm and the minimum distance between two antennas is $\lambda/2 = 1.95$ mm.

Table 2.2: Slotted waveguide antenna array target performance parameters.

Parameter	Target
Frequency range	76-77 GHz
Gain	≥ 16 dBi
Side Lobe Level	≤ -19 dB
Field of View in azimuth @-3 dB	70°
Field of View in elevation @-3 dB	16°
Isolation RxRx	≤ -20 dB
Isolation TxRx	≤ -35 dB

performance of the antennas, which is listed in Table 2.2. Additionally, the selected antennas have to be compact, low cost when manufactured in mass-production, and for the prototype it must be feasible to fabricate in a technology available at NXP or TU/e.

2.5 Planning

In order to accomplish the goals of this project, the following tasks need to be fulfilled:

- Update and finalize the LiP designed by Valeria Tapia [34], and characterize it in the laboratory.
- Design an antenna array, to be vertically mounted on top of the IC and LiP.
- Integrate the NXP IC, LiP and antenna array in a single cell unit and evaluate the system performance.

First, the identification of the problem and a literature review were conducted. Then, the update and finalization of the LiP design were addressed by re-optimizing according to updated design rules and later several samples of the LiP using a Vector Network Analyzer (VNA) were characterized. After that, the design and realization of a single-cell demonstrator, consisting of a single chip, launcher, and a regular antenna array, was performed.

Chapter 3

Launcher in package

A waveguide launcher in package for radar ICs is described in detail. The original design was developed as part of Valeria Tapia’s PDEng project [34]. Some re-optimizations are performed on the original design and, additionally, a model for higher frequencies is proposed. Both designs, with versions of dielectric and conductive interfaces were manufactured and their performance was characterized in the laboratory. These results are discussed here as well.

3.1 Launcher principle of operation

The proposed launcher is a device that aims to efficiently couple the power from the radar IC to a standard waveguide and from the waveguide to the IC. In this case, the waveguide standard is WR-10 (75 – 110 GHz). It is meant to be a low-cost, low-loss, high-isolation solution and is intended for car radar applications. The IC used for this design is the TEF810X or *Dolphin* chip designed by NXP, as it was commented in Section 2.4.1.

Standard solutions to integrate an IC and a waveguide either consist of a PCB transition from IC to waveguide, or is achieved by placing the IC inside the waveguide. The first option is not compact and, due to several transitions, losses are high [35, 36]. The second option has very low losses, but it only allows for single-channel operation. A third option is to directly integrate both, the package and the waveguide, thus achieving good performance and low losses. Nevertheless, this solution is expensive [37].

The design proposed here, for integration of IC and waveguide, is thus a novel approach. Several solutions were analyzed and discarded in [34] and [38]. The launcher design that was chosen to be manufactured and tested is described here.

The device must be capable of transporting power from the bottom of the package to the top, allowing for a vertical integration of waveguide and antenna array, as explained in Chapter 2. Then, the launcher must couple the power to the waveguide, as shown previously in Figure 2.1. In more detail, the power from the IC comes out of a pad where a differential coaxial line transfers it to a loop inside a shielded cavity and then the power is transferred to the waveguide on top.

3.2 Launcher design specification goals

In order to allow radar solutions in middle and entry-level cars, each of the components must be low cost. To comply with this requirement, the use of standard WR-10 waveguides

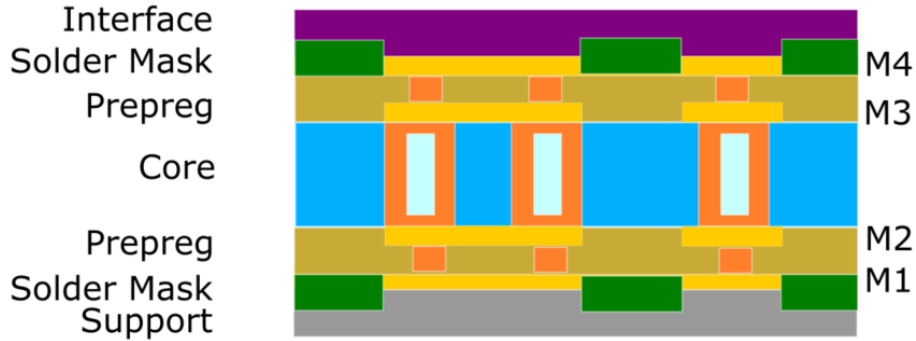


Figure 3.1: Conceptual scheme of dielectric and metal layers for laminate manufacturing technology designs [34] (lateral view). PTH and μ Vias are used to connect metal layers M1 to M4.

was selected, allowing for mass production and the flexibility to allocate different antenna configurations according to the needs of several clients. Also, the launcher design must reflect that the final device will be manufactured using standard IC procedures to reduce the costs.

In terms of electrical performance, losses must be low to maximize transmission and reception levels for a fixed input power. The goal is to achieve better performance than the one achieved by using standard PCB transitions. Reflections must be under -15 dB and transmission losses under 2 dB. Keeping isolation between channels lower than -30 dB guarantees less interference and thus better performance once the radar is identifying a target. These parameters were already summarized in Table 2.1.

3.3 Launcher and waveguide fan-out design

By the end of her PDEng project [34], Valeria Tapia designed a device based on a supplier-proprietary assembly technology, which is used for 3D system integration of chips. This technology has low losses, medium thermal resistance and medium cost, feasible for a demonstrator, but not for a final mass-production solution. It consists of a stack of substrates and metal layers that can be connected with Plated Through Holes (PTH) and μ Vias, as can be seen in Figure 3.1. There are several design rules, as the dimensions of the PTH and μ Vias, the separation between the vias, the width of the metal traces and minimum distance between traces. A summary of the design rules and parameters used for the final design are listed in Table 3.1 and Table 3.2.

Because of changes in design rules of the manufacturing company, i.e. the diameter of the μ Vias and the minimum spacing allowed between traces, the design had to be re-optimized. As the thicknesses of the substrates are fixed, only changes in the xy direction shown in Figure 3.1 were allowed. The goal was then to minimize transmission losses and reflections by changing the size and shape of the loop launchers shown in Figure 3.2. In parallel, an additional model for higher frequencies, targeted at 90-110 GHz, was designed to be manufactured and tested in parallel. However, for this model there was no yet an existing IC to connect to, so it was taken as a proof of concept.

For each frequency band, i.e. 77 and 100 GHz, two versions of the launcher were designed: with a dielectric and with a conductive interface, as shown in the purple layer in Figure 3.1.

Table 3.1: Design rules used for the design of the launcher: layer thicknesses and electrical properties. Some values are sensitive information and they have been removed on purpose. * Measured at NXP, ** Supplier information.

Layer	Material	Thickness	ϵ_r	$\tan \delta$
Interface	RO4450F	0.101 mm	3.52	0.004
Solder Mask	-	fixed	*	*
Prepreg (PPG)	-	fixed	**	**
Core	-	fixed	**	**
Base support	FR4	1.6 mm	3.9	0.018
Metal Layer (M1, M2, M3 and M4)	Copper	fixed	-	-

Table 3.2: Design rules used for the design of the launcher: minimum spacing and dimensions. The values are sensitive information and they have been removed on purpose.

Property	Target
PTH to PTH pitch (different net)	more than
PTH to PTH pitch (same net)	more than
μ Vias diameter	fixed
μ Vias capture pad diameter	fixed
PTH diameter	fixed
PTH capture pad diameter	fixed
Trace min width	more than
Trace to trace min spacing	more than
Plane to plane min spacing	more than
Capture pad to capture pad min spacing	more than

The interface between the launcher and the waveguide compensates for micrometers of deformation when pressure is applied to the launcher device against the waveguide. A conductive elastic layer with holes that perfectly match the dimension of the WR-10 standard waveguide should ideally show better performance, because there will not be dielectric losses associated with it. However, a uniform layer of dielectric material is easier to implement and assemble. A re-optimized loop launcher design must be made for each dielectric or conductive interface, thus having a total of four models to be implemented and tested.

The final model will need seven (3Tx+4Rx) launchers, one for each channel of the IC. However, in order to test the performance of the device, a passive back-to-back model, connecting two mirrored launchers and duplicating them was conceived, see Figure 3.2. By connecting this 4-channel model to a VNA, a characterization of the S-parameters can be performed, to obtain reflection, transmission loss and isolation.

On top of the back-to-back launcher device, a waveguide fan-out structure is intended to connect the 4 channels of the launcher to the VNA, allowing enough space for standard waveguide connectors and loads, see Figure 3.3. The performance of this waveguide fan-out device is presented in Figure 3.4. Simulations on this device reveal that the reflections are lower than -30 dB and transmission losses are lower than 0.004 dB for the 76-81 GHz car radar band when using a perfect conductor material. The waveguide fan-out should therefore not add major losses to the launcher besides the material. Higher losses are expected for

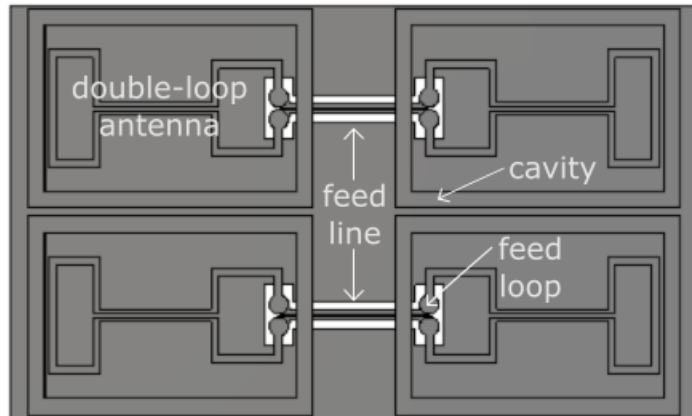


Figure 3.2: Top view of the back-to-back model of the 77 GHz launcher with conductive interface.

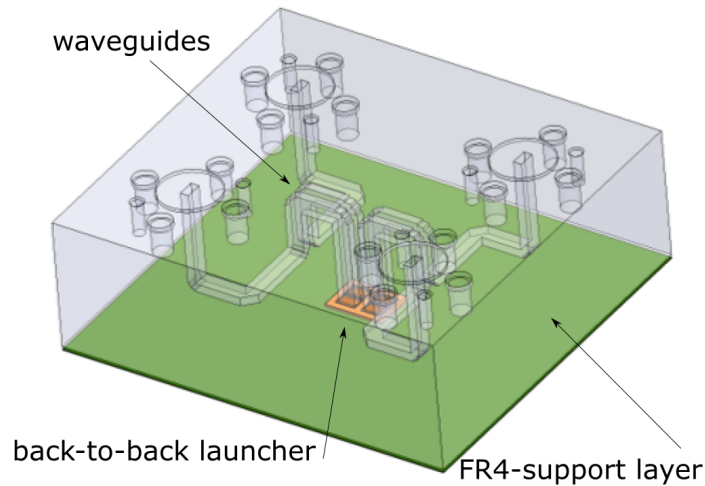


Figure 3.3: Final model of the launcher and waveguide to be manufactured and tested. The orange structure at the bottom is the 4-channel back-to-back launcher. Each channel is connected to a standard WR-10 waveguide.

a realistic material with finite conductivity and this effect will be shown in the following sections, when compared with measurement results.

The model to be tested consists of a waveguide fan-out structure with 4 ports. At the bottom, the 4-channel back-to-back launcher device is connected, as shown in Figure 3.3. As explained before, there are 4 versions of the launcher: 77 GHz with dielectric interface in between the waveguide and the cavity, 77 GHz with conductive interface in between the waveguide and the cavity, 100 GHz with dielectric interface in between the waveguide and the cavity, 100 GHz with conductive interface in between the waveguide and the cavity.

The dimensions for all models were optimized in CST Studio Suite [39] and the differences between them are the size of the cavity, i.e. smaller for the higher frequency model, and the size and shape of the loop launcher. Double loop launchers were used for the 77 GHz model and single loop launchers for the 100 GHz model. The addition of the second loop in the lower

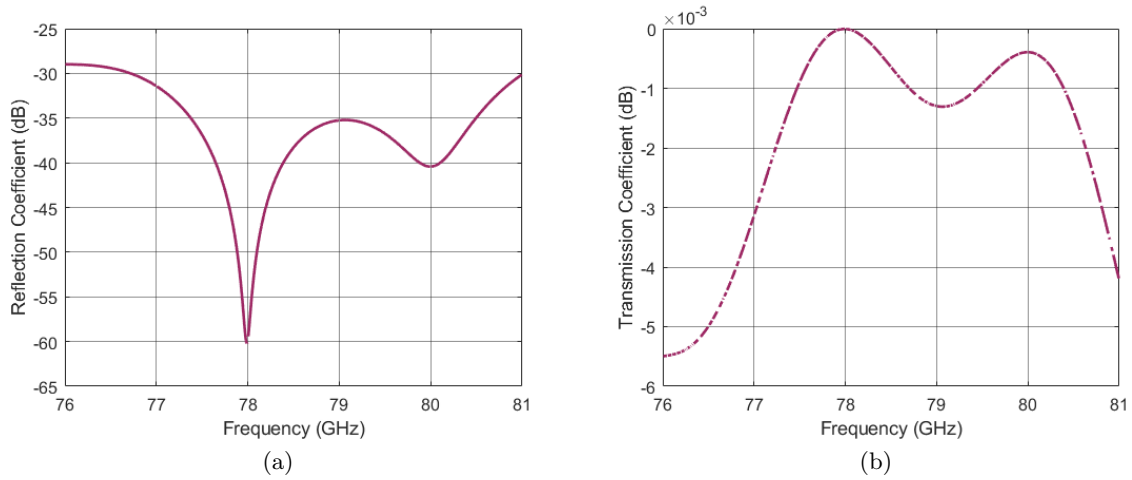


Figure 3.4: Waveguide fan-out performance as a standalone device simulated for 76-81 GHz.

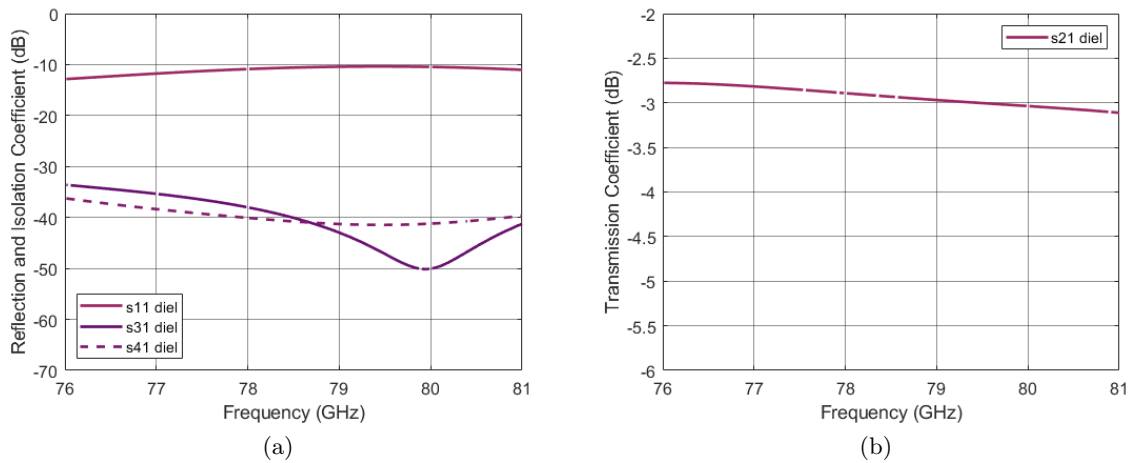


Figure 3.5: Simulated performance of the 77 GHz launcher with dielectric interface.

frequency model was due to the need for a larger bandwidth. More details on this design can be found in [34].

The simulation results for the 4-channel back-to-back models are shown in Figure 3.5 and Figure 3.6. The 77 GHz model has a reflection coefficient lower than -10 dB and transmission losses lower than 3.1 dB. The 100 GHz model has reflections lower than -10 dB between 95-105 GHz and transmission losses lower than 5.5 dB. Isolation level is lower than -30 dB in both cases. Even though the reflection and transmission loss is higher than the target, a model based on less restrictive design rules could be produced as long as the concept shows to be successful, by meeting the simulation expectation. The previous model optimized by Valeria Tapia [34] based on another set of design rules but the same concept, did meet the required performance.

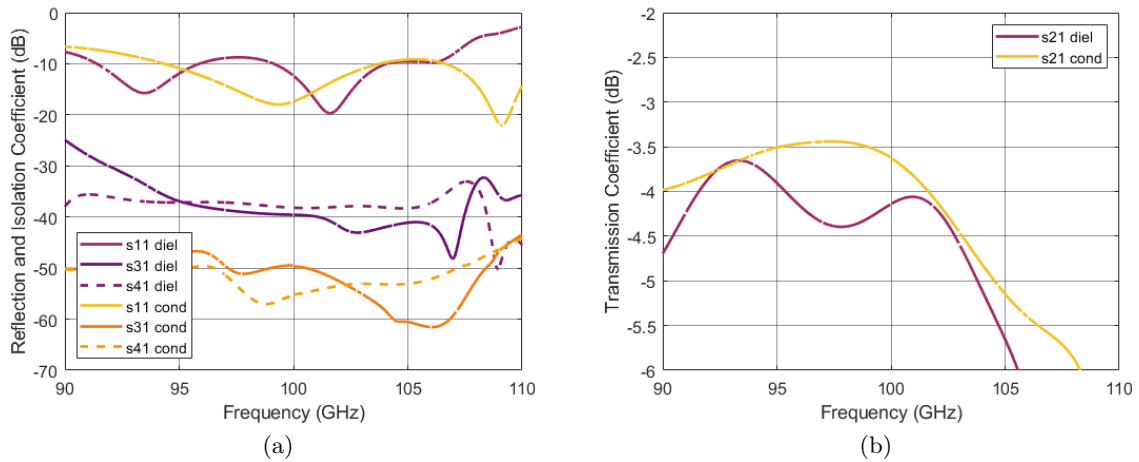


Figure 3.6: Simulated performance of the 100 GHz launcher.

3.4 Launcher and waveguide fan-out fabrication

The back-to-back 4-channel launcher was manufactured and assembled by external companies, commissioned by NXP. The waveguide fan-out was machined internally at TU/e at the Equipment and Prototype Center (EPC) workshop. Some general characteristics of the processes are discussed below.

3.4.1 Launcher

As mentioned before, the launcher was fabricated using laminate manufacturing technology based on stacked materials. After the simulated model was agreed upon as the final design, a .gds file of each of the layers was exported directly from CST. Afterwards, an engineer at NXP prepared a proper layout to be sent to the external companies. Then, after a few iterations, the design was ready to be manufactured. Each back-to-back launcher device was implemented in a laminate of size 9.55×9.09 mm, and a thickness of 0.45 mm. Figure 3.7 show an example of the manufactured launcher demonstrators.

3.4.2 Waveguide fan-out

In the waveguide fan-out, the waveguides have to go from as close as 1 mm between themselves (output of the launchers) up to a separation of 30 mm in order to accommodate connectors when measuring with the VNA. For that reason, and because of the milling technology used for manufacturing it, a model in three layers with bends was conceived, as shown in Figure 3.8. Each layer should be milled from one side only to maintain accuracy. Then, the three layers are put together using alignment pins and screws. For the purpose of reducing losses, a metal with good conductivity and low oxidation levels was selected. In this case, the chosen material was brass, which also has good mechanical properties in terms of robustness and ease of machining. Additionally, after milling, a lapping procedure had to be applied to all contact surfaces to reduce air-gaps between layers. This was done after realizing that the losses were higher than expected.

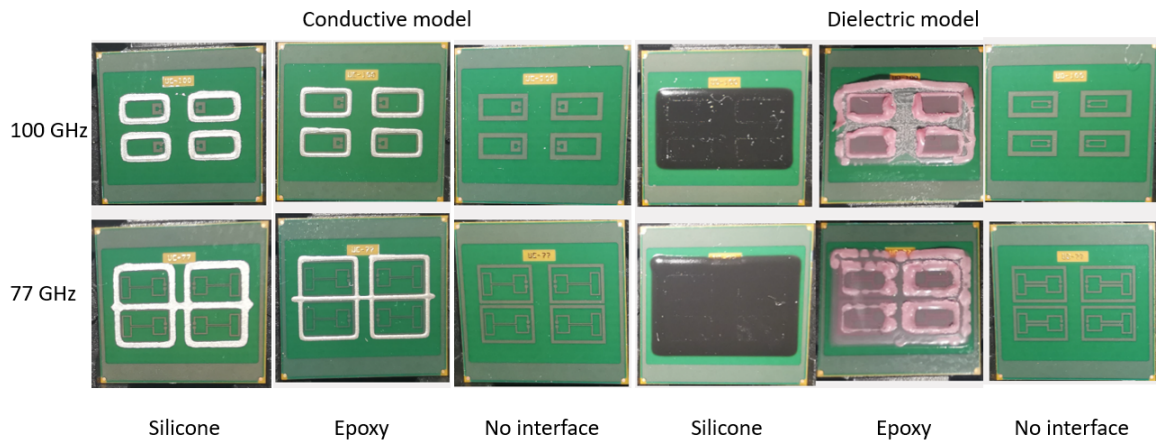


Figure 3.7: Final model of the launcher in package. Different models were designed for 77 and 100 GHz and for a conductive and dielectric interface layer.

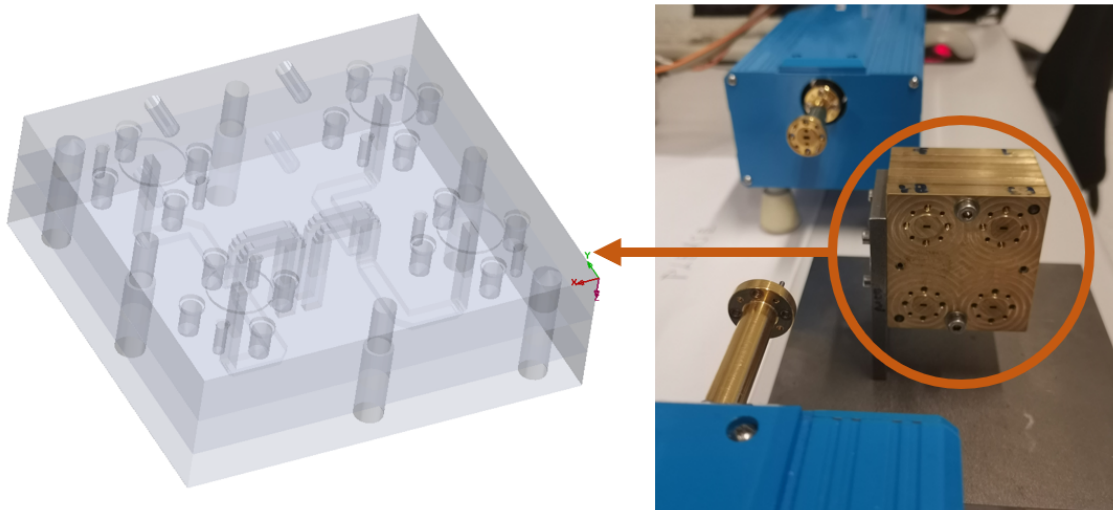


Figure 3.8: Final model of the waveguide fan-out. Four channels allow access to the two launchers connected back-to-back.

3.5 Measurements of launcher and waveguide fan-out

With the purpose of characterizing the launcher as a passive device, the back-to-back configuration was selected. In this way, the device, through the waveguide fan-out, can be connected to the VNA ports to retrieve the S-parameters. S11 gives information on the reflection, S21 on the transmission losses, S31 and S41 on the isolation between adjacent and opposite channels.

3.5.1 Measurement strategy

As the VNA ports are of coaxial-type, some transitions and additional considerations were needed. There are two VNAs available at TU/e to measure the performance of the launcher structure inside the waveguide fab-out. On the one hand, the Electromagnetics (EM) group has a 2-port VNA with extenders capable of measuring up to 90 GHz with rectangular WR12 waveguide terminations. On the other hand, the IC group has a VNA with extenders to cover 90-140 GHz, terminated in WR8. As the waveguide fan-out was designed for a WR10 standard waveguide, transitions from WR8 to WR10 and WR12 to WR10 were bought. Also, to calibrate the measurement setup, a WR10 load, short and delay-line were ordered to facilitate a Thru-Reflect-Line (TRL) calibration. By performing repeated calibrations and measurements, the reproducibility of the test setup and calibration can be assessed. The performance of the waveguide fan-out, without launcher connections, will also be characterized using a VNA. In this way, when post processing the data of the launchers, the influence of the performance of the waveguide can be considered for a final conclusion on the performance of the launcher.

As shown in Figure 3.9, S11, S22, S33 and S44 allow to retrieve the reflection of each channel. They are all expected to be equivalent and similar to what is shown in Figure 3.5 and Figure 3.6, respectively. S12 and S34 (and S21 and S43) give information on the transmission losses. Especially for this measurement, the double path traveled needs to be taken into account when analyzing the losses, as those are doubled for the back-to-back model than for the stand-alone device. Finally, by measuring S13 and S24 (and S31 and S42) the adjacent isolation is obtained and by measuring S14 and S23 (and S41 and S32) the opposite or diagonal isolation is obtained.

3.5.2 Measurement results

Several measurements were conducted to characterize the launcher performance and the behavior of the different interfaces to identify the combination that shows a good compromise in between low losses and reliability, for which the selected interface plays a big role. S-parameter measurements show the performance of the launcher and they can be compared with simulations. Additionally, insights about the preferred interface material can be obtained after performing repeatability and pressure tests, showing which type of interface is more suitable for a car radar.

The result of the measurements on the waveguide fan-out in a back-to-back configuration, without inserting the launcher device, is shown in Figure 3.10. Transmission losses are 1.5 - 1.7 dB in the frequency range of 76 - 81 GHz, for a path length of 14 cm. This result is used for de-embedding the losses when measuring the launcher located at the bottom of the waveguide fan-out. Reflection is lower than -12 dB and isolation lower than -50 dB, as expected.

The results of the measurement on each launcher type: 77 and 100 GHz model without interface, or with conductive or dielectric interface, are shown in Figure 3.11 and Figure 3.12 and summarized in Table 3.3. Reflection and isolation results are as expected, but transmission losses are higher. Mostly for the 77 GHz model.

The real thickness of the interfaces was measured and it was found that the silicon dielectric interface is 50 μm thicker than the simulated material. By adjusting the parameters in the simulation to fit the measured results, ϵ_r and $\tan \delta$ of the measured materials were

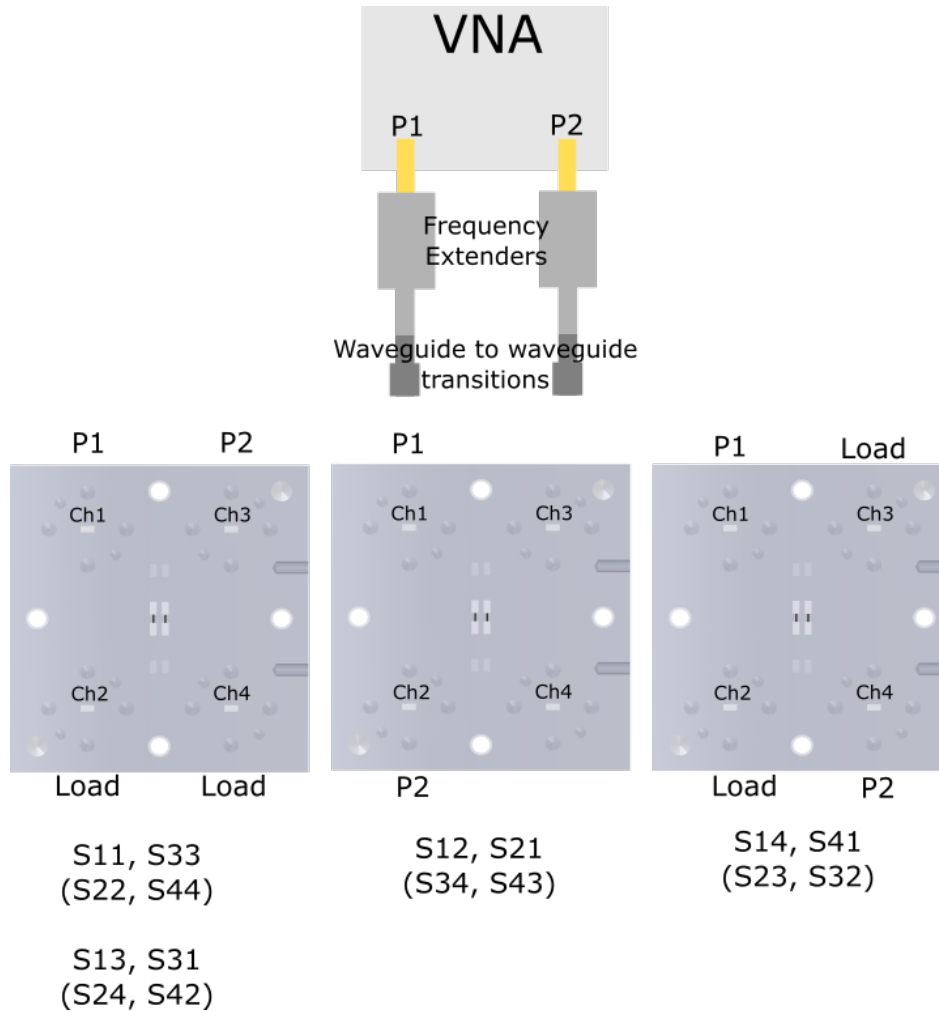


Figure 3.9: Measurement connections to characterize launcher S-parameters. At the top, the measurement set up from the VNA to the waveguide transition is presented. At the bottom, the top view of the model in three different scenarios is shown. Left one is used to measure reflection loss and isolation between lateral channels, the middle one is used to measure transmission loss and the one in the right side is used to measure isolation between diagonal channels.

estimated. The results are shown in Table 3.4, together with the measured thicknesses of the interfaces.

Finally, the influence of pressure applied to the launcher on the performance was characterized. Differences of about $5 \mu\text{m}$ were encountered between a reference point and the optimum. Additional results are shown in Appendix B.

3.5.3 Analysis of results

The mechanical performance of the interface made with silicone material is better than the one made with epoxy, as the former is elastic and keeps its original shape. The epoxy material leaves residuals when pressure is applied against a metallic waveguide. Electrical performance

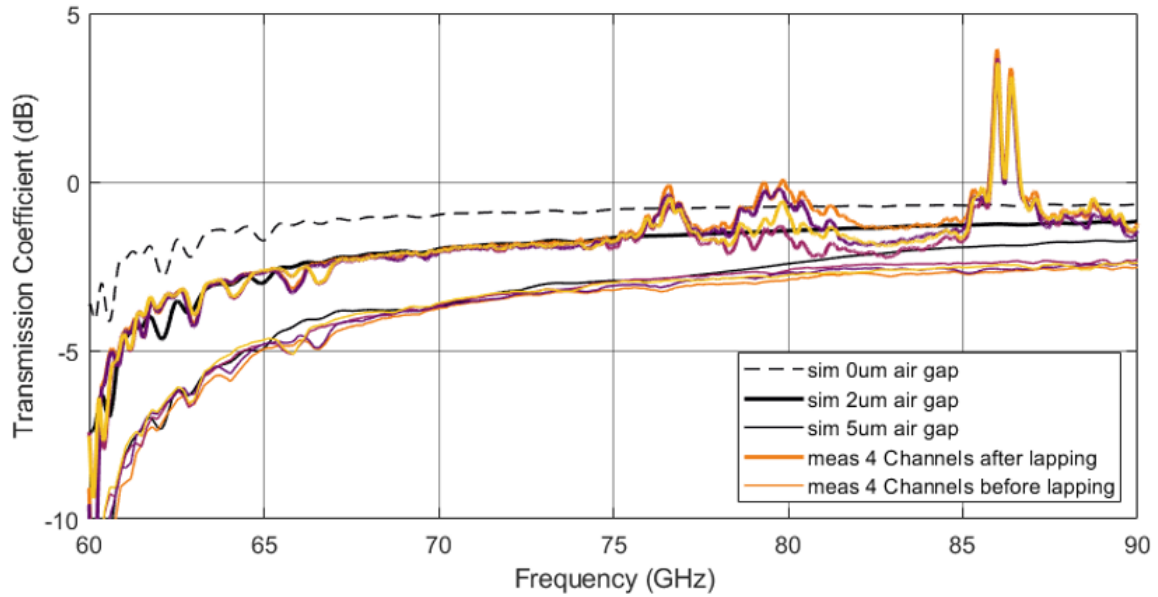


Figure 3.10: Waveguide fan-out performance. Measurements with 2-port VNA and comparison with the CST simulation. A misscalibration of the measurement setup provokes ripples in between 75-90 GHz. The black solid curve fits the expected behavior.

Table 3.3: Launcher performance summary for the range 76 - 81 GHz.

Launcher type	Trans. Loss [dB]	Ref. Loss [dB] (less than)	Iso. Adjacent [dB] (less than)	Iso. Diagonal [dB] (less than)
77 GHz conductive no deposit	4.5 - 6.3	10.9	45.3	43.1
77 GHz conductive silicone	5.6 - 10.5	4.4	35.2	41.2
77 GHz conductive epoxy	5.3 - 8.1	5.4	32.9	40.0
77 GHz dielectric no deposit	14.8 - 17.7	4.3	44.2	52.6
77 GHz dielectric silicone	5.2 - 5.5	8.7	34	32
77 GHz dielectric epoxy	4.6 - 5.5	8.0	35	32
100 GHz conductive no deposit	3.0 - 4.5	7.5	32.2	33.0
100 GHz conductive silicone	3.0 - 4.5	7.5	36.9	43.2
100 GHz conductive epoxy	3.6 - 4.5	7.6	36.9	46.5
100 GHz dielectric no deposit	3.3 - 4.4	9.2	34.0	40.6
100 GHz dielectric silicone	5.1 - 8.4	11.2	28.3	32.5
100 GHz dielectric epoxy	4.2 - 6.0	11.2	28.7	32.5

for both materials is similar. Both show higher losses than expected, comparable with a material with a $\tan \delta$ of 0.06 instead of the simulated 0.004.

The silicon interface shows less spread in the results. In other words, the silicon interface makes the model more robust to differences in pressure and is then more reliable. Launcher measurements are repeatable. This applies to assembly and disassembly of the same unit or measuring different units of the same type.

Table 3.4: Properties of interfaces materials.

Interface type	Thickness [μm]	Estimated ϵ_r	Estimated $\tan \delta$
Silicon conductive	20	N/A	N/A
Epoxy conductive	50	N/A	N/A
Silicon dielectric	150	3.52	0.05
Epoxy dielectric	not measured	3.52	0.05

Conductive models perform best with maximum pressure applied against the launcher. On the contrary, dielectric models perform best with medium pressure.

The 100 GHz models match better with the simulations than the 77 GHz models. One possible cause for this is that the double loop design is more sensitive, because the spacing between the loop and the cavity is small. In general, dielectric models did not match the simulations because the material has a higher loss tangent than expected. Dielectric material interfaces allow for an increased bandwidth, but due to the material properties they exhibit higher losses. Also, as the dielectric material is thicker, the isolation is worse than for models with conductive interface.

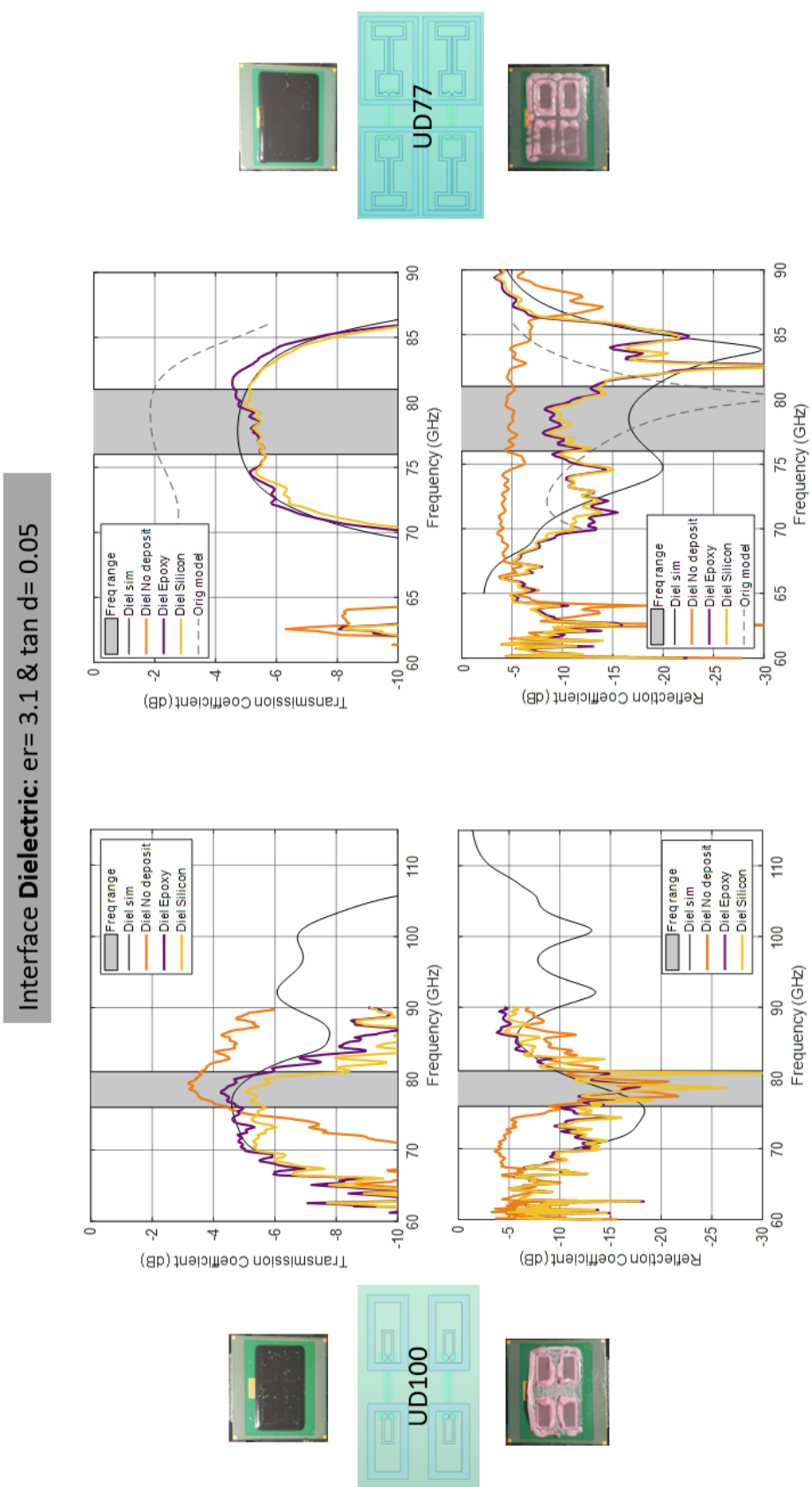


Figure 3.11: Dielectric layer launcher performance. Measurements with 2-port VNA and comparison with CST simulation.

Interface Conductive: $\sigma = 2.5E4 \text{ S/m}$

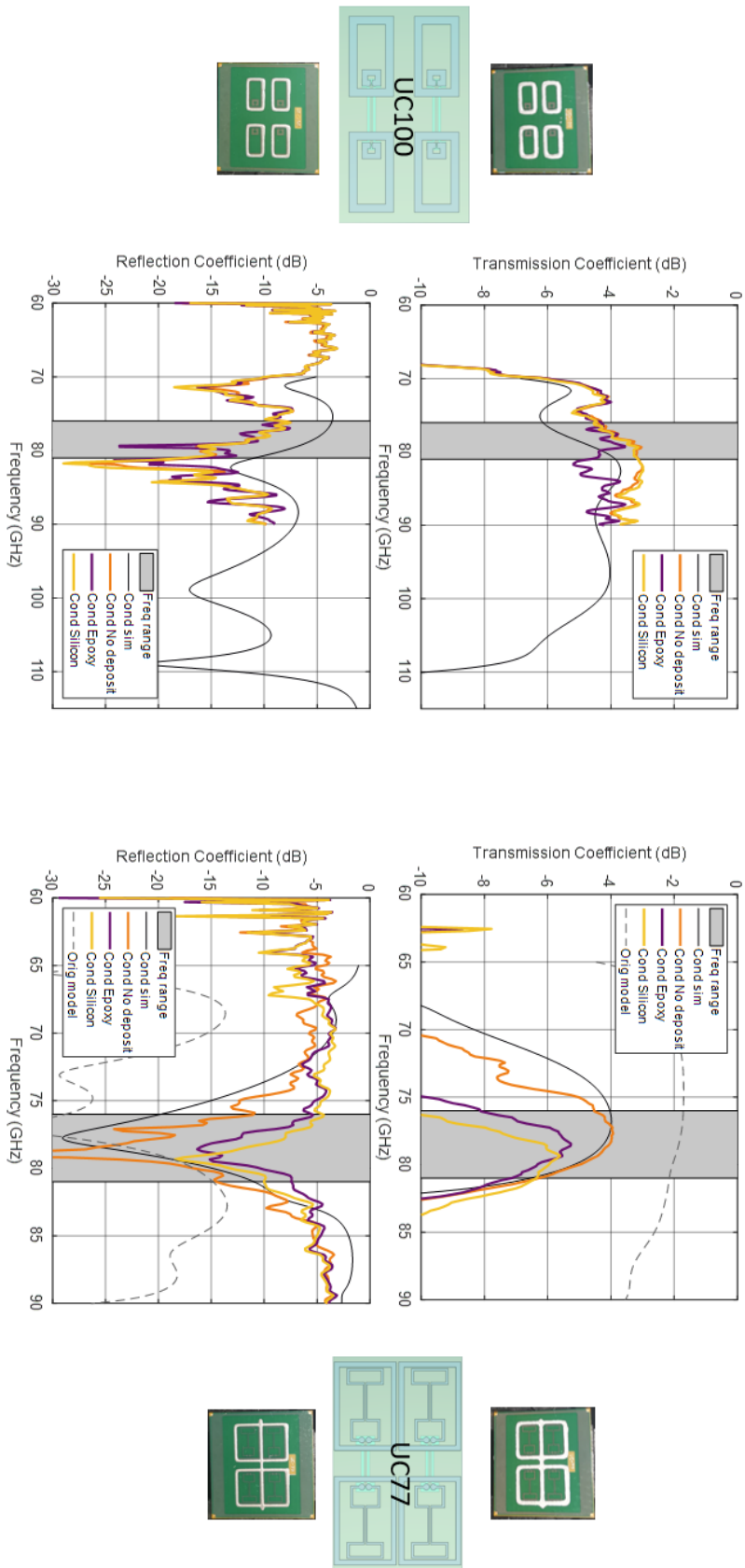


Figure 3.12: Conductive layer launcher performance. Measurements with 2-port VNA and comparison with CST simulation.

3.6 Conclusions

Four launcher designs were proposed, two of them are re-optimized versions of the 77 GHz launcher with dielectric and conductive interface and the other two are new higher-frequency versions that keep the same concept of a cavity with loop launcher. Laminate manufacturing technology was selected for these demonstrators devices. In order to test them as passive devices, a back-to-back configuration was used. Mirrored models of each launcher were connected through a differential feed-line and replicated to the side, thus achieving a 4-channel passive device. On top of this structure, a waveguide fan-out, designed in three layers, was used to allow placement of standard WR10 connectors on each flange.

All designs achieve good performance in simulation and measurements. Some discrepancies in measurements with respect to simulations were found. The waveguide fan-out structure had to go to a lapping procedure to polish the surfaces for reducing extra air gaps. The dielectric material of the launcher interfaces exhibited higher losses than expected because it was thicker and the loss tangent was higher. For a single path, after de-embedding the extra losses due to the waveguides, the transmission loss of the launcher is lower than 2.5 dB, isolation level is lower than -30 dB and reflection loss better than 10 dB. The concept shows an acceptable performance and there is room for improvement. By using a less lossy material, a total transmission loss of even 1 dB could be obtained.

The different interfaces behave differently. The preferred materials are silicone based, because the behavior is less sensitive to the applied pressure and it is also more repeatable. Pressure applied is most relevant for the launcher without interface, but when maximum pressure is applied, the performance is optimum. Epoxy material also shows mechanical issues, due to the fact that it sticks to the metal waveguide and it deforms too much.

Chapter 4

Slotted-waveguide antenna array

In 1946-1947 Watson [40] investigated how a slot cut in the wall of a rectangular waveguide was producing radiation by interrupting the currents on the inner surface of the waveguide. Later on, Stevenson [41] found an expression for the conductance of a slot when modeling the electromagnetic propagation by transmission lines and lumped elements formalism. Other researchers [42, 43] made further improvements on those expressions, making them more accurate by including the effect of the exact geometry of the waveguide and the internal storage of energy. In [44], Oliner described a method for determining the impedance of different types of slots. After that initial period of investigation of slotted-waveguide antennas, several examples have been produced for different applications and especially for navigation systems and radar [45, 46]. They are an attractive option because of the high antenna efficiency, ease of construction and compact shape. Also, slotted-waveguide antennas provide flexibility in controlling the beam shape according to the disposition of the slots [47].

During an ongoing project at NXP, it was decided to design slotted-waveguide antennas for a BSD radar module consisting of three Tx and four Rx channels. In parallel to this PDEng project, a six-slot antenna array was designed according to requirements already explained in Chapter 2. That antenna design was transversely polarized and there was a need to compare the performance with a longitudinally polarized concept. The design of each of the functional components of a longitudinally polarized slot antenna and the comparison between the two possible designs is presented in this chapter.

4.1 Antenna specification goals and constraints

The goal performance parameters of the slotted-waveguide are set based on the recognition software, as explained in Chapter 2. The position of each slotted-waveguide is fixed and each slotted-waveguide should provide a gain of 16 dBi or more and a maximum side-lobe level of -19 dB, as summarized in Table 2.2.

The transversely polarized slot array, that was designed in parallel, achieves these performance parameters, but the required structure is complex and not straightforward to fabricate. In order to find a simpler alternative and reduce the cost of the module, a second design, based on a longitudinally polarized antenna is the goal in this part of the project.

In principle, the waveguide must be based on the WR-10 standard. At least at the input, which is connected to the launcher, it has to be of dimensions 1.27×2.54 mm. Due to the space constraint, the slotted-waveguide antenna must be shorter than 30 mm.

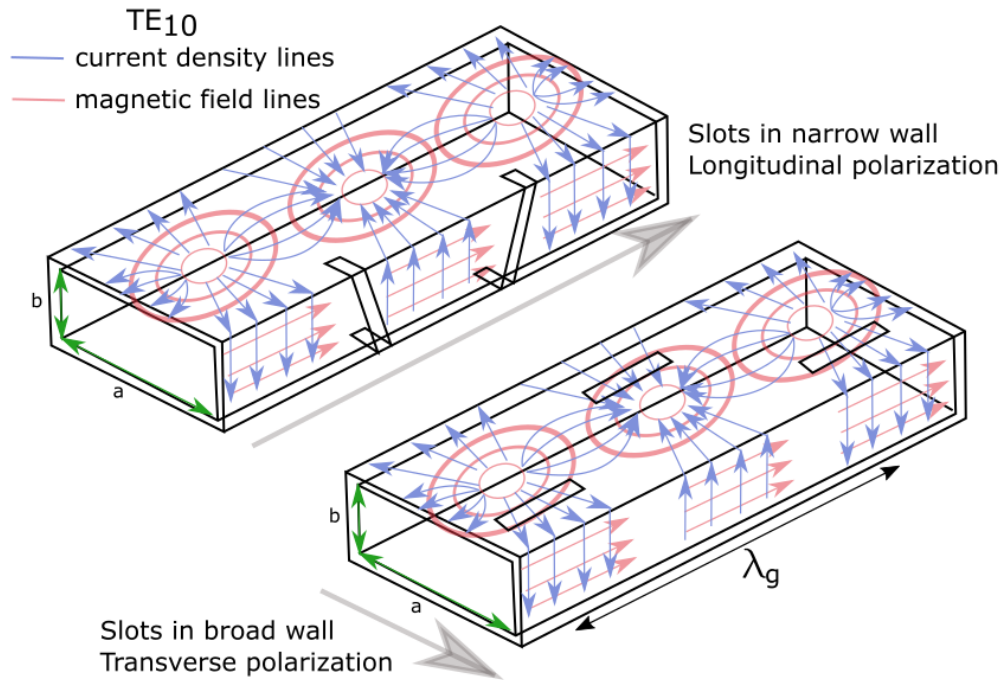


Figure 4.1: Magnetic field and electric current lines associated with rectangular waveguide mode TE₁₀. Slots cut in the broad wall provide a transverse or horizontal polarization and slots cut in the narrow wall provide a longitudinal or vertical polarization. Image adapted from [49, 50]

4.2 Slotted-waveguide antenna theoretical model

The type of slotted-waveguide antenna considered here consists of a waveguide with an array of slots cut in the narrow or broad wall. The slots, when properly designed, interrupt the currents flowing at the surface of the waveguide wall, thus producing electromagnetic radiation similarly as for a magnetic dipole antenna. The direction of the electric current density lines are perpendicular to the magnetic field lines, as shown in Figure 4.1, thus when the electric current is perpendicular to the slot axis, the excitation in the slot is in its maximum limit because the magnetic field is aligned with the slot, and the slot will radiate as a magnetic dipole. When the direction of the electric current density lines are parallel to the slot axis, there is no excitation in the slot. The selection of the wall on which the slots will be allocated will then determine the disposition of the slots along the wall [40, 48].

Taking into account the dominant TE₁₀ mode in a rectangular waveguide [49], for broad-wall slots, the slots should be arranged longitudinally [51, 52] as shown in Figure 4.1. To increase the excitation of the radiated fields, the slots cut in the broad wall can be moved towards the edge of the waveguide. For narrow-wall models, the optimum way to radiate is to cut a slot at a slanted angle [53, 54, 55], as shown in Figure 4.1. To control the excitation, the tilting angle of the slot can be used. Zero tilting will yield no excitation and a larger angle will produce more excitation. In both cases, if the spacing in between slots is half the wavelength

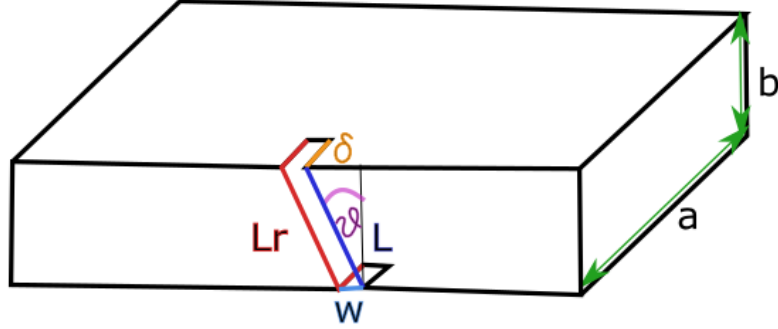


Figure 4.2: Longitudinally polarized slotted-waveguide design parameters. L_r in red, is the resonant length, L in blue, is the length of the slot cut in the narrow wall δ in orange, is the part of the slot cut into the broad wall, w in light-blue, is the width of the slot and θ in purple, is the inclination angle of the slot.

inside the waveguide, i.e. half the guided wavelength $\lambda_g/2$ pertaining to the dominant mode, a radiation pattern based on constructive interference will be created, equivalent to the case of an array of dipoles. The guided wavelength is defined as:

$$\lambda_g = \frac{\lambda_0}{\sqrt{1 - \left(\frac{\lambda_0}{2a}\right)^2}}. \quad (4.1)$$

Where $\lambda_0/2$ is the wavelength in free space for the design frequency and a is the longest edge of the waveguide cross-section, as shown in Figure 4.2.

A directive beam can be achieved with a large aperture containing an array of slots. If the spacing between slots is fixed to $\lambda_g/2$, then the more slots, the more directive the beam. Also, to reduce the side-lobe level of the pattern, the slot array can be designed in a specific way so that a tapered amplitude of conductances is produced [55, 56].

4.2.1 Longitudinally polarized slotted-waveguide antenna analytical model based on literature

The narrow-wall slanted slots produce a longitudinally polarized pattern [53, 54, 55]. The main design parameters of this type of slot array are: the angle of the slot, the width of the slot, the length of the slot and the total number of slots. All these parameters are represented in the scheme of Figure 4.2. Different approaches of slots done in the narrow wall of the waveguide were studied in [57, 58, 59] and they are different from inclined slots.

In order to have a real-valued conductance value, i.e. cancelling all susceptance components, the slot has to be as long as $L_r = 0.4625\lambda_0$, called radiation length [42]. Depending on the inclination angle θ , the radiation length can only be achieved by cutting the slot into the broad wall by δ [42]. The radiation length L_r , the length of the slot contained in the narrow wall L , the angle of the slot with respect to the vertical θ and the depth of the cut in the broad wall δ are related as [42]:

$$2\delta = L_r - L = 0.4625\lambda_0 - \frac{b}{\cos \theta}. \quad (4.2)$$

Where b is the shortest edge of the waveguide cross-section, as shown in Figure 4.2.

Angles $\theta < 45.6^\circ$ will always produce a slot that is cut into the broad wall. Larger angles produce slots that are fully contained in the narrow wall. An alternative for cutting into the broad wall was explored in Chapter 9 of [48], where instead of cutting the slots into the broad wall, a circular hole was created in the extremes to provide the needed resonant-length effect.

The conductance of a slot created in the narrow wall, normalized with respect to the wave impedance of the dominant TE₁₀ mode, can be written as [42]:

$$g_i = \frac{1}{2\pi} \frac{\lambda_0^4}{a^3 b} \frac{\lambda_g}{\lambda_0} \left(\frac{\sin(0.5\beta_{01}W \cos \theta)}{0.5\beta_{01}W \cos \theta} \right)^2 \left(\frac{\sin \theta}{1 - \left(\frac{\lambda_0}{\lambda_g} \sin \theta\right)^2} \right)^2 \quad (4.3)$$

$$\frac{(\cos(k\delta) \cos(0.5\beta_{01}L \sin \theta) - \cos(0.5kL_r) - \frac{\lambda_0}{\lambda_g} \sin \theta \sin(k\delta) \sin(0.5\beta_{01}L \sin \theta))^2}{\text{cin}(kL_r) + (\text{cin}(kL_r) - 0.5\text{cin}(2kL_r)) \cos(kL_r) - (\text{si}(kL_r) - 0.5\text{si}(2kL_r)) \sin(kL_r)}.$$

where

$$\text{si}(x) = \int_0^x \frac{\sin t}{t} dt, \quad (4.4)$$

$$\text{cin}(x) = \int_0^x \frac{1 - \cos t}{t} dt. \quad (4.5)$$

The parameters with the most influence in this equation are θ , L_r , L and δ . Nevertheless, L_r , L and δ are tied to the selection of the angle θ , so ultimately, θ is the main design parameter to determine the conductance.

The expression in Equation (4.3) does not take into account mutual coupling between two or more slots and the storage of energy in evanescent modes around the slot [43], but it does improve Stevenson's formula [41] by adding the effect of the cut δ into the broad wall of the waveguide [42]. For larger angles θ , the internal power storage decreases and thus the expression in Equation (4.3) becomes more accurate [43].

By adding several slots in a waveguide wall, an antenna with higher gain can be obtained. As shown in Figure 4.1, slots cut in the narrow wall have to have angles θ with alternating sign to obtain alternating phases each $\lambda_g/2$ [40]. An equivalent circuit of an array of slots is shown in Figure 4.3, where the slot array can be modeled as a parallel circuit with lumped elements and each conductance g_i represents a slot in the array [53]. If small resistance losses are assumed inside the waveguide, the equivalent conductance of a slot array can be estimated as:

$$g_{eq} = \sum_{i=1}^N g_i. \quad (4.6)$$

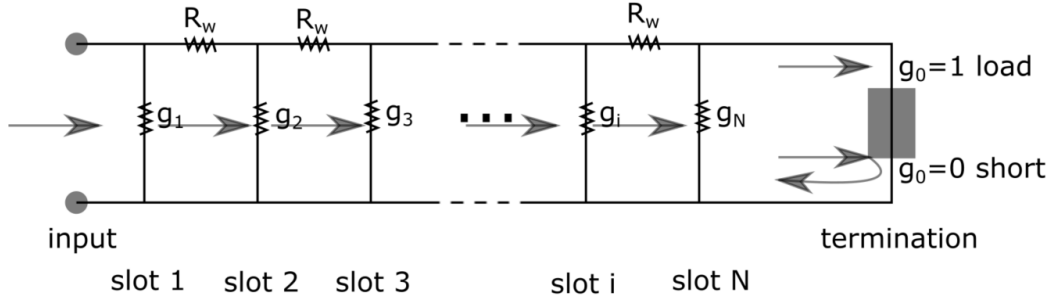


Figure 4.3: Equivalent circuit for a slot array. Each conductance g represents a slot cut in the waveguide. When the waveguide is terminated in a load, there is a travelling wave, and when the waveguide is terminated in a short, there is a standing wave. Image adapted from [53].

4.3 Longitudinally polarized slotted-waveguide antenna array design

Ideally, the designed slotted-waveguide antenna should have a reflection coefficient lower than -10 dB and a beam pattern that shows a gain > 16 dBi and a SLL < -19 dB over the frequency range of 76-77 GHz. Additionally, it should have the required field of view and isolation as it was shown in Table 2.2, and it will be fabricated at a low cost. Achieving all these properties is challenging and some trade-offs must be made through design choices. An overview of the different design possibilities is explained below and also shown in the scheme of Figure 4.4. They are: (1) how to feed the waveguide, (2) which type of wave will exist inside the waveguide, (3) what a single slot will look like and (4) how to arrange an array of slots. Once deciding all these aspects, a slotted-waveguide antenna has been designed. After that, a matching network has to be designed to connect the slotted-waveguide antenna to the waveguide openings on top of the seven channels of the launcher. Finally, to integrate each of the seven slotted-waveguide antennas, a beamforming network has to be designed, including a metal plane that will shield the radiation plane from all electronics placed below.

In the following sections, the frequency range in which the antenna achieves a reflection coefficient lower than -10 dB will be referred to as *impedance-matching frequency bandwidth* and the frequency range in which the antenna achieves a gain > 16 dBi and a SLL < -19 dB will be referred to as *beam-pattern frequency bandwidth*.

4.3.1 Feeding strategy

The simplest way to feed the slotted-waveguide is with a single 90° H-bend from one side, as shown in the left side of Figure 4.5. Another possibility is to feed the waveguide from the middle, as in a T-splitter configuration [60, 61], as shown on the right in Figure 4.5. The middle feed has the advantage of providing additional beam-pattern bandwidth at the cost of a more complex structure to fabricate because of the need for an additional H-bend. For longer waveguides, the effect of feeding from the middle becomes even more relevant.

As covering the frequency range of 76-77 GHz is required and ideally also covering until 81 GHz, it was decided to opt for a middle feed. The additional cost of it is related to extra

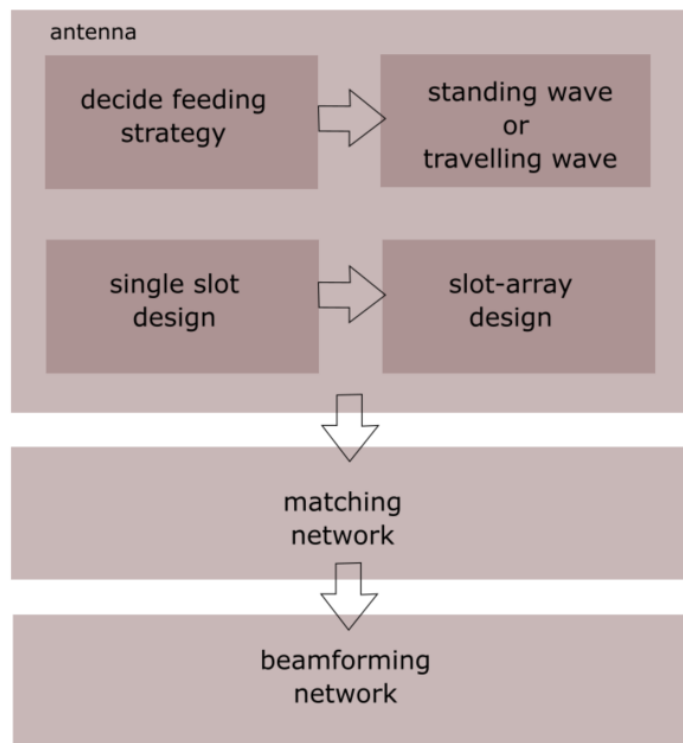


Figure 4.4: Design flow of a slotted-waveguide antenna.

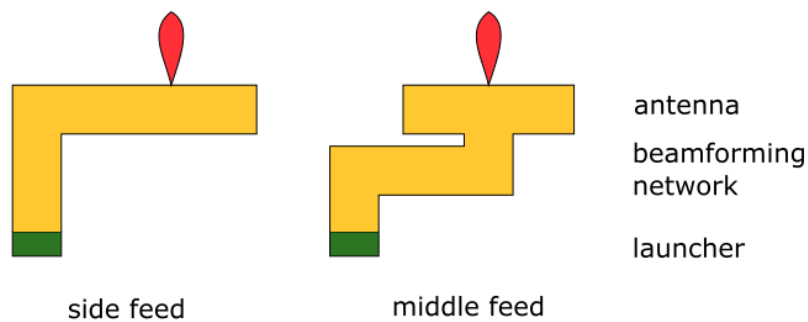


Figure 4.5: Schematic lateral view of a longitudinally polarized slotted-waveguide antenna fed from the side (left) and from the middle (right). The position of the launcher and the phase center of the radiation pattern is fixed, so the beamforming network has to be adapted to those positions.

layers needed to fabricate this device. Nevertheless, this is only required for a demonstrator as a final product could be made by using a mold and in that case the extra cost is minimal. Beam-pattern simulation results obtained for a slotted-waveguide antenna with a side feed can be found in Appendix C.

4.3.2 Travelling wave vs standing wave

The slotted-waveguide antenna can be designed under the principle of a travelling wave or a standing wave. A travelling wave will need either a load at the end of the waveguide or that the waveguide is long enough such that the power will decay towards the end. A standing wave will be produced when the ends are short circuited. A scheme including the equivalent circuit in both scenarios was shown in Figure 4.3.

As the available space for the BSD module is not enough to have a long waveguide, the decision of having a travelling wave or a standing wave depends on the type of waveguide end. The use of a load was discarded because even though it provides a better starting point to perform the impedance matching, there is significant loss of power in the load and one of the most important goals of this project is to minimize losses. A standing wave will imply a high Q value due to the energy storage inside the cavity, resulting in a low resistance over the whole frequency range, except for a region in which both the imaginary and real component are high. Results obtained with a matched load can be found in Appendix C. A travelling wave slotted-waveguide antenna with high performance is demonstrated in [50].

4.3.3 Single-slot design

After the preceding two decisions, meaning, feed the waveguide from the middle and have the waveguide with a shorted end, the remaining design choices for an antenna design are how a single slot will look like and how to distribute an array of slots. CST Microwave Studio (CST) was used as a tool to simulate the RF performance of the different structures. Brass with a conductivity of 2.74×10^7 S/m was used for all models.

In principle, for a slanted slot cut in the narrow wall the selection of the angle of the slot θ is arbitrary, as long as the resonant length L_r complies with Equation (4.2). However, depending on the selection of the angle θ some particular properties arise. It has been empirically found, and also confirmed in literature [55, 54, 40], that to obtain a high antenna efficiency, the normalized conductance of the slot shown in Equation (4.3) has to be < 0.1 . This maps to an angle of around 15° . Nevertheless, the larger the angle, the more radiated power, as explained in Section 4.2. More radiated power will imply less energy stored in the waveguide cavity and thus a less resonant behavior, which will provide a model that is easier to match. This is because the input impedance of the antenna will be more constant over the frequency range.

An angle of 15° was selected to initialize the design. For the design frequency of 76.5 GHz, this angle corresponds to the values of $L_r = 1.8$ mm, $\delta = 0.25$ mm and $L = 1.3$ mm based on Equation (4.2) and $w = 0.2$ mm was decided upon, based on manufacturing feasibility. The normalized conductance of this slot is 0.12 based on Equation (4.3). The wave impedance of the TE₁₀ mode is $Z_0 = 592 \Omega$ at 76.5 GHz.

4.3.4 Slot-array design

As explained in Section 4.2, the slots cut in the narrow wall have to be alternating in angles. Due to the available space and the need to radiate as much power as possible, it was decided to cut six slots, the maximum possible number separated by $\lambda_g/2$ from each other. So initially, the slotted-waveguide antenna consists of six θ -alternated slots cut in the narrow wall.

For the feed from the middle there is an additional concept to be taken into account for the design. Because the wave is going to be split in the middle, going half to the right side and half to the left side, there has to be a tilt in 180° in the slots located on one of the

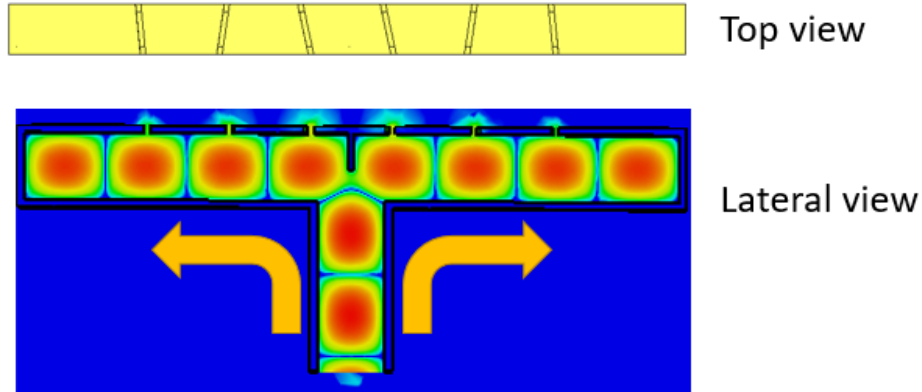


Figure 4.6: T feed wave propagation. When the waveguide encounters the septum, half of the wave goes to the right side and the other half to left side, with Poynting vector going in opposite direction.

branches to generate a constructive main beam. The radiation produced by the portion of the wave that goes to the right-hand side has to be seen with a point symmetry with respect to the left-hand side. As the waves at each slot are already phase-shifted by 180° , the slots on one side have to be arranged with the same angle as the mirrored ones, when seen from outside, as shown in Figure 4.6.

In theory, an array of dipoles will have a SLL of -13 dB [62]. A taper can be applied to have conductances of different amplitudes and then obtaining an even lower SLL. By using six slots, one option was explored to find the optimum sparse positions for the slots based on Rabia Syeda's approach [63]. This approach provided theoretically a SLL of less than -15 dB. An angle $\theta = 15^\circ$, a width of 0.2 mm and the sparse positions were used in the CST model of the six-element slotted-waveguide, but the obtained beam pattern exhibited poor performance. From this experiment, it was concluded that the phase component needs to be included for the optimization algorithm and that the angle of the slots needs to be adjusted accordingly, to obtain a constructive beam pattern. This additional step is proposed as a parallel approach to obtain a taper based on spacing in between the slots.

Another way of creating a taper of amplitudes is by having a fixed $\lambda_g/2$ spacing but with different angles θ for the individual slots. By selecting a Taylor tapering based on six elements, six Taylor coefficients can be obtained to map to six different conductances based on a target SLL [62, 55, 56]. First, the six Taylor coefficients $c_{Taylor-i}$ are calculated. Then the coefficients are translated into corresponding conductances g_i as shown in Equation (4.7) and finally to the required slot angles θ by means of Equation (4.3). After this process, scaling down to match angles around 15° and fine tuning of the angles is done in the 3D model in CST, thus obtaining a symmetric pattern of $\theta = 5.8^\circ, 8.6^\circ, 12.3^\circ, 12.3^\circ, 8.6^\circ, 5.8^\circ$ as it was shown in Figure 4.6 in the top view.

$$g_{eq} = \sum_{i=1}^N g_i = \frac{\sum_{i=1}^N c_{Taylor-i}^2}{\sum_{i=1}^N c_{Taylor-i}}. \quad (4.7)$$

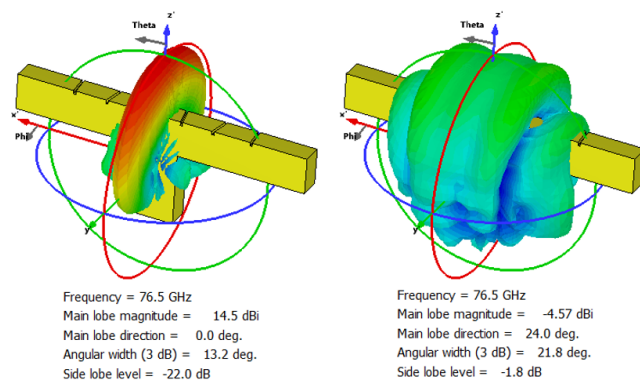


Figure 4.7: Middle feed model. 3D Ludwig 3 copolar (longitudinal) and cross-polar (transverse) component for 76.5 GHz. Directivity is 14.5 dBi and cross-polar level is -19.07 dB with respect to maximum directivity.

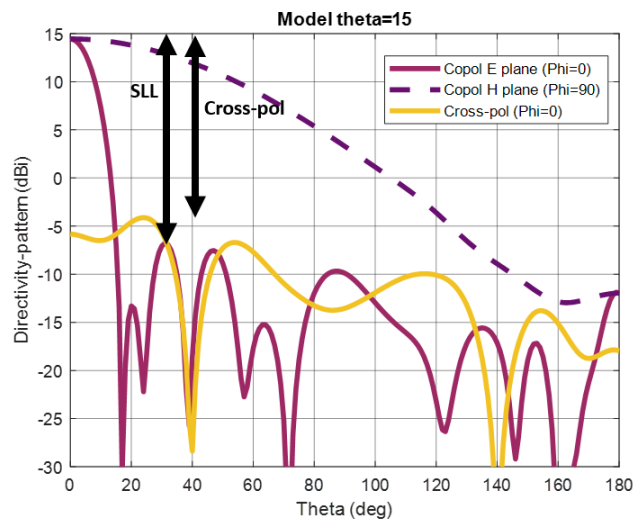


Figure 4.8: Middle feed model. Ludwig 3 copolar (longitudinal) and cross-polar (transverse) component for 76.5 GHz.

Simulation results slot array

The resulting beam pattern at 76.5 GHz for the design with a middle feed is shown in Figure 4.7 and Figure 4.8. For a range of other frequencies, the beam pattern is shown in Appendix C in Figure C.7 and Figure C.8. A summary of the overall performance is shown in Figure 4.9.

At 76.5 GHz, the Ludwig-3 directivity is 14.5 dBi for the longitudinal polarization and -4.57 dBi for the transverse polarization, resulting in a cross-polarization level < -19.07 dB. Also, the SLL is -22.0 dB. The directivity, cross-polar level and SLL are fairly constant over the frequency range from 75-80 GHz. The beam-pattern frequency bandwidth for this model ranges from 75-80 GHz with a decay of less than 10% from the target.

The gain level is extremely low. It is assumed that this is because the model is completely

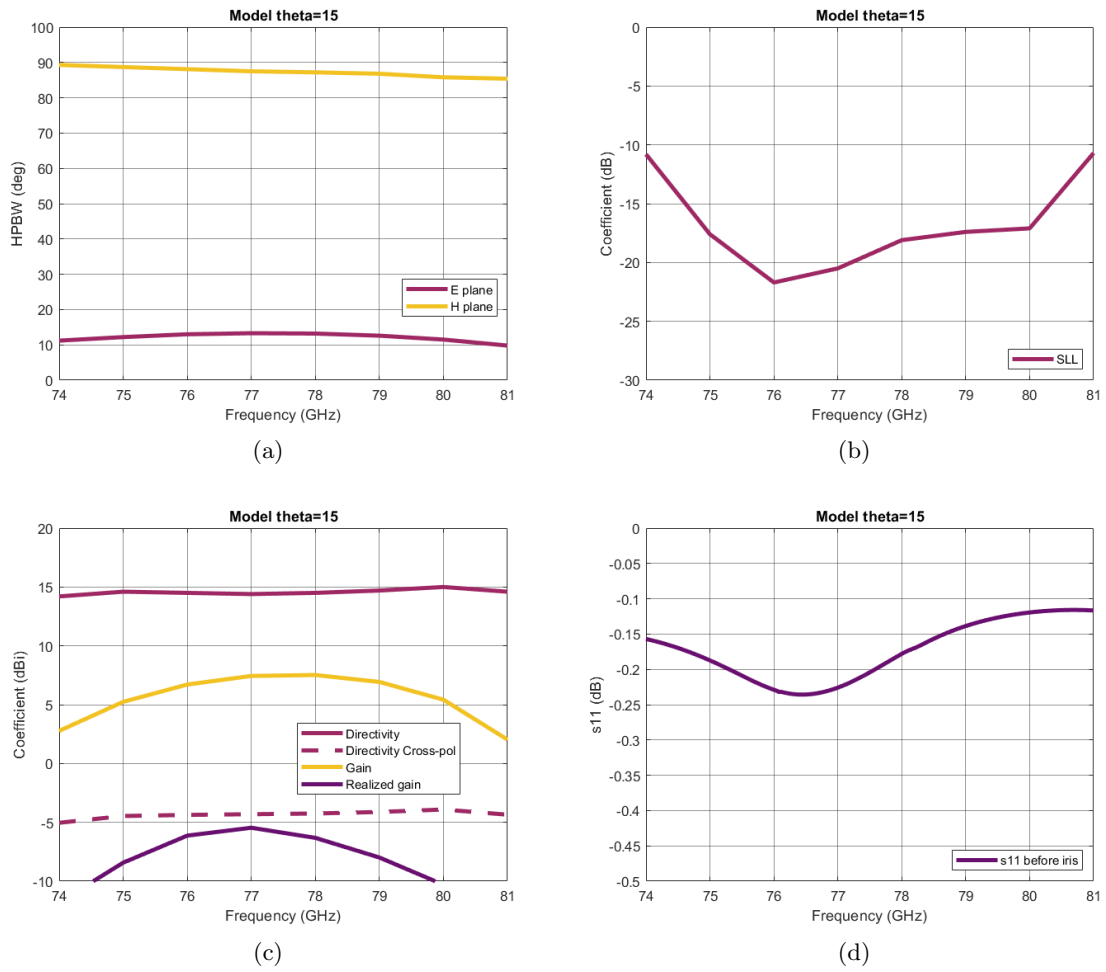


Figure 4.9: Middle feed 15° model simulation results over frequency. (a) is half power beam-width, (b) is SLL, (c) is directivity and gain and (d) is reflection coefficient

not matched and thus the calculation is not accurate. The realized gain is a factor lower than the gain, according to the impedance matching.

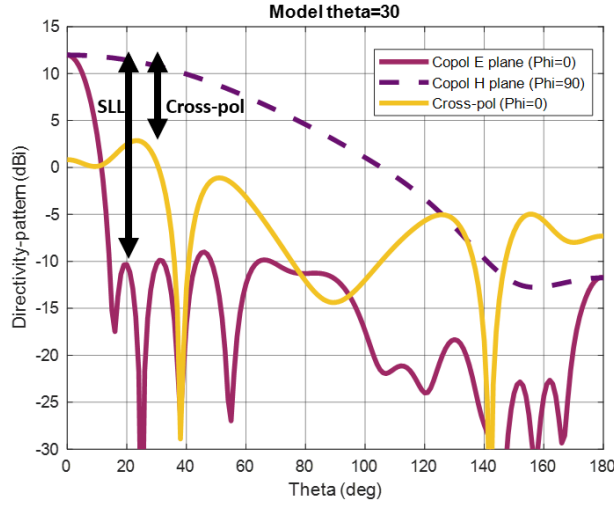


Figure 4.10: Middle feed model. Ludwig 3 copolar (longitudinal) and cross-polar (transverse) component for 76.5 GHz, second iteration using larger angles. Directivity is 11.9 dBi and cross-polar level is -8.65 dB with respect to maximum directivity.

4.3.5 Second alternative for a slot design

As it was explained before, depending on the selection of the angle, the beam-pattern can show a better antenna efficiency or the slotted-waveguide can radiate more. Following all previous steps, a second model is proposed based on angles $\theta \sim 30^\circ$ to provide more radiation at the cost of antenna efficiency. For the design frequency of 76.5 GHz, this angle corresponds to the values of $L_r = 1.8$ mm, $\delta = 0.17$ mm and $L = 1.5$ mm based on Equation (4.2) and $w = 0.2$ mm. The normalized conductance of this slot is 0.5 based on Equation (4.3). The Taylor coefficients provide the slot angles $\theta = 17.4^\circ, 25.8^\circ, 36.9^\circ, 36.9^\circ, 25.8^\circ, 17.4^\circ$. Additionally, the spacing between slots was fine tuned to optimize a constructive beam with low SLL in the center frequency. Results for this design are shown in Figure 4.10 and Figure 4.11.

At 76.5 GHz, the Ludwig-3 directivity is 11.9 dBi for the longitudinal polarization or copolar field component and 3.25 dBi for the transverse polarization or cross-polar field component, resulting in a cross-polarization level < -8.65 dB. Also, the SLL is -21.0 dB. The directivity, gain, cross-polar level and SLL are fairly constant over the frequency range from 75-80 GHz. The beam-pattern frequency bandwidth for this model ranges from 75-80 GHz with a decay of less than 10% from the target.

By comparing Figure 4.9 and Figure 4.11 it can be seen that the directivity, cross-polarization level and SLL are better in the model of smaller angles, in particular the cross-polarization level is considerably lower for the small-angle case. Nevertheless, the realized gain is considerably better for the larger-angle design. This effect is expected because it was known that larger angles radiate more and it was explained that it affects the impedance matching. The starting point for the impedance matching is better in the larger-angle design, as it is shown in Figure 4.12. Because of this, the larger-angle design was selected to continue for the next design steps.

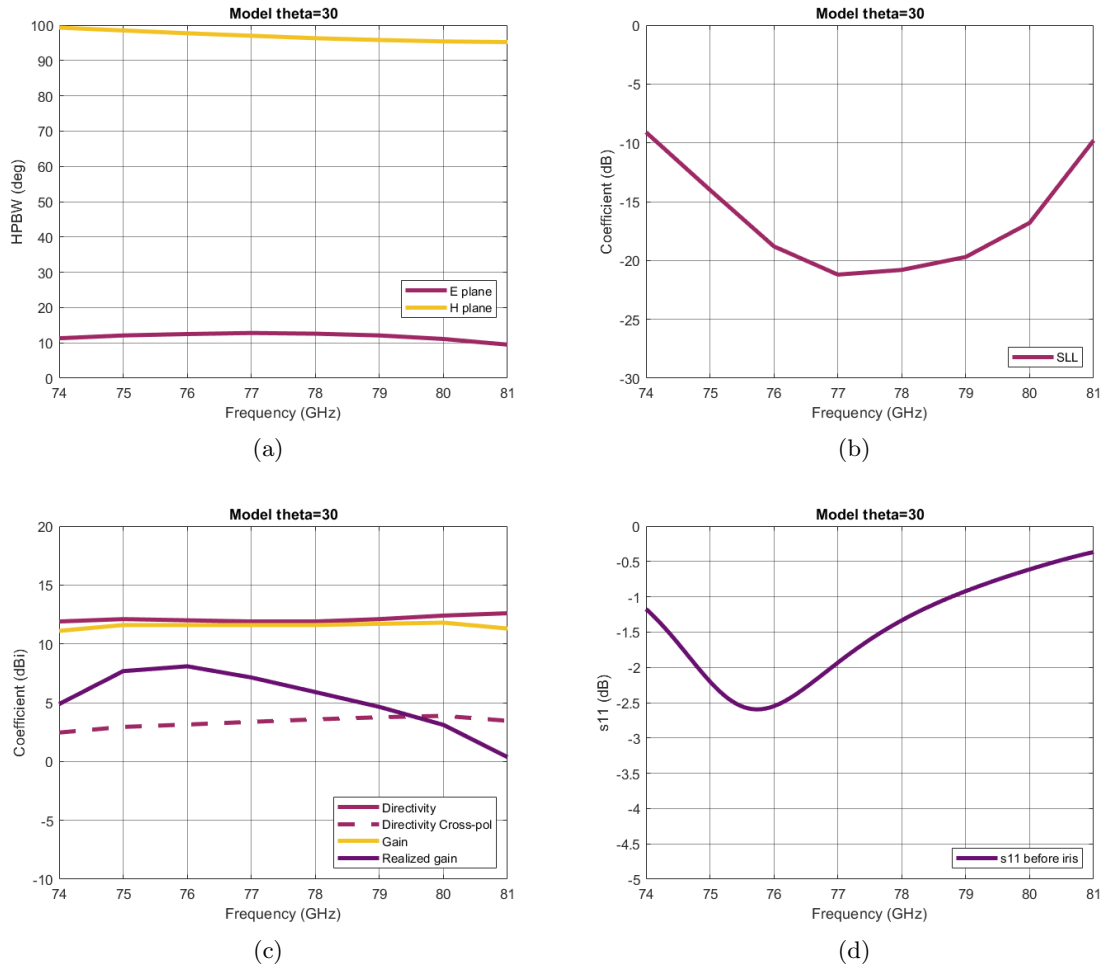


Figure 4.11: Middle feed 30° model simulation results over frequency. (a) is half power beam-width, (b) is SLL, (c) is directivity and gain and (d) is reflection coefficient

4.3.6 Impedance-matching structure

The design of an impedance-matching structure highly depends on the termination of the waveguide. Because of the resonant nature of the design when the waveguide is shorted at the end, the impedance of the slot array shows a strong and frequency-dependent imaginary component, as it was shown in Figure 4.12. To mitigate this effect, a series of inductive and capacitive components can be added to the design as a matching network. An array of inductive irises is selected to compensate the reactive behavior of the slot array [64, 49]. Other approaches, such as a $\lambda/4$ transformer were considered, but due to the large reactive component and small real part, that approach was practically not feasible. The equivalent circuit of this matching network is shown in Figure 4.13.

The focus of this design is for 76-77 GHz, the operation frequency for BSD, but there is also interest in the entire 77-81 GHz band, because it lies inside the frequency band of operation of the radar transceiver. The input impedance is referenced to a different plane, in order to better match the range 76-77 GHz.

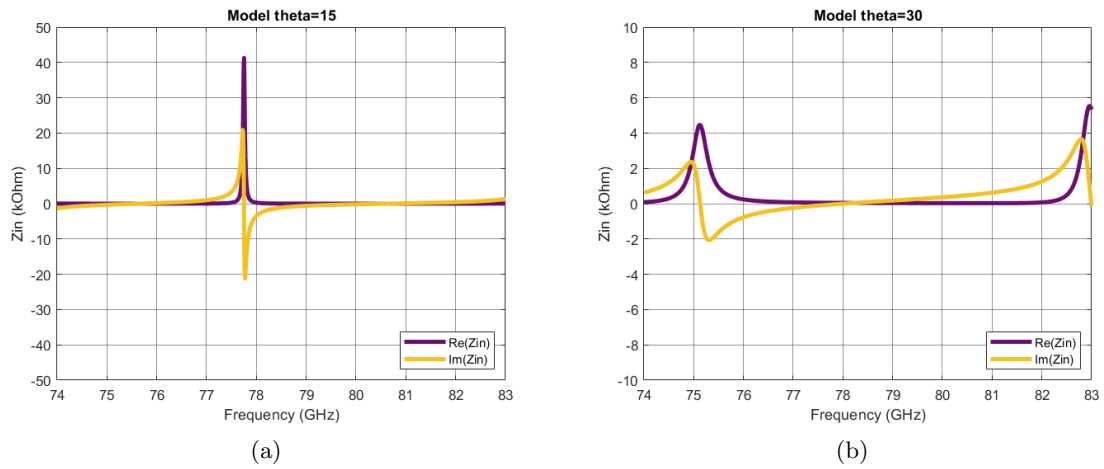


Figure 4.12: Input impedance of the shorted center-feed slotted waveguide antenna. (a) 15° model. The real and imaginary components show a strong variation in a narrow frequency range, making it difficult to match. (b) 30° model. The real and imaginary components show less variation over frequency, making it easier to match.

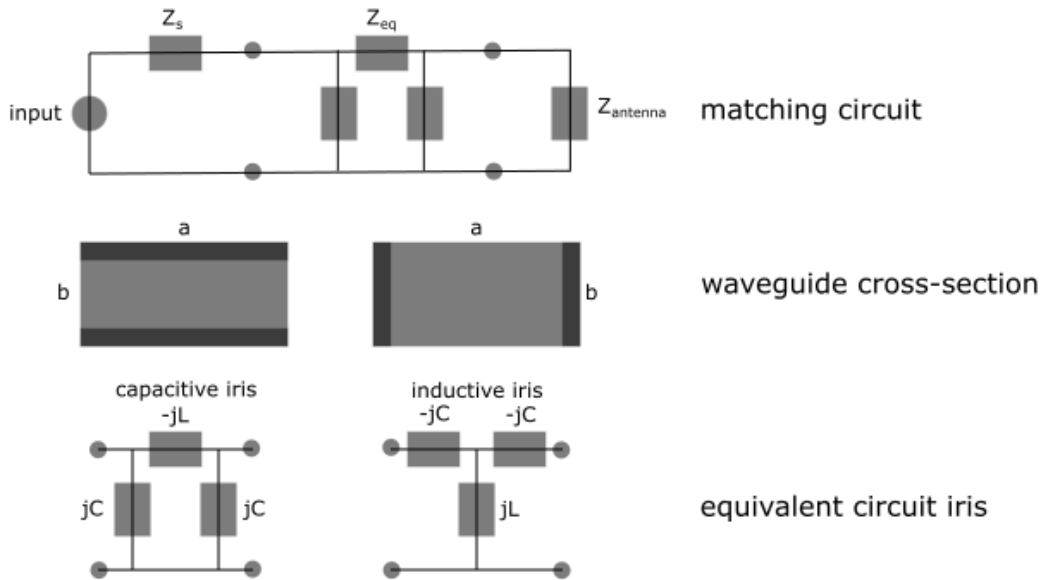


Figure 4.13: Impedance-matching network formed by capacitive or inductive irises. Capacitive irises are created when they are placed in the broad side of the waveguide a and inductive irises are created when placed in the narrow side b . Image adapted from [64].

Simulation results including matching network

By adding an inductive iris, a reflection coefficient lower than -10 dB can be obtained, but only for a narrow impedance-matching frequency bandwidth of 300 MHz, as shown in Figure 4.14. Figure 4.14 also shows that the performance parameters remain similar as for the design

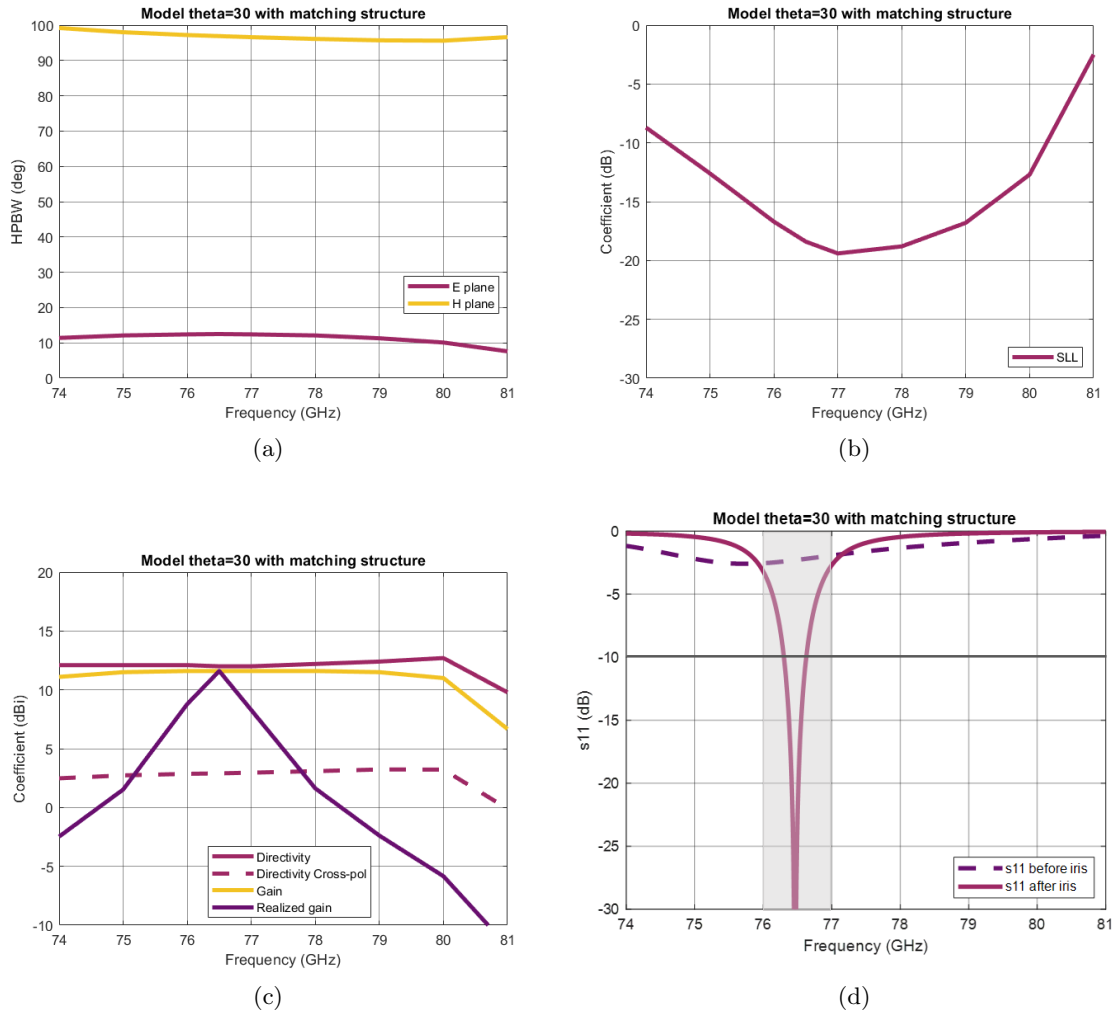


Figure 4.14: Middle feed 30° model, with matching structure, simulation results over frequency. (a) is half power beam-width, (b) is SLL, (c) is directivity and gain and (d) is reflection coefficient

without iris, but the realized gain is greatly improved for the design frequency. Nevertheless, the addition of irises will make the model more complex and expensive to fabricate, but this addition is needed to achieve the impedance matching. Also, when the antennas are fabricated in mass-production, the use of a mold will lower the cost of the addition of irises, making it comparable as a model without irises. In order to further improving the impedance-matching frequency bandwidth it is possible to add more irises in cascade at an additional cost.

4.3.7 Beamforming network and integration of the design

Because of the fixed disposition of the phase center of the seven slotted-waveguide antennas for the three Tx and four Rx, and the required spacing between them, as already mentioned in Chapter 2, a ridge to reduce the size of the waveguide is needed in the case of a waveguide antenna with slots cut in the broad wall, when targeting half-wavelength spacing between

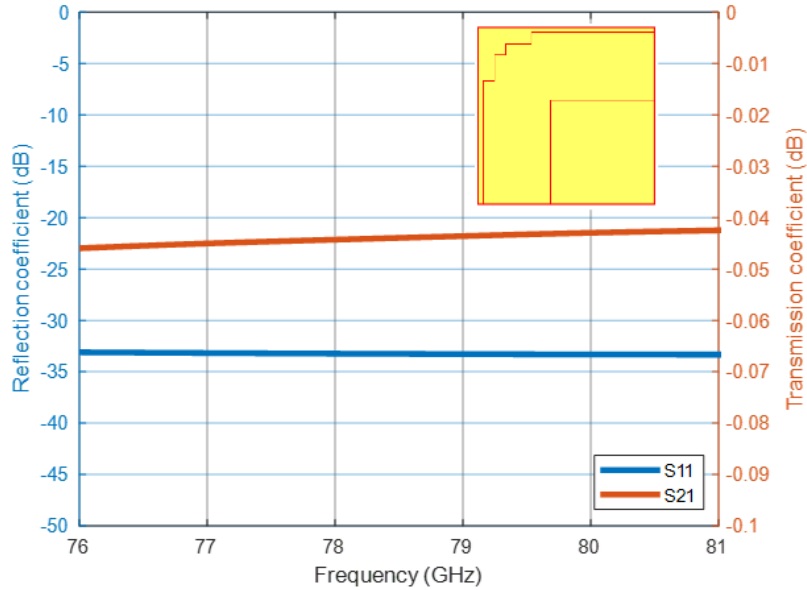


Figure 4.15: 90° H bend reflection and transmission coefficient. The steps have been optimized to have minimum reflection and maximum transmission from one side to the other.

two adjacent waveguides [65, 66]. However, this is not the case for slots cut in the narrow wall. The width of the slotted-waveguide narrow wall is 1.27 mm, which allows to fit two waveguides at half-wavelength spacing, as shown in Chapter 2 in Figure 2.3.

The required beamforming network then consists of waveguide bends optimized for low losses, interconnected with regular rectangular waveguides. The design of the waveguide bend consists of optimized steps that lead to a reflection lower than -30 dB and transmission loss lower than 0.05 dB, as shown in Figure 4.15. The complete beamforming network is shown in Figure 4.16.

All three Tx and four Rx channels are positioned according to the requirements specified by the software team. The beamforming network is connected to all respective middle feeds, which include the impedance-matching network. A metal plane is added to isolate the radiating plane from all the electronics that would be placed below the antenna array.

The optimized position of the ground plane was found to be at the middle of the waveguide broad wall or at one wavelength from the antenna aperture. The metal plane does not greatly affect the performance of the slotted-waveguide antenna. The coupling between the different slotted-waveguide arrays does not greatly influence the beam pattern performance when studied one by one in active-passive mode. The final design is shown in Figure 4.17.

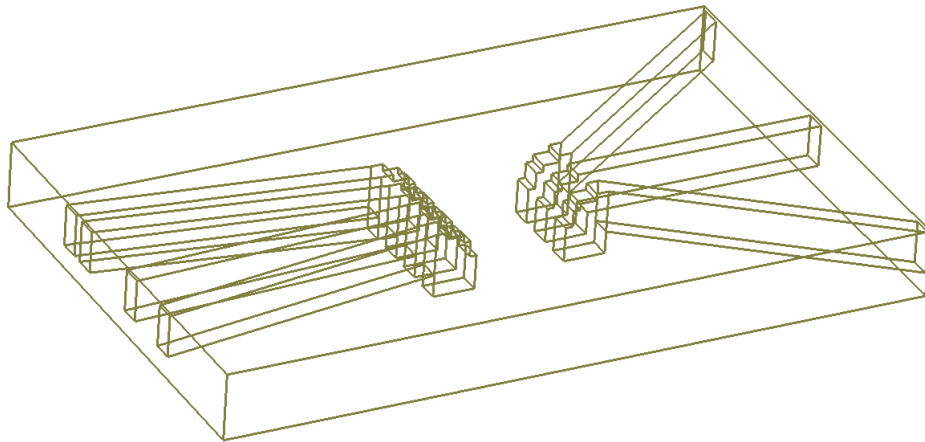


Figure 4.16: Beamforming network for a seven-channel slotted-waveguide antenna array. Both the position of the starting waveguide openings and the phase center of each of the antennas is fixed. The beamforming network consists of rectangular standard WR-10 waveguides connected through H-bends. An additional bend on each channel can be added to feed from the center of the waveguide.

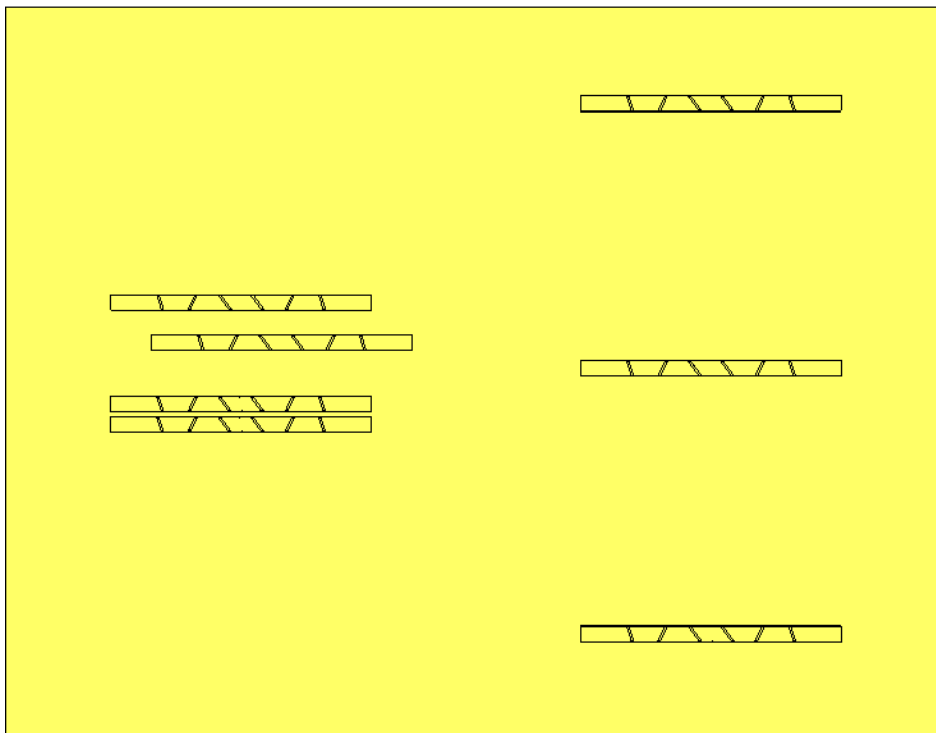


Figure 4.17: Seven-channel antenna array. Three Tx and four Rx antennas are placed at their intended positions. A metal plane shields the design to the electronics that will be placed below it.

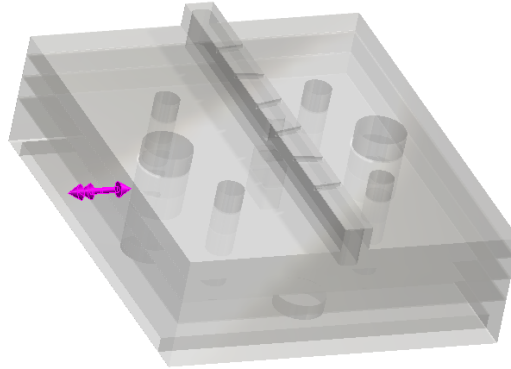


Figure 4.18: Single-channel antenna model to be fabricated in metal layers. It includes a standard WR-10 UG-387/U flange.

4.4 Slotted-waveguide antenna fabrication

The model presented in the preceding section in Figure 4.17 can be built into a brass block by splitting it into several layers and by using the milling technique available at EPC. This approach is the same as used for the waveguide fan-out presented in Chapter 3. A lapping procedure would not be needed in this case because the surfaces are much smaller and thus a good contact in between surfaces is achieved by only using screws and alignment pins.

Due to time and budget constraints, it was decided to fabricate the model of a single six-element slotted-waveguide antenna together with its matching network, instead of the full TxRx seven-element array. The model to be fabricated is shown in Figure 4.18 and it includes a standard WR-10 UG-387/U flange to be connected to a standard waveguide connector. Results of simulations for this model, including a metal plane of finite size, can be found in Appendix in Figure C.9

4.5 Slotted-waveguide antenna characterization

To characterize the slotted-waveguide antenna, two measurement set-ups are needed. First, a beam scanner to obtain the beam pattern properties such as gain, SLL for co-polarization and cross-polarization components in the frequency range of interest, at least from 76-77 GHz, but preferably from 75-82 GHz. Second, a VNA to characterize the reflection loss in the frequency range from 74-83 GHz. The first set-up is available at TU/e and the second at NXP, in both cases a WR10-WR12 waveguide transition is needed because both laboratories have their set-up based on WR-12 waveguide connectors.

4.6 Comparison of longitudinally and transversely polarized slotted-waveguide antenna

Transversely-polarized antennas have already been used for automotive applications and a longitudinally-polarized slotted-waveguide antenna is less studied for this particular applica-

tion. The theory to model the conductance of the slots cut in the broad wall is analytic and then the equations to find the conductance of the slot are more accurate than the case for the longitudinally-polarized slot. For the longitudinally polarized antenna, there are approximate models that are much more complex and can only be resolved numerically. This difference gives rise to the tendency to prefer the transversely polarized concept over the longitudinally polarized one, but for some applications one polarization might be more convenient than the other or it might even be needed to have a dual polarization system.

Additionally, the main design parameter of the longitudinally polarized slot antenna is the angle of the slot, while for the transversely polarized antenna it is the offset from the center of the broad wall of the waveguide. The challenge for longitudinally polarized antennas is that small angles lead to less radiation, meaning there is more storage of energy and this results in an input impedance that is difficult to match, and yields a narrow-band behavior. Larger angles lead to more radiation and have less constraints at the moment of creating a matching network, but the antenna efficiency is maximized for conductances lower than 0.1[54, 40], which maps to angles lower than 15° . This trade-off does not exist in the case of transversely polarized antennas. Examples have been found of longitudinally polarized slotted-waveguide antennas that show a good matching, but always with a narrowband behavior. Examples of large arrays can be found in [67, 68] and small arrays can be found in [69].

The big advantage of longitudinally polarized slotted-waveguide antennas is that the radiating plane is at the narrow wall. This means there is more flexibility in placing multiple slot arrays as close as $\lambda_0/2$, without the need for additional structures such as a ridged waveguide. Overall, there are less references for longitudinally polarized slotted-waveguide antenna for the required application and there are also more constraints when selecting the angles for the slots.

4.7 Conclusions

The design of a longitudinally polarized slotted-waveguide antenna has been discussed. Design choices exist for the feeding strategy, the termination of the waveguide, the selected angles of the slots and the way to arrange an array of slots. All design choices provide a good performance in some aspects, but there is not a combination that can cover all requirements at once. Small slot angles produce a good and constant performance over the desired frequency band in terms of directivity, cross-polarization and side lobe level. Nevertheless, the impedance bandwidth is only possible for a very small frequency range. The design for larger slot angles provided a pattern with higher cross-polarization level, less directivity and a side lobe level that decays faster over frequency. But the realized gain and the impedance matching are considerably better than the small-angle case.

For other applications, where the space occupied by the antenna is not an important constraint, a larger slot array containing at least 20 elements is a good option to mitigate the large impedance and its variation over frequency associated with the storage of energy inside the waveguide and at the same time achieve a good antenna efficiency. For a restricted space and based on the requirements for the BSD module, a transversely polarized slotted-waveguide antenna provides a better compromise in terms of performance, although at a higher manufacturing cost.

Chapter 5

Conclusions and future work

5.1 Conclusions

The motivation behind self-driving cars, a brief overview of the principle of operation of radars, types of radars, and the state of the art of commercial MIMO radar solutions were reviewed. After this, the conclusion was that there is still a long way towards having a fully automated level-5 car. The major obstacles for the moment are to have a solid legislation around it and the acceptance at the society level. Spite of this being the major constraint, there are also technology improvements to be done. We have focused on the improvement of the sensor, specifically a radar sensor. It was found that to make radars a competitive solution, the losses and isolation have to be improved, specially for the case when several antennas are used.

In addition to the requirement of having a radar sensor with low losses and high isolation in between different channels, there were other requirements. The starting point for this design was an updated version of the 3Tx4Rx Dolphin transceiver chip from NXP. It operates in the current car radar frequency band of 76-81 GHz. So the frequency of operation was already fixed. Also, the decision was to opt for waveguide-like transitions and antennas, for the reason they can provide good performance at a relatively low cost, compared with PCB transitions and antennas as the commonly used solution. Finally, it was decided to use BSD as use case. The software team from NXP proposed positions for the phase center of the antennas to scan in 2D for a BSD use case. All design choices also had to provide low-cost solutions to make the radar module profitable.

The proposed solution consisted then on vertically mounting a waveguide interface from IC to waveguide antenna array. The first step towards the proposed solution was to finalize the design and characterization of a waveguide launcher in package. Re-optimization according to updated design rules and the addition of a higher-frequency design of the launcher was conducted. The characterization of the different versions of the LiP in combination with different types of interface layers in between the launcher and a standard waveguide was also part of the conducted tasks. It was found after measurements in the laboratory that the fabricated models were in agreement with the simulations. Even though the results show reflections less than -10 dB and transmission loss lower than 2.5 dB, there is still room for improvement to get to reflections less than -15 dB and losses of around 1 dB. This is because a major constraint was the design rules of the technology used, which was updated just before the deadline to fabricate the launcher demonstrator. Isolation was in all cases less than -30 dB.

Regarding the different interfaces, they showed different mechanical properties and some were certainly more reliable than others. Preferred materials are silicone based. They are less sensitive to applied pressure and they keep their shape even after several cycles of mounting and dismounting. All the selected dielectric materials showed a behavior consistent with a material with high loss tangent of around 0.05. Thus, if a less lossy material is used, even with loss tangent of 0.01, 1 dB of losses can be recovered. Overall, the concept of the launcher in package was proven.

For the antenna design it was opted to use a longitudinally-polarized slotted-waveguide antenna. The feeding strategy, the type of wave that exists inside the waveguide, the selected angle of tilting of the slot and the slot-array disposition were the main design choices. It was chosen to use a central feed to increase the frequency bandwidth at the cost of a more complex beamforming network structure. A standing wave was produced after having shorted ends in the waveguide, this was at the cost of a more complex matching strategy but winning radiating power, which was the main goal of the design. The choice of the angle of tilting of the slot was a difficult decision because there is a trade-off in between the radiation efficiency and the radiating power. Small angles, in particular if they are $\sim 15^\circ$ provide better beam pattern properties, but larger angles, for example $\sim 30^\circ$ provide a slot with higher excitation and thus the radiating power is more per slot. Because the array of slots was restricted to a small number, this effect had a big impact in the matching because it resulted in a cavity less resonant just by changing the angle of the slot. For the disposition of the six slot array it was decided to use a Taylor tapering of amplitudes based on different tilting angles and a fixed separation in between them.

The resulting antenna showed to be narrow-band because of the issue previously mentioned. A $\sim 15^\circ$ tapered based array had a good performance in terms of the beam pattern. The obtained directivity was 14.5 dBi, SLL was -22 dB, cross-polarization level was lower than -19 dB and fairly constant over the frequency range of 76-81 GHz. Nevertheless the starting point of reflection coefficient was challenging. For the model of $\sim 30^\circ$ the impedance matching bandwidth was ~ 300 MHz after adding a single iris. This case provides a worse cross-polarization level in the order of -10 dB. The slotted-waveguide antenna cut in the broad wall, which is transversely polarized, seems to be a better option for a small array due to the trade-off existing in the longitudinally-polarized case.

5.2 Future work

The measurements of the longitudinally-polarized antenna are pending as the device is currently to be ordered to the mechanical workshop at TU/e. Additional long term tasks are to integrate the complete module, including the IC with LiP in the respective application board and an array of seven antennas, one for each of the seven channels of the radar transceiver. Then, apart from the operation as a full radar module with 2D scan capabilities, the antenna array can be tested standalone to characterize the beam pattern, the interaction in between antennas and the reflection and isolation coefficients.

A step even further is to use several ICs connected in cascaded operation to be able to integrate a large array of antennas. In this case, by using MIMO array capabilities, sparse positions could be used to obtain a large aperture maximizing the use of power. All of this can only be a real advantage if each of the cells IC+interface+antenna are optimized to provide very low losses, which is why the tasks conducted in this project were relevant to move to

imaging radars.

Bibliography

- [1] PwC. (2020) Five trends transforming the automotive industry. [Online]. Available: <https://www.pwc.nl/en/publicaties/five-trends-transforming-the-automotive-industry.html> 1
- [2] Julia Pyper, Scientific American Magazine. (2020) Self-Driving Cars Could Cut Greenhouse Gas Pollution. [Online]. Available: <https://www.scientificamerican.com/article/self-driving-cars-could-cut-greenhouse-gas-pollution/> 1
- [3] A. Maxmen, “A moral map for ai cars,” *Nature*, vol. 562, pp. 469–470, 10 2018. 1
- [4] T. Pollard, Car Magazine. (2019) What are autonomous car levels? Levels 1 to 5 of driverless vehicle tech explained. [Online]. Available: <https://www.carmagazine.co.uk/car-news/tech/autonomous-car-levels-different-driverless-technology-levels-explained/> 1, 10
- [5] Euro NCAP. (2020) NCAP web page. [Online]. Available: <https://www.euroncap.com/> 2
- [6] Waymo. (2020) Google self-driving car project: Waymo. [Online]. Available: <https://waymo.com/> 2
- [7] Tesla. (2020) Tesla autopilot system. [Online]. Available: <https://www.tesla.com/autopilot> 2
- [8] Nuro. (2020) Nuro: self-driving vehicle for goods transportation. [Online]. Available: <https://nuro.ai/product> 2
- [9] Uber. (2020) Uber. [Online]. Available: <https://www.uber.com/us/en/atg/technology/> 2
- [10] SAE International. (2019) Society of Automotive Engineers International levels of driving automation j3016. [Online]. Available: <https://www.sae.org/news/2019/01/sae-updates-j3016-automated-driving-graphic> 2
- [11] R. Rasshofer and G. K, “Automotive radar and lidar systems for next generation driver assistance functions,” *Advances in Radio Science - Kleinheubacher Berichte*, vol. 3, 05 2005. 7
- [12] T. K. Sarkar and M. Salazar Palma, “A history of the evolution of RADAR,” *European Microwave Week 2014: Connecting the Future, EuMW 2014 - Conference Proceedings; EuMC 2014: 44th European Microwave Conference*, no. June 1904, pp. 734–737, 2014. 3

- [13] ETSI Europe. (2020) European Telecommunications Standards Institute (ETSI). [Online]. Available: <https://www.etsi.org/> 3
- [14] FCC USA. (2020) Federal Communications Commission (FCC). [Online]. Available: <https://www.fcc.gov/> 3
- [15] B. Sene, D. Reiter, H. Knapp, H. Li, T. Braun, and N. Pohl, “An automotive μ -band fmcw radar sensor based on a sige-transceiver mmic,” *IEEE Microwave and Wireless Components Letters*, vol. 32, no. 3, pp. 194–197, 2022. 3
- [16] K. Lomakin, M. Sippel, K. Helmreich, and G. Gold, “3d printed slotted waveguide array antenna for d-band applications,” in *2021 15th European Conference on Antennas and Propagation (EuCAP)*, 2021, pp. 1–4. 3
- [17] M. I. Skolnik, *Introduction to Radar Systems, 2nd Edition*, 2nd ed. New York: McGraw Hill Book Co., 1980. 3, 4
- [18] H. Griffiths, “Multistatic, mimo and networked radar: The future of radar sensors?” in *The 7th European Radar Conference*, 2010, pp. 81–84. 5
- [19] C. A. Balanis, *Modern antenna handbook*. Hoboken, New Jersey: John Wiley and Sons, Inc, 2008. 5
- [20] A. B. Smolders, H. Visser, and U. Johannsen, *Modern Antennas and Microwave Circuits*. Eindhoven: Eindhoven University of Technology, 2020. 5
- [21] E. Brookner, “Mimo radar demystified and where it makes sense to use,” in *2014 IEEE Radar Conference*, 2014, pp. 0411–0416. 5
- [22] NXP Semiconductors. (2020) NXP Semiconductors radar system solutions. [Online]. Available: <https://www.nxp.com/applications/solutions/automotive/adas-and-highly-automated-driving/automotive-radar-systems:RADAR-SYSTEMS> 8, 59
- [23] Infineon. (2020) Infineon company presentation june 2020. [Online]. Available: https://www.infineon.com/dgdl/IFX_FY2020_Q2_Web_EN.pdf?fileId=5546d4615f9640f0015fb9c63a36005b 8, 60
- [24] Texas Instruments. (2020) TI at a glance. [Online]. Available: <https://www.ti.com/about-ti/company/ti-at-a-glance.html> 8, 60
- [25] ——. (2020) TI Advanced Driver Assistance Systems. [Online]. Available: <https://www.ti.com/applications/automotive/adas/overview.html> 8, 60
- [26] STMicroelectronics. (2020) STMicroelectronics 77 GHz radar. [Online]. Available: <https://www.st.com/en/applications/adas/77-ghz-radar.html> 8, 60
- [27] UMS. (2020) UMS products. [Online]. Available: <https://www.ums-gaas.com/products/> 8, 61
- [28] ArbeRobotics. (2020) Arbe Phoenix. [Online]. Available: <https://arberobotics.com/product/> 9, 61

- [29] Cognitive Pilot. (2020) Cognitive Pilot Imaging 4D radar solution. [Online]. Available: <https://en.cognitivepilot.com/products/radar-sensor/> 9, 62
- [30] Vayyar. (2020) Vayyar Automotive Radar. [Online]. Available: <https://vayyar.com/auto> 9, 62
- [31] Smartmicro. (2020) Smartmicro Automotive Radar. [Online]. Available: <https://www.smartmicro.com/automotive-radar/> 9, 62
- [32] InnoSenT. (2020) InnoSenT Automotive Radar. [Online]. Available: <https://www.innosent.de/en/automotive/> 10
- [33] NXP Semiconductor. (2020) TEF810X Block Diagram. [Online]. Available: <https://www.nxp.com/products/rf/radar-transceivers/tef810x-fully-integrated-77-ghz-radar-transceiver:TEF810X> 14, 15
- [34] V. Tapia, “Waveguide launcher in package solution for car radar applications,” Eindhoven, unpublished PDEng Thesis, Eindhoven University of Technology, Eindhoven, 2020. 14, 16, 18, 19, 22
- [35] S. Jameson and E. Socher, “A wide-band cmos to waveguide transition at mm-wave frequencies with wire-bonds,” *IEEE Transactions on Microwave Theory and Techniques*, vol. 63, no. 9, pp. 2741–2750, 2015. 18
- [36] Y. Li, B. Pan, M. M. Tentzeris, and J. Papapolymerou, “A fully micromachined w-band coplanar waveguide to rectangular waveguide transition,” in *2007 IEEE/MTT-S International Microwave Symposium*, 2007, pp. 1031–1034. 18
- [37] U. Johannsen, “Technologies for integrated millimeter-wave antennas,” Ph.D. dissertation, Eindhoven University of Technology, Eindhoven, 2013. 18
- [38] S. Geluk, “Low-Loss mm-Wave Transitions between Integrated Circuits and Antennas,” Ph.D. dissertation, Eindhoven University of Technology, Eindhoven, 2019. 18
- [39] Dassault Systemes. (2020) CST Studio Suite Software . [Online]. Available: <https://www.3ds.com/es/productos-y-servicios/simulia/productos/cst-studio-suite/> 21
- [40] W. Watson, “Resonant slots,” *Radio Section paper, based on reports to the National Research Council of Canada.*, pp. 747–777, 1946. 32, 33, 35, 38, 49
- [41] A. F. Stevenson, “Theory of slots in rectangular wave-guides,” *Journal of Applied Physics*, vol. 19, no. 1, pp. 24–38, 1948. [Online]. Available: <https://doi.org/10.1063/1.1697868> 32, 35
- [42] B. Das, J. Ramakrishna, and B. Sarap, “Resonant conductance of inclined slots in the narrow wall of a rectangular waveguide,” *IEEE Transactions on Antennas and Propagation*, vol. 32, no. 7, pp. 759–761, 1984. 32, 34, 35, 70, 71
- [43] P. Hsu and S. Chen, “Admittance and resonant length of inclined slots in the narrow wall of a rectangular waveguide,” *IEEE Transactions on Antennas and Propagation*, vol. 37, no. 1, pp. 45–49, 1989. 32, 35

- [44] A. Oliner, “The impedance properties of narrow radiating slots in the broad face of rectangular waveguide: Part i—theory,” *IRE Transactions on Antennas and Propagation*, vol. 5, no. 1, pp. 4–11, 1957. 32
- [45] H. Saltzman and G. Stavis, “A dual beam planar antenna for janus type doppler navigation systems,” in *1958 IRE International Convention Record*, vol. 6, 1958, pp. 240–247. 32
- [46] I. F. da Costa, D. H. Spadoti, and S. A. Cerqueira, “Dual-band slotted waveguide antenna array for communication, maritime navigation and surveillance radar,” in *2015 International Workshop on Telecommunications (IWT)*, 2015, pp. 1–4. 32
- [47] R. C. J. H. Jasik, *Antenna Engineering Handbook*, 2nd ed. New York: McGraw-Hill, 1984. 32
- [48] J. L. Volakis, *Antenna Engineering Handbook. Chapter 9: Waveguide Slot Antenna Arrays by R.A. Gilbert*, 4th ed. New York: McGraw-Hill, 2007. 33, 35
- [49] D. M. Pozar, *Microwave Engineering*, 4th ed. Hoboken, New Jersey: John Wiley and Sons, Inc, 2012. 33, 43
- [50] K.-R. Chou, H.-N. Lin, W. Lu, H.-W. Chang, and K. Tiong, “Design and operation of an edge-wall slotted waveguide array antenna with ultralow side lobes for application of off-shore radar,” *Journal of Marine Science and Technology*, vol. 23, pp. 620–627, 10 2015. 33, 38
- [51] R. Elliott and L. Kurtz, “The design of small slot arrays,” *IEEE Transactions on Antennas and Propagation*, vol. 26, no. 2, pp. 214–219, 1978. 33
- [52] R. Elliott and W. O’Loughlin, “The design of slot arrays including internal mutual coupling,” in *1986 Antennas and Propagation Society International Symposium*, vol. 24, 1986, pp. 319–322. 33
- [53] J. Hilburn, R. Kinney, R. Emmett, and F. Prestwood, “Frequency-scanned x-band waveguide array,” *IEEE Transactions on Antennas and Propagation*, vol. 20, no. 4, pp. 506–509, 1972. 33, 34, 35, 36, 75
- [54] J. Hilburn and F. Prestwood, “K band frequency-scanned waveguide array,” *IEEE Transactions on Antennas and Propagation*, vol. 22, no. 2, pp. 340–342, 1974. 33, 34, 38, 49
- [55] G. Raffoul and J. Hilburn, “Radiation efficiency of an x band waveguide array,” *IEEE Transactions on Antennas and Propagation*, vol. 22, no. 2, pp. 355–357, 1974. 33, 34, 38, 39
- [56] H. M. El Misilmani, M. Al-Husseini, K. Y. Kabalan, and A. El-Hajj, “A design procedure for slotted waveguide antennas with specified sidelobe levels,” in *2014 International Conference on High Performance Computing Simulation (HPCS)*, 2014, pp. 828–832. 34, 39
- [57] L. Oliveira, A. Alves S., and H. Hernandez-Figueroa, “A novel vertically polarized slotted waveguide array antenna,” in *The Second European Conference on Antennas and Propagation, EuCAP 2007*, 2007, pp. 1–5. 34

- [58] D. Dogan and A. Civi, "Edge wall slotted waveguide antenna with low cross polarization," in *2010 IEEE Antennas and Propagation Society International Symposium*, 2010, pp. 1–4. 34
- [59] D. Gray, K. Sakakibara, and Y. Zhu, "Narrow-wall confined slotted waveguide structural antennas for small multi-rotor uav," in *2013 Proceedings of the International Symposium on Antennas Propagation*, vol. 02, 2013, pp. 1192–1195. 34
- [60] L. Zhang and T. Liu, "A new h-plane t-junction waveguide power divider covering the full w-band," in *2020 IEEE 3rd International Conference on Electronic Information and Communication Technology (ICEICT)*, 2020, pp. 803–805. 36
- [61] Y. Miura, J. Hirokawa, M. Ando, Y. Shibuya, and G. Yoshida, "Double-layer full-corporate-feed hollow-waveguide slot array antenna in the 60-ghz band," *IEEE Transactions on Antennas and Propagation*, vol. 59, no. 8, pp. 2844–2851, 2011. 36
- [62] C. A. Balanis, *Antenna theory: analysis and design*, 4th ed. Hoboken, New Jersey: John Wiley and Sons, Inc, 2016. 39
- [63] R. Z. Syeda, "Millimeter-wave MIMO radars for radio-frequency imaging systems. A sparse array topology approach," Ph.D. dissertation, Eindhoven University of Technology, Eindhoven, 2021. 39
- [64] N. Marcuvitz, *Waveguide Handbook*, 2nd ed. London: IET, 1986. 43, 44
- [65] D. Kim and R. Elliott, "A design procedure for slot arrays fed by single-ridge waveguide," *IEEE Transactions on Antennas and Propagation*, vol. 36, no. 11, pp. 1531–1536, 1988. 46
- [66] K. Tekkouk, J. Hirokawa, R. Sauleau, M. Ettorre, M. Sano, and M. Ando, "Dual-layer ridged waveguide slot array fed by a butler matrix with sidelobe control in the 60-ghz band," *IEEE Transactions on Antennas and Propagation*, vol. 63, no. 9, pp. 3857–3867, 2015. 46
- [67] M. A. K. S. Lubis, D. P. Yusuf, F. Y. Zulkifli, and E. T. Rahardjo, "Bandwidth improvement with narrow wall slotted waveguide antenna," in *2017 International Conference on Radar, Antenna, Microwave, Electronics, and Telecommunications (ICRAMET)*, 2017, pp. 93–95. 49
- [68] D. P. Yusuf, F. Y. Zulkifli, and E. T. Rahardjo, "Design of narrow-wall slotted waveguide antenna with v-shaped metal reflector for xband radar application," in *2018 International Symposium on Antennas and Propagation (ISAP)*, 2018, pp. 1–2. 49
- [69] A. Schultz and X. Wu, "A novel low loss e-plane substrate integrated waveguide narrow wall slot antenna," in *2020 IEEE International Symposium on Antennas and Propagation and North American Radio Science Meeting*, 2020, pp. 83–84. 49
- [70] Infineon. (2020) Infineon radar sensors for automotive industry. [Online]. Available: <https://www.infineon.com/cms/en/product/sensor/radar-image-sensors/radar-sensors/radar-sensors-for-automotive/#!products> 60

Acknowledgements or the story of how I arrived to this point

It all started with the interview for this position while I was in the middle of the Pacific Ocean with bad internet connection. But it went well and I moved to Europe expecting to travel more than any other time in my life... and it ended up being quite the opposite. Soon after my arrival to The Netherlands covid arrived too and all expectations changed. I am starting with this because that was the most challenging part of this journey and at the same time the reason why I am so grateful of the people around me.

First of all, to my supervising team, thank you for being there, pushing me but being comprehensive and human. I appreciate the dedication and efforts you made to keep the communication going on spite of all difficulties. It was very challenging to conduct a project being isolated and our regular meetings were vital to keep me going: thank you Bart, Martijn, Rabia and Anton, Giorgio and Waqas. Thank you also to the members of the review committee for your valuable feedback and support during this project.

To all the DEES coaches and colleagues, I wish we would have had more opportunities to meet in person. I always felt very welcomed in DEES family and for that I should give special thanks to Rian. I was not able to meet many people before we went into lockdown, and you managed to create a sense of community for all of us in DEES program. We were virtually accompanied and taken care of.

Then to Vincent, Fernando, Dixit and Cesar, because it all changed after meeting you. I am grateful not only for our great meals together, each one better than the previous one, but mainly the company and support you mean to me. Also to Katerina, Asterios, Stijn, Lorenzo, Chetna and Shobhit, I am so happy our paths crossed and I hope they will keep on crossing spite of our new jobs or new home-cities. Thanks to Rabia again because you doubled as supervisor and friend (and now tripled as a colleague too in which you have also helped me). To all my friends in Chile and the ones who are also abroad, thank you for being in my most appreciated memories and for being close spite of being far away. To Corina, Cristian and Valentino: I am so happy we can continue our adventures now a bit closer.

And to my family, all of them: I like to think that I am a lucky person. Most of my luck is because of having you. Thank you for letting me be whatever I wanted, for loving me and letting me love you, thank you for being so special... The worst side of The Netherlands is that you are not here (not so much the fact of the bad weather). I miss you a lot.

The reason I am here is because of all of you. Infinite thanks to all.

Appendix A

State of the art of commercial automotive MIMO radars

The automotive industry has included radars to implement different ADAS and NCAP functionalities. Bosch (Germany), Continental (Germany), Autoliv (Sweden), Hella (Germany), Denso (Japan), Delphi (UK) and Valeo (France), in partnership with semiconductor suppliers, have developed radar modules for car manufacturers. A review of the automotive vendors of these commercial solutions is given and the characteristics of the systems are presented, with a focus on FMCW MIMO radars in the 77 GHz band.

A.1 Transceiver suppliers (77 GHz band)

There are several companies that supply semiconductor transceiver solutions. The focus of this review is on companies dedicated to the automotive industry and, in particular, on the 77 GHz car radar frequency band.

NXP

NXP is a Dutch-American semiconductor manufacturer. Until 2006 it was the Philips subdivision of semiconductors. In 2015, NXP acquired Freescale Semiconductors. Currently it has full solutions aimed for ACC, CTA, parking assist, AEB and BSD, including S32R26 and S32R27 microcontrollers for High-Performance radar and TEF810X Fully-Integrated 77 GHz radar Transceiver [22]. A summary of the general characteristics of the TEF810X transceiver are listed below:

- Single chip, FMCW radar for short, medium and long range.
- Car radar frequency band: 76 GHz to 81 GHz.
- Low cost integrated solution: ADC, waveform generator, 3 Tx and 4 Rx units, frequency filters, safety monitoring circuit.
- Phase noise = -86dBc/Hz, transmit power = 12 dBm, noise figure = 12dB.
- Support different MIMO radar operation modes.
- Operating temperature from -40°C to 135°C

- Size: packaged in a 7.5 mm x 7.5 mm area.
- 15 x 15 Ball Grid Array (BGA) for interfacing with antenna board technologies.

Infineon

Infineon is a German semiconductor manufacturer. Until 1999, it was a division of Siemens. In April 2020, Cypress, another semiconductor company, was acquired by Infineon [23]. Two versions of 77 GHz transceivers are under development. The general characteristics of the transceivers are:

- FMCW radars with waveform generation capability, integrated filters and ADC.
- 2 GHz modulation bandwidth.
- RXS816xPL, a 7x8.5 mm packaged 3Tx4Rx transceiver [70]
- RXS8156PLA, a is a 7x7.5 mm packaged 2Tx4Rx transceiver [70]

Texas Instruments

TI is an American technology company focused on semiconductors. It was founded in 1930 [24]. Currently, they have three sensors available for the 77 GHz band with (MIMO) imaging radar capabilities: AWR1642/AWR1843/AWR2243. They also provide cameras, lidar, ultrasound and sensor fusion solutions [25]. A summary of the general characteristics of the transceivers are listed below:

- Single chip, FMCW radar for short, medium and long range.
- Car radar frequency band: 76 GHz to 81 GHz.
- Integrated PLL, ADC, 2/3/3 Tx and 4 Rx units. Built-in calibration and self-test.
- Phase noise = -95 dBc/Hz, transmit power = 12/12/13 dBm, noise figure = 14.5/14.5/12 dB.
- Support MIMO radar operation modes.
- Automotive temperature operating range
- Size: packaged in a 10.4 mm x 10.4 mm area.
- BGA for interfacing with antenna board technologies.

STMicroelectronics

STMicroelectronics is a French-Italian electronics and semiconductor company headquartered in Geneva, Switzerland. It was born as the fusion of SGS Microelettronica and Thomson Semiconducteurs. They have one 77 GHz STRADA770M transceiver, which main characteristics are listed below [26]:

- Single chip, FMCW radar for short, medium and long range.
- Car radar frequency band: 76 GHz to 81 GHz.

- Integrated PLL, ADC, 3 Tx and 4 Rx units.
- Support MIMO radar operation modes.
- Size: packaged in a 9 mm x 9 mm area.
- BGA for interfacing with antenna board technologies.

UMS

UMS is a French-German company focused on RF and millimeter-wave ICs. They are in operations since 1996. Currently, they provide multipliers, mixers and LNAs in the range 76-77 GHz [27].

From all of the above, NXP, TI and STMicroelectronics have transceivers with MIMO capabilities, allowing multiple-chip connection in MIMO mode, making them feasible for imaging systems with virtual-array capabilities. NXP and TI also have application boards with wide azimuth FOV, but as they have 1D array antennas, they can not scan in 2D.

A.2 Imaging radar solutions

In the past years, few companies have also developed full imaging radar solutions, either using proprietary transceivers or acquiring them from semiconductor suppliers. An analysis of the products that are available in the market is conducted here in order to show potential competitors.

Arbe Robotics

The company Arbe Robotics was founded in 2015 in Israel. Phoenix is their chipset solution with imaging capabilities [28] which main characteristics are listed below:

- Frequency range: unknown
- FMCW, proprietary transceiver, 24 Tx and 12 Rx, Time domain MIMO
- FOV: 100° Azimuth, 30° Elevation. Angular resolution: 1° Azimuth, 2° Elevation
- Range: 300 m (7.5-60 cm accuracy)
- Velocity: 0.1 m/s doppler resolution
- Identification of 100 targets
- No false alarms, minimal mutual radar interference, protection from cyber attacks
- Modular and scalable design.

Cognitive Pilot

Cognitive Pilot is a Russian company specialized in software for transport, agriculture and artificial intelligence and hardware for autonomous vehicles. Cognitive Imaging radar is their automotive radar solution [29]. Its main characteristics are listed below:

- Frequency range: 76-81 GHz
- Type of radar: unknown. Number of channels: unknown.
- FOV: 90° Azimuth, 15° Elevation. Angular resolution: unknown
- Range: 280 m (10 cm accuracy)
- Velocity: 0.03 m/s doppler resolution
- 97.7% detection accuracy

Vayyar

Vayyar is an Israeli company and since 2011 they are dedicated to design low-cost imaging solutions. For the automotive industry they have one solution aimed for inside and outside the car [30]. Some characteristics of this 4D sensor are listed below:

- Frequency range: 76-81 GHz
- FMCW, MIMO radar. 72 Tx and 72 Rx.
- Wide FOV in both axis. Angular resolution: unknown.
- Range: unknown.
- Velocity: unknown doppler resolution
- High accuracy and low false alarms

Smartmicro

Smartmicro is a German company founded in 1997, as a spin-off from the Technical University of Braunschweig. They focus on radar design solutions for traffic, automotive and airborne uses [31]. CATegory8 is their concept for imaging radar solution. Two options are available:

UMRR-96 Type 153

- Frequency range: 77-81 GHz
- FOV: 130° Azimuth, 15° Elevation. Angular resolution: 1° Azimuth, 2° Elevation
- Range: 0.15-120 m (1% accuracy)
- Velocity: -400-140 km/h, 0.15 m/s accuracy
- Transmit power (max) 31 dBm

- Weigh: 153 g / Dimensions: 97x76x17.7 mm

UMRR-11 Type 132

- Frequency range: 76-77 GHz
- FOV: 100° Azimuth, 15° Elevation. Angular resolution: 0.5° Azimuth, 0.5° Elevation
- Range: 0.5-175 m (1% accuracy)
- Velocity: -400-200 km/h, 0.1 m/s accuracy
- Transmit power (max) 31 dBm
- Weigh: 274 g / Dimensions: 94.7x84.4x26.4 mm

Appendix B

Additional measurement results launcher in package

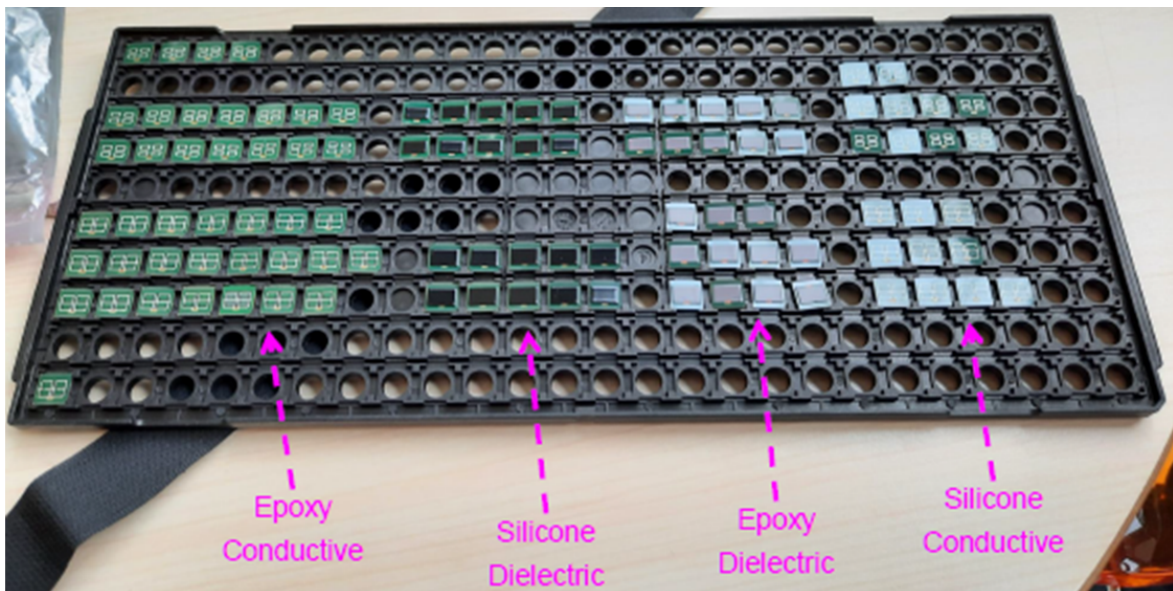


Figure B.1: Different launcher samples.

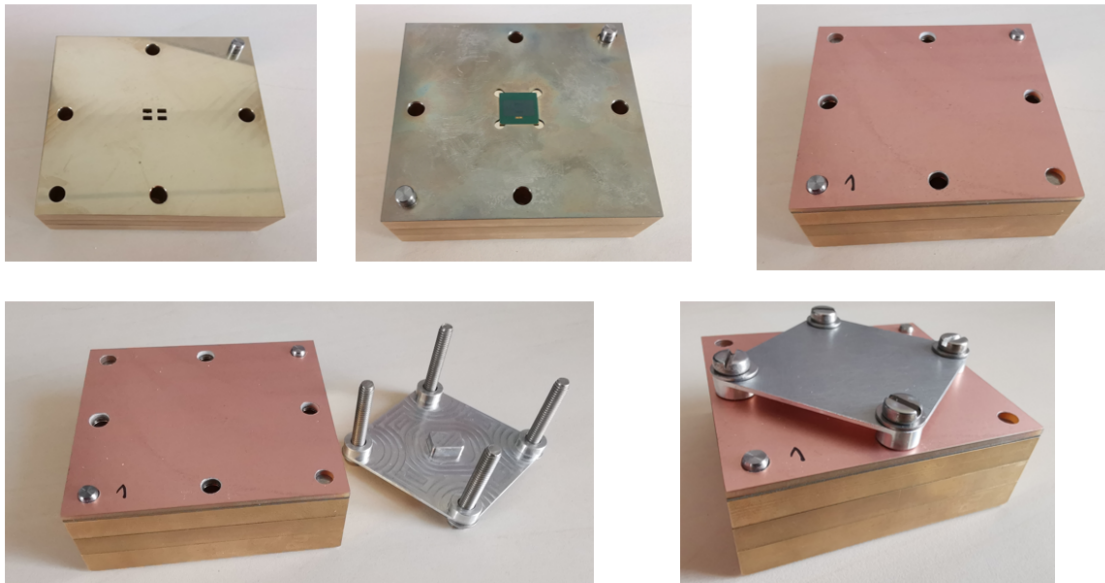


Figure B.2: Launcher assembly in waveguide fan-out.

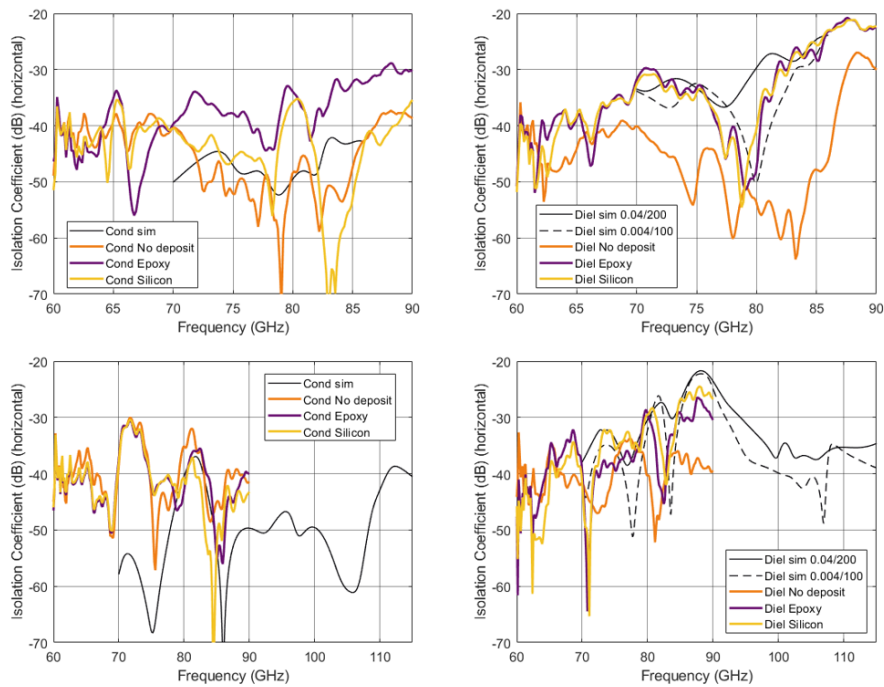


Figure B.3: Isolation between lateral channels. Upper plots are for 77 GHz model and lower plots are for 100 GHz model

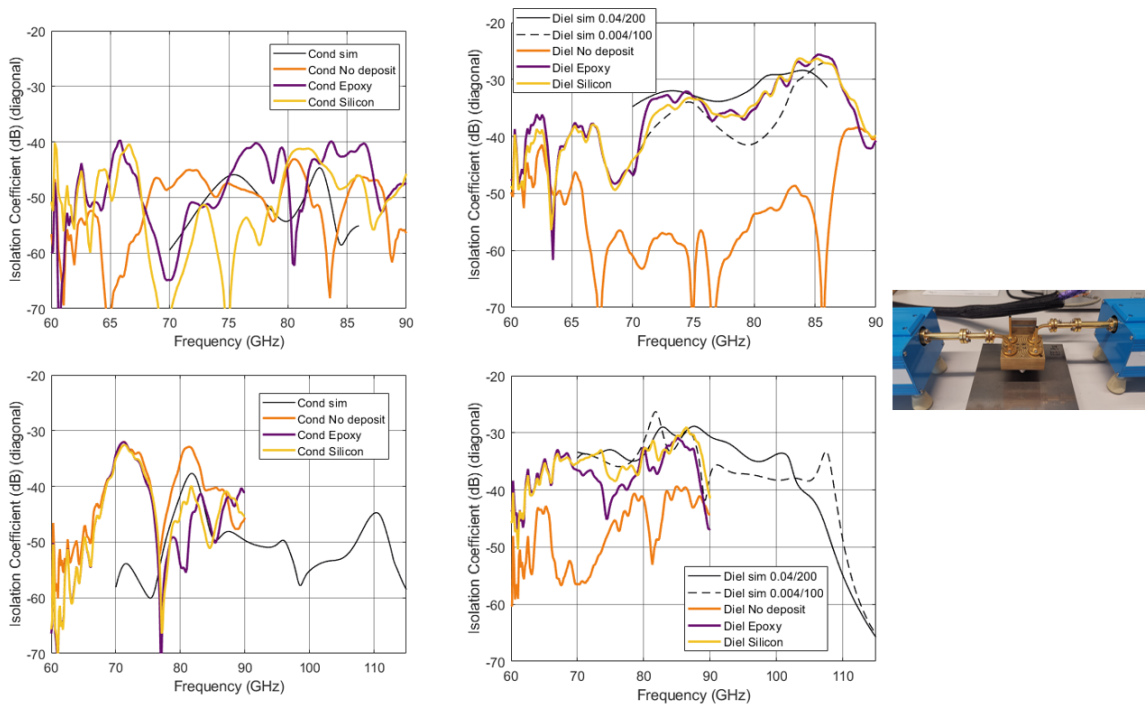


Figure B.4: Isolation between diagonal channels. Upper plots are for 77 GHz model and lower plots are for 100 GHz model

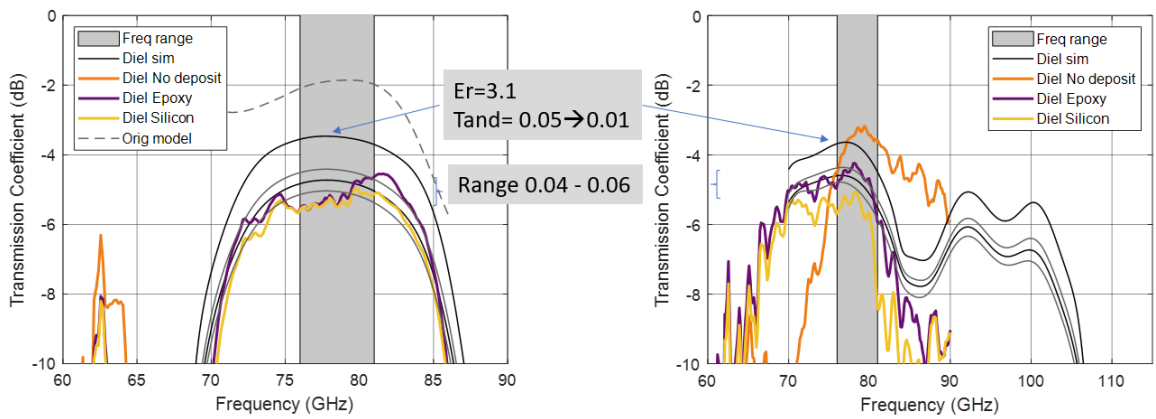


Figure B.5: Simulation for different material interfaces.

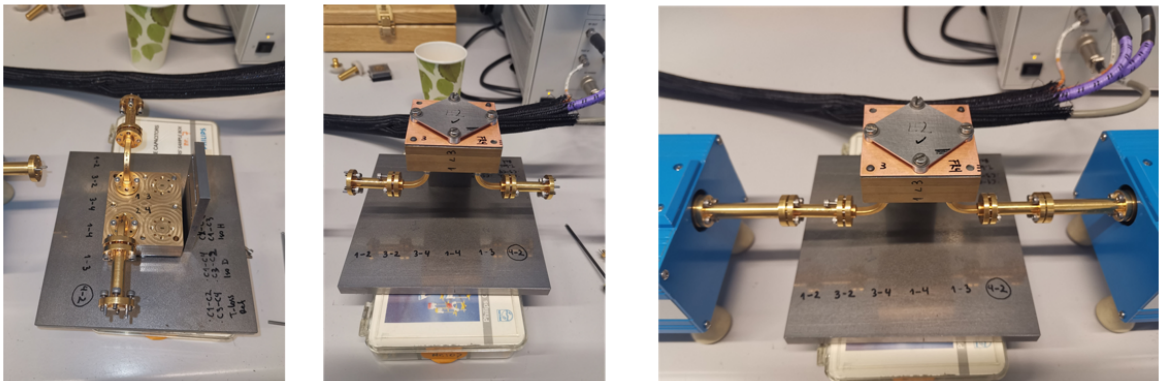


Figure B.6: Testing set-up for pressure measurements.

Date	Measurement	Main result
Apr 6	VNA Launcher 77c without deposit	Higher losses than expected One waveguide show ~7dB and the other ~11 dB EPC FR4 and NXP material behave similar. FR4 is better. Assembly at EPC and assembly at NXP give comparable results
Apr 9	VNA Launcher 77c without deposit	Improved calibration and use of loads improved isolation results First layer in lossy waveguide had higher roughness inside WG Different laminate units show similar results Same laminate show repeatability after disassembly
Apr 19	VNA Launcher 77c (deformable), 77d silicone, 77d epoxy Launcher 100c (deformable), 100d silicone, 100d epoxy	Epoxy dielectric gets fully deformed. It leaves a deposit in WG Silicone dielectric is elastic Deformed conductive (miss measurements conductive elastic) 77c no deposit has less losses, but it is narrowband. 77d silicone has more losses but wideband 100c no deposit and 100c conductive have similar performance Simulation with tand=0.04 fits measurements Differences of pressure applied change results up to 0.5 dB 100 GHz model match better simulations (mostly c model)
May 4	VNA Launcher 77c, 77d, 100c, 100d (no deposit, silicone, epoxy)	Are epoxy and silicone labels swapped? → no Dielectric models with no interface have poor performance 100: conductive no interface and conductive silicone behave similar (best results) 77: conductive no interface is best but narrowband, dielectric silicone and epoxy are wideband, but higher losses Epoxy conductive, tight is better Silicone dielectric, medium pressure for 77, max pressure for 100
May 11, 25	Thickness samples Pressure qualitative analysis Repeatability of launcher measurements	Thickness: conductive silicone 20 um / conductive epoxy 60 → 45 um (before/after measurement) / dielectric silicone 150 um 77c&100c max pressure larger spread / 77c&100c silicone max pressure, small spread / 77c&100c epoxy max pressure medium spread 77d epoxy medium pressure larger spread & 100d epoxy maximum pressure, larger spread / 77d silicone medium pressure, small spread & 100d silicone maximum pressure, larger spread Repeatability: dielectric silicone > conductive epoxy > conductive silicone Sensitivity to pressure: dielectric silicone < conductive silicone < conductive epoxy < dielectric epoxy < no interface
May 20, 21, 31	Launcher compression vs performance Dielectric silicone Conductive undeformed Conductive deformed Conductive no deposit	Dielectric silicone model is less affected: 7um compression → 0.15 dB Conductive epoxy model is less affected: 5um compression → 0.1 dB Conductive silicone model has not a consistent behavior Conductive no-deposit model is more affected: 4um compression → 0.4 dB Compressibility: silicone dielectric > silicone conductive > epoxy conductive > conductive no interface

Figure B.7: Summary of conducted measurements.

	Silicone dielectric	Epoxy dielectric	Silicone conductive	Epoxy conductive
Performance (ins. loss) 77/100 @76-81 GHz *	5.2 – 5.5 dB / 5.1 – 4.8 dB	4.6 – 5.5 dB / 4.2 – 6.0 dB	5.6 – 10.5 dB / 3.0 – 4.5 dB	5.3 – 8.1 dB / 3.6 – 4.5 dB
Bandwidth (-3dB from max)	13.9 GHz / 14.6 GHz	14.2 GHz / 15.9 GHz	5.3 GHz / >20 GHz	5.9 GHz / >20 GHz
Relative bandwidth (fc=78.5 GHz)	0.18 / 0.19	0.18 / 0.20	0.07 / 0.25	0.08 / 0.25
Deformation	Not deformed	Deformed, residuals in WG	Deformed	Not deformed
Compressibility**	1	-	2	3
Repeatability of measurements**	1	-	3	2
Sensitivity to pressure**	1	4	2	3
Optimum pressure	Medium	Medium	Maximum	Maximum
FINAL RANKING	1	4	2	3

* Waveguide fanout and waveguide bends are deducted in these values

** Ranking from 1-4 where 1 is the best

Figure B.8: Summary results of different samples.

Appendix C

Additional simulation results slotted-waveguide antenna

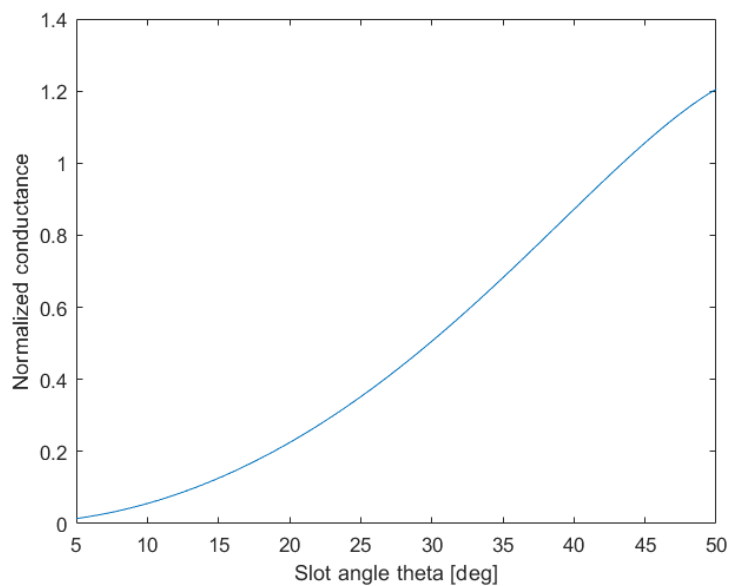


Figure C.1: Normalized conductance with respect to angle of the slot θ based on [42].
 $f=76.5$ GHz, $W=0.2$ mm

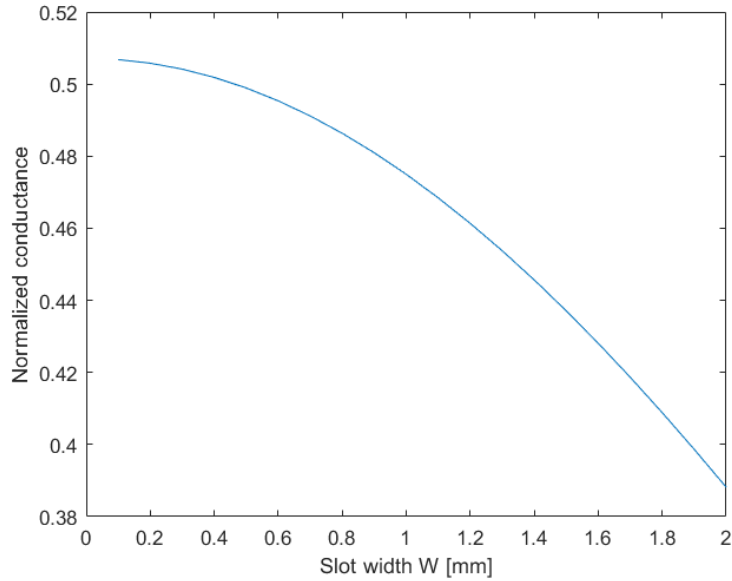


Figure C.2: Normalized conductance with respect to width of the slot based on [42]. $f=76.5$ GHz, $\theta=30^\circ$

C.1 Side feed design

The side feed is the simplest way to feed the antenna, adding only one bend to go from vertical to horizontal, as it was shown in Figure 4.5. The resulting beam pattern for this design is shown in Figure C.3 for 76.5 GHz and in Figure C.4 for the co-polarization component and in Figure C.5 for the cross-polarization component in different frequencies.

At 76.5 GHz, the design frequency, the Ludwig-3 directivity is 14.2 dBi for the longitudinal polarization and -1.39 dBi for the transverse polarization, meaning the cross-polarization level is < -15.59 dB. The SLL is -20.7 dB at the same frequency point. Across the frequencies from 75 to 80 GHz the decay of the gain and SLL is more than 10%. Even though it does cover the frequency range for BSD, it does not cover the entire frequency range of the transceiver module, from 76-81 GHz.

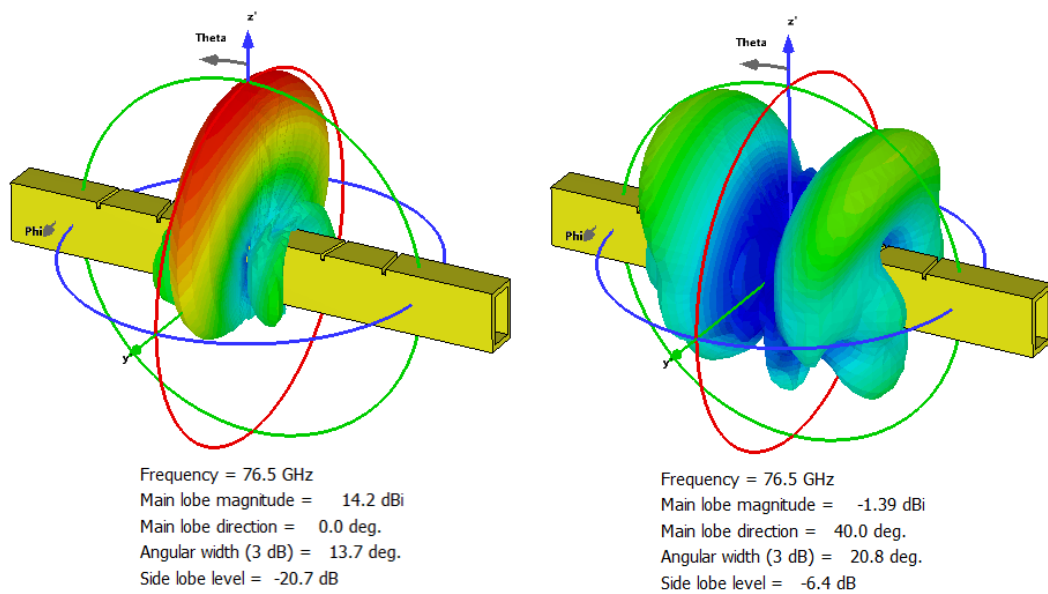
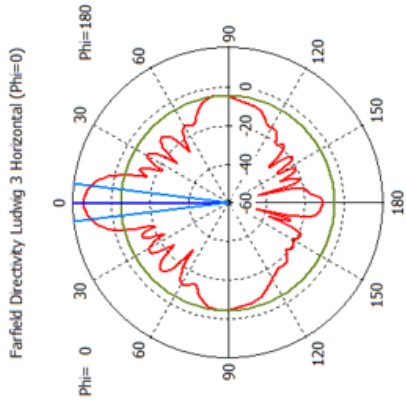
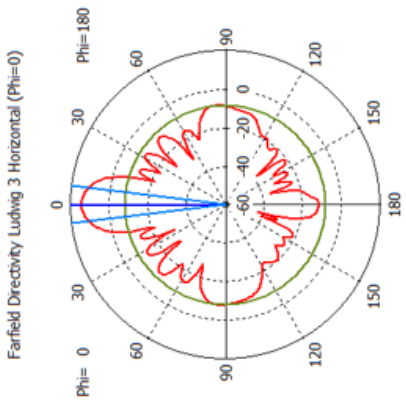


Figure C.3: Side feed model. Ludwig 3 copolar (longitudinal) and cross-polar (transverse) directivity component for 76.5 GHz. Cross-polar level is -15.59 dB $\theta = 5.8^\circ, 8.6^\circ, 12.3^\circ, 12.3^\circ, 8.6^\circ, 5.8^\circ$



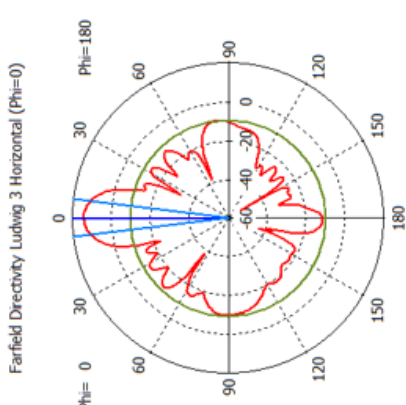
Theta / Degree vs. dBi

Frequency = 75 GHz
 Main lobe magnitude = 14.1 dBi
 Main lobe direction = 0.0 deg.
 Angular width (3 dB) = 14.2 deg.
 Side lobe level = -23.6 dB



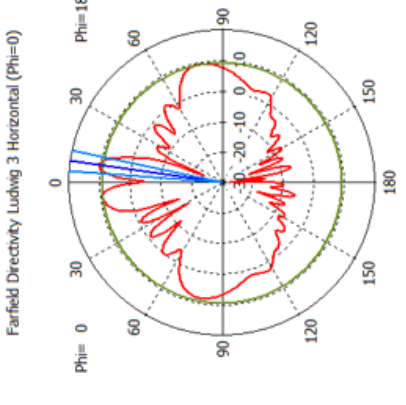
Theta / Degree vs. dBi

Frequency = 76 GHz
 Main lobe magnitude = 14.2 dBi
 Main lobe direction = 0.0 deg.
 Angular width (3 dB) = 13.7 deg.
 Side lobe level = -22.4 dB



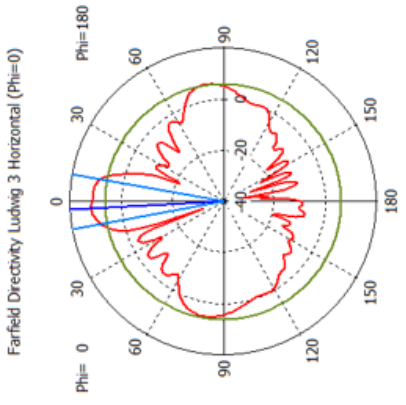
Theta / Degree vs. dBi

Frequency = 77 GHz
 Main lobe magnitude = 14.2 dBi
 Main lobe direction = 0.0 deg.
 Angular width (3 dB) = 13.7 deg.
 Side lobe level = -18.8 dB



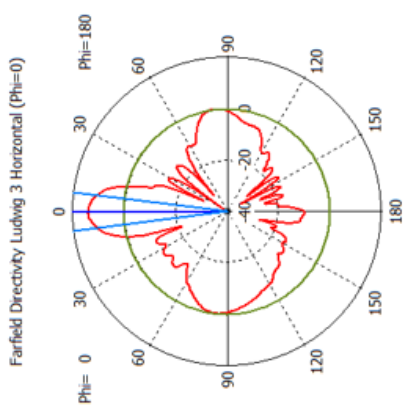
Theta / Degree vs. dBi

Frequency = 78 GHz
 Main lobe magnitude = 13.8 dBi
 Main lobe direction = 0.0 deg.
 Angular width (3 dB) = 14.5 deg.
 Side lobe level = -13.8 dB



Theta / Degree vs. dBi

Frequency = 79 GHz
 Main lobe magnitude = 11.6 dBi
 Main lobe direction = 3.0 deg.
 Angular width (3 dB) = 20.8 deg.
 Side lobe level = -5.4 dB



Theta / Degree vs. dBi

Frequency = 80 GHz
 Main lobe magnitude = 10.4 dBi
 Main lobe direction = 8.0 deg.
 Angular width (3 dB) = 7.7 deg.
 Side lobe level = -1.0 dB

Figure C.4: Side feed model. Ludwig 3 copolar (longitudinal) for different frequencies. $\theta = 5.8^\circ, 8.6^\circ, 12.3^\circ, 12.3^\circ, 8.6^\circ, 5.8^\circ$

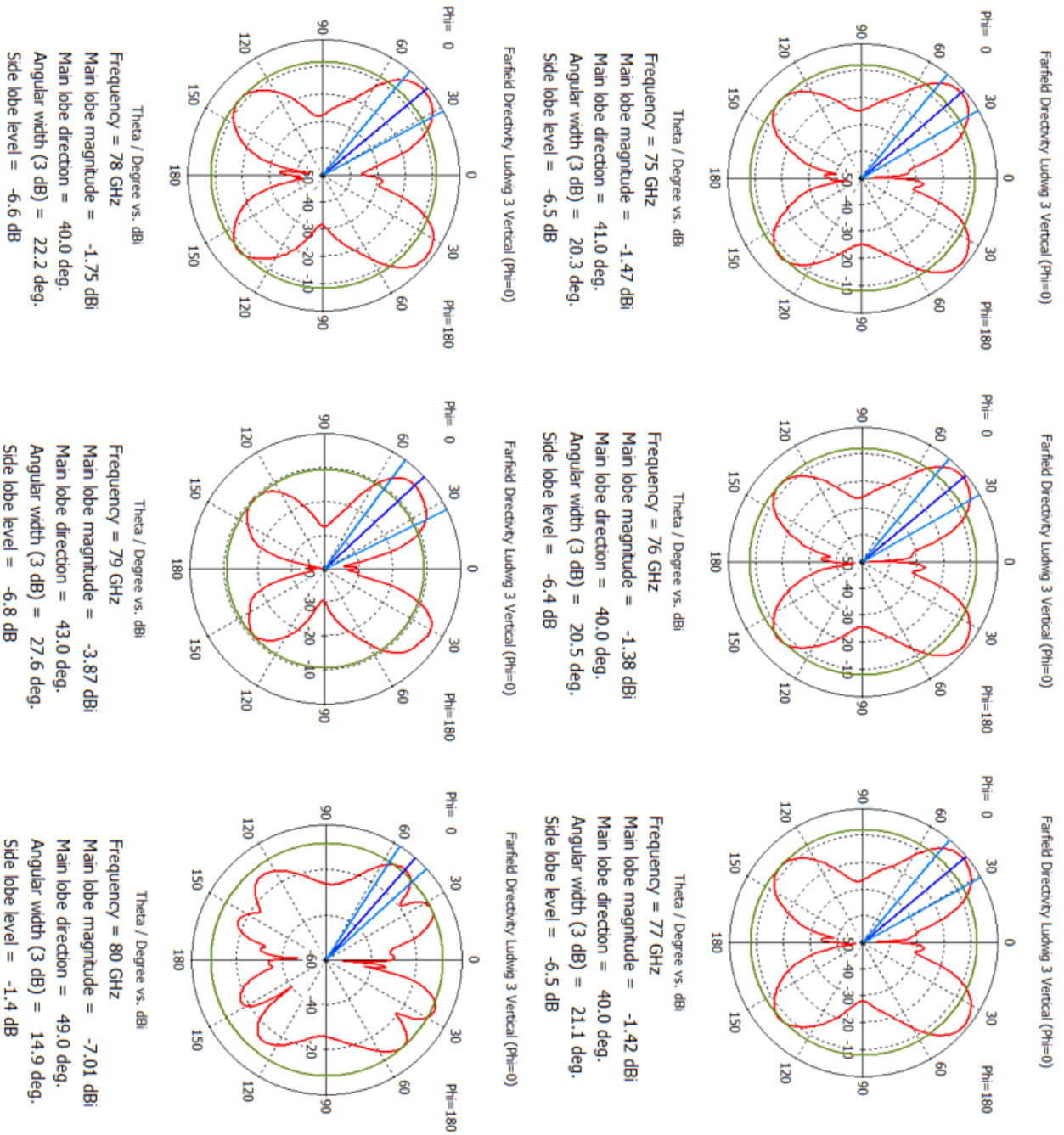


Figure C.5: Side feed model. Ludwig 3 cross-polar (transverse) for different frequencies. $\theta = 5.8^\circ, 8.6^\circ, 12.3^\circ, 12.3^\circ, 8.6^\circ, 5.8^\circ$

C.2 Loaded waveguide

By adding loads to the waveguide ends, either in case of the side feed or in case of the middle feed, the wave inside the waveguide becomes a travelling wave. There is less energy stored in the cavity and thus the impedance matching is more straightforward because the resonant behavior is mitigated and then, the input impedance is continuous over a larger frequency range [53]. Without any additional matching structure, the model presented for the middle feed already has a reflection loss better than 15 dB for the range 76-77 GHz, as shown in Figure C.6. Nevertheless, creating a load for a waveguide in this frequency range is not simple and then it will also imply higher costs. More importantly, though, is the fact that a load will imply absorption of power that will not be reflected but that power is also not radiated. Ultimately the device will not be power efficient then.

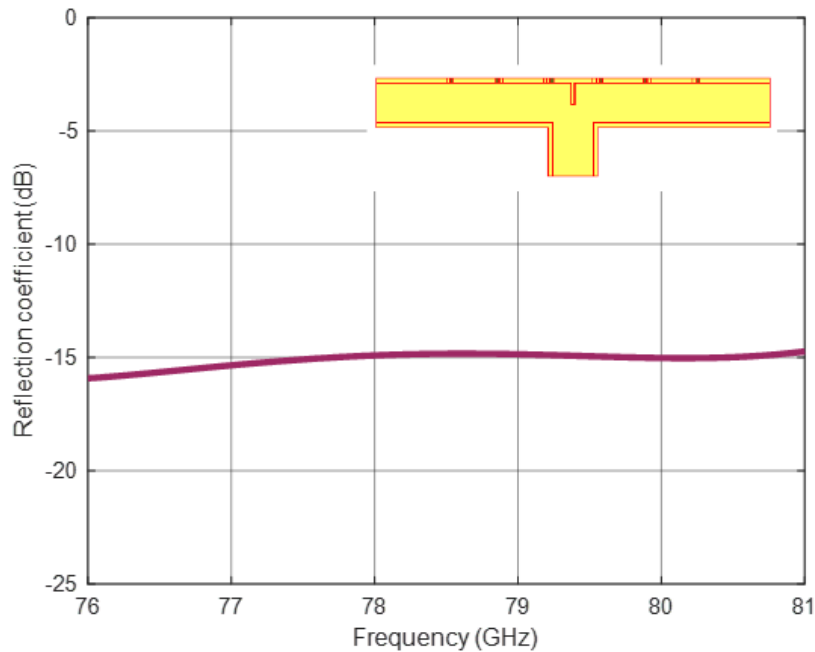


Figure C.6: Reflection coefficient in a loaded middle-fed slotted waveguide antenna. Because the loads in the waveguide ends produce a travelling wave, the reflection towards the waveguide feed is not high.

C.3 Central feed design

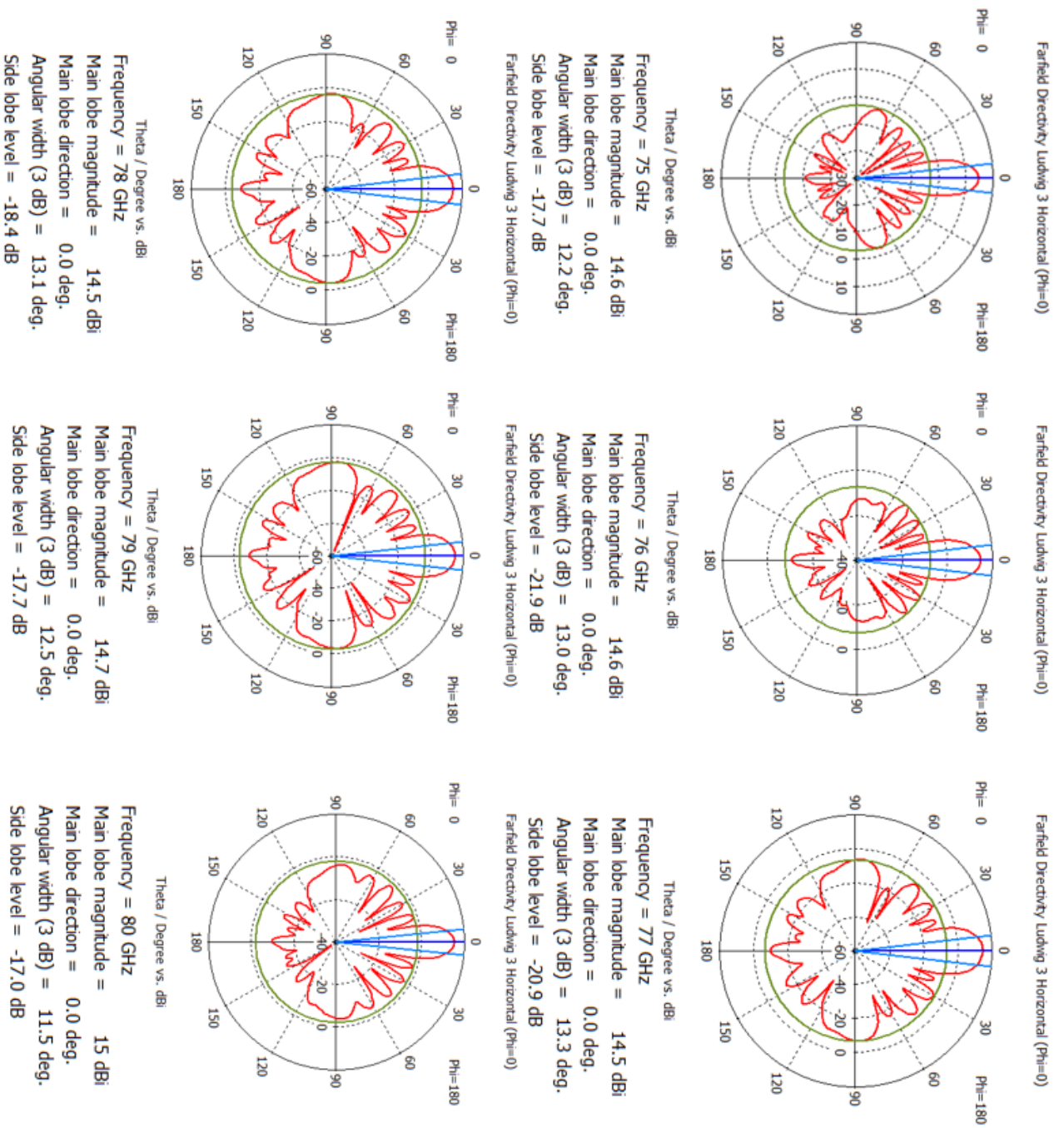


Figure C.7: Middle feed model. Ludwig 3 copolar (longitudinal) for various frequencies. $\theta = 5.8^\circ, 8.6^\circ, 12.3^\circ, 12.3^\circ, 8.6^\circ, 5.8^\circ$

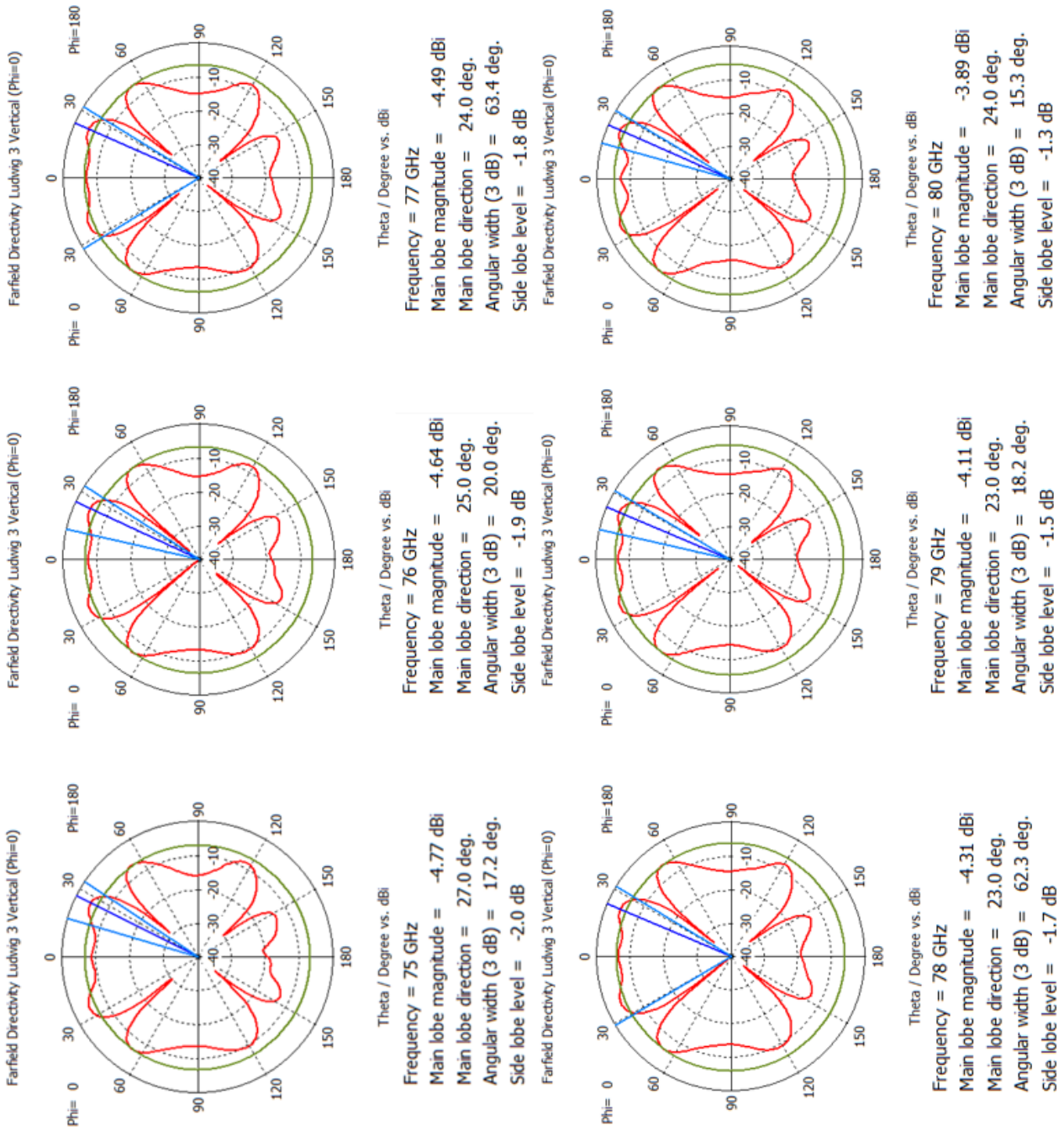


Figure C.8: Middle feed model. Ludwig 3 copolar (transverse) for various frequencies. $\theta = 5.8^\circ, 8.6^\circ, 12.3^\circ, 12.3^\circ, 8.6^\circ, 5.8^\circ$

C.4 Model with added metal plane

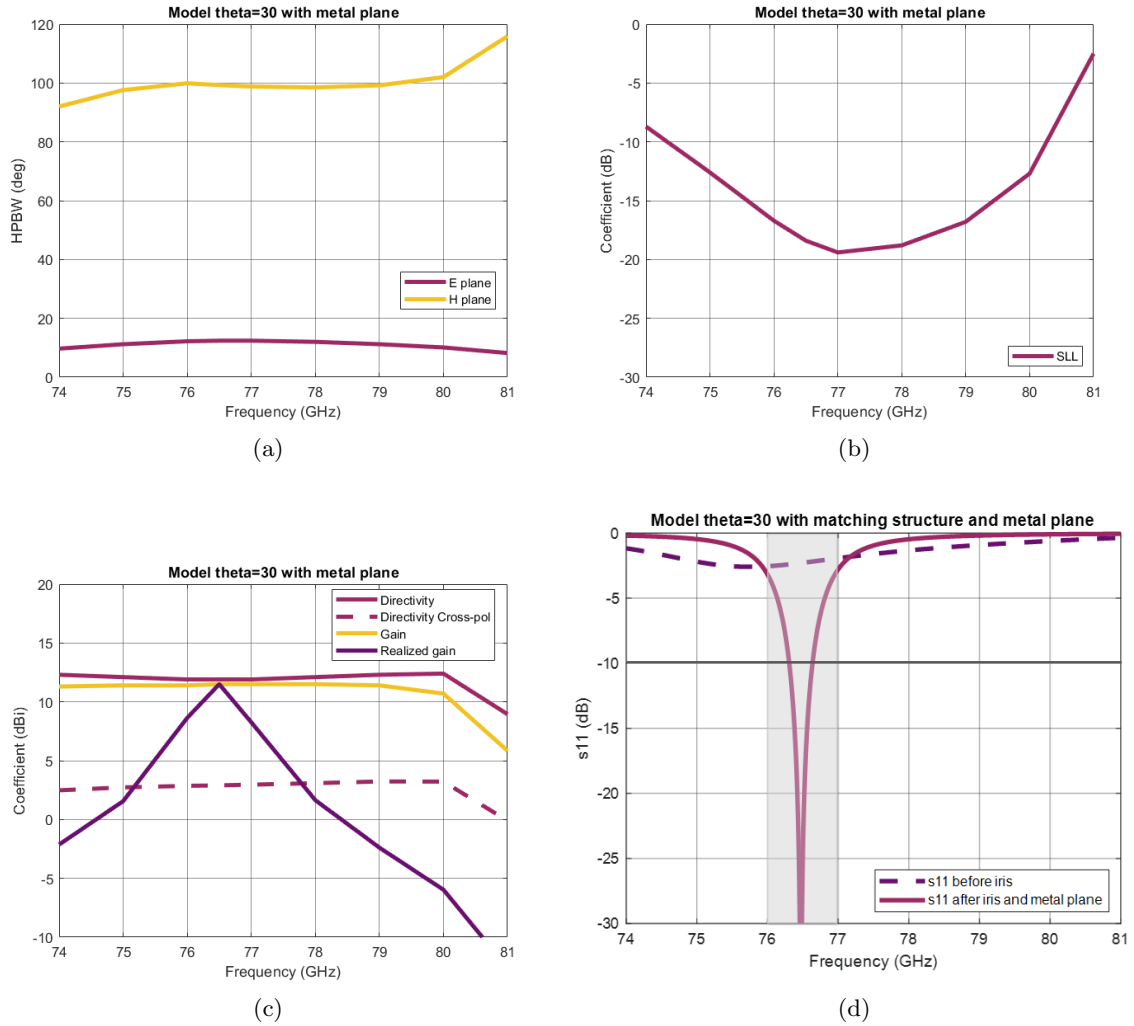


Figure C.9: Middle feed 30° model, with matching structure and metal plane, simulation results over frequency. (a) is half power beam-width, (b) is SLL, (c) is directivity and gain and (d) is reflection coefficient